Final Technical Report

Turbine Aeration Design Software for Mitigating Adverse Environmental Impacts Resulting From Conventional Hydropower Turbines

DE-EE0005416 oo1
October 2011 – March 2015

Principle Investigator: John S. Gulliver, Professor,
612-625-4080, gulli003@umn.edu

Working Partners: Roger E.A. Arndt, Acting PI; Fotis Sotiropoulos, co-PI;
Chris Ellis, Mohammed Hajit, Ashish Karn, Christopher Milliren

University of Minnesota
Minneapolis, Minnesota 55455
Attn: Sponsored Projects Administration

March 2015

This report is based upon work supported by the U. S. Department of Energy under Award No. DE-EE0005416 oo1

.

Any findings, opinions, and conclusions or recommendations expressed in this report are those of the authors and do not necessarily reflect the views of the Department of Energy.

Table of Contents

Executive Summary

This project involved the development of a conventional hydropower turbine aeration test-bed for computational routines and software tools for improving environmental mitigation technologies for conventional hydropower systems. In achieving this goal, we have partnered with Alstom, a global leader in energy technology development and United States power generation, with additional funding from the Initiative for Renewable Energy and the Environment (IREE) and the College of Science and Engineering (CSE) at the UMN.

1). Physical model experiments: Experimental data, designed to be used as an effective verification of the software, was collected in the SAFL high-speed water tunnel. Two hydrofoils, both with NACA 0015 profiles and both specially designed for aeration experiments, were studied. The focus of attention was the bubbly wake generated by precisely metered ventilation air flow. Bubble location and size distribution information was captured with high-speed video using a custom-made pulsed LED light source to back-light the flow. The pulsed LED array is capable of flash rates up to 10 kHz with a minimum 5 microsecond pulse width (flash duration) and rise and fall times ~200 nanoseconds. Equipped with TTL control, the light source was integrated with a LaVision TR-PIV system. This allowed the light source to be used for the acquisition of periodic image pairs (known as frame straddling) used by an in-house developed bubble tracking algorithm to calculate randomly located velocity vector fields and associated statistics or for high speed time series image acquisition needed to produce time resolved velocity fields such as is used in the tracking of coherent structures. To improve the uniformity of back-lighting in the images, a light shaping diffuser was placed between the light source and the test section. This improved the image processing associated with both the bubble size analysis and particle shadow velocimetery (PSV). A 1-megapixel Photron APX-RS camera, capable of 3000 frames per second at full resolution (up to 250,000 fps at limited resolution) was used to obtain images. These data provided an extensive and rich dataset accessible for computational validation studies of the impact of entrained air on the flow field, and the impact of the flow field on air entrainment and mass transfer. During the study we answered three questions that are very important to the success of an aerating turbine: 1) for a given flow field, what will be the quantity of air that is entrained, 2) what will be the bubble size of the entrained air at a given location after entrainment and 3) what will the oxygen transfer be from these bubbles? All three of these processes were the focus of the experiments, which were completed using two different hydrofoil configurations; with air injection from a slot close to the leading edge and another fitted with an air injection slot at the trailing edge. A series of air injection experiments was completed at several hydrodynamic conditions, allowing for quantitative analysis of bubble size and velocity statistics and oxygen transfer capabilities for the two turbine blade hydrofoil designs.

2). CFD model validation: Using the data collected from the physical model experiments, high resolution large eddy simulation (LES) bubble tracking techniques will be validated and implemented using both of the tested NACA-0015 ventilated blade geometries. The computational code, developed at Saint Anthony Falls laboratory, contains the most recent computational libraries and solvers for numerical calculations. Our computational code is implemented in parallel C language accompanied by PETSC and BoomerAMG libraries. Second order discretization techniques are used for both time and space which enables us to carry out

simulations with high accuracy. The code is implemented in parallel, which allows running the jobs on our supercomputing cluster at SAFL. The code utilizes the Eulerian/Eulerian approach from the theory of multicomponent fluids. Aimed at carrying out Euler/Euler two-way coupled large eddy simulation of turbulent dilute bubbly flows, the proper filtering of the governing equations were extracted through single-filtering of the component weighted microscopic Navier-Stokes equations. Through low pass filtering, the frequencies higher than the Nyquist frequencies are removed from the solution. The set of equations to be solved numerically are the mass and momentum balance equations for gas and liquid phases, accompanied by an equation of state and various complementary models for closure of turbulence and interfacial momentum terms. To overcome the stiff and nonlinear character of the equations, certain simplifications were justified and applied, which allowed for efficient solvers and decreased considerably the computational cost. The simplifications were based on the valid assumptions that the liquid phase density is much greater than the gas phase density, and there is low gas holdup in the domain. As a result, the liquid phase equations are cast as an incompressible flow class of Navier-Stokes with some modifications applied in the momentum equation, while the gas phase is seen as a compressible fluid. Throughout the development of the computational code, numerous test cases were considered with the purpose of validating the developed code. This aeration visualization and analysis tool will be an addition to the existing novel computational techniques developed at SAFL. The techniques developed during this portion of the project will be directly applicable to aerating turbine design, to test the assumptions and provide preliminary assessment of these designs, thereby saving energy and resources previously allocated towards extensive full-scale testing campaigns.

The research program described provides a critical tool for advancing the development and implementation of aerating turbines at U.S. hydropower facilities. In addition, the experimental results will comprise an aeration test-bed for all manufacturers, increasing the reach of the U.S. DOE's efforts. The advanced aeration design capabilities resulting from utilizing this software will reduce the cost and regulatory uncertainty prior to hydropower development.

I. Introduction

The discharge by hydropower facilities of water that is low in dissolved oxygen is increasingly of concern due to its effect on downstream water quality. As a result, a number of techniques have been investigated that aerate the water employed, one being direct aeration by the hydroelectric turbine. To assess the efficacy of such strategies, coupled experimental and numerical approaches are needed that connect bubble size and behavior in high speed and turbulent flow to the physical processes governing gas transfer. The purpose of this study is to 1) develop the necessary algorithms to determine the bubble size distribution and flow field in the wake of a ventilated hydrofoil utilizing background illumination, 2) measure gas transfer from the ventilated bubbles and relate the results to known theories of gas transfer from bubbles, and 3) develop a computational code capable of carrying out large eddy simulation for bubbly flows and run it for the ventilated hydrofoil problem. The measurements made as part of the experimental program provide an extensive and rich data set allowing correlation to measurements of gas transfer efficiency and validation of computational studies of two phase flow through ventilated hydroturbines. The developed computational code is used to simulate general dilute two-phase bubbly flows for some benchmark problems, including the aerating hydrofoil.

For a detailed analysis of two-phase flows, non-intrusive optical techniques are most suitable. Such measurement techniques can provide velocity fields and local bubble size distributions. Phase-Doppler anemometry (PDA) has a higher sizing accuracy than direct imaging techniques when small spherical bubbles are studied, but accuracy decreases when the shape of the bubbles becomes non-spherical and their size increases. Laser light sheet illumination is very useful for large-scale measurements. However, a limiting problem for the application of laser sheet illuminated particle image velocimetry (PIV) to bubbly flows is the strong absorption of the penetrating laser light sheet by scattering on the surface of the bubbles, particularly in dense bubble clouds. One technique that allows the quantifying of bubble size, shape, and distribution is shadow imaging using a diffuse back-light. A problem that arises in higher void fraction bubbly flows is that of overlapping bubble images, which may include in-focus and out-of-focus bubbles. A reliable algorithm is necessary to reconstruct missing parts of overlapping bubbles. There is also the issue of image calibration and the determination of appropriate length scales. Unless a telecentric lens is used in the imaging system, the length scale (real world length per pixel) increases with distance from the camera. A rationale needs to be established that assigns appropriate lengths to the acquired images. This affects both the estimation of bubble size and bubble velocity.

The present study developed the necessary algorithms to determine the bubble size distribution and velocity field in the wake of a ventilated hydrofoil using background illumination. Velocity fields were derived using particle-tracking and PIV techniques applied to the shadow images The in-focus bubbles, those in the camera's depth of field, cast the darkest, most distinct shadows. Image depth-of-field is determined by the camera setup and can be used to determine the location and thickness of the measurement plane. This is important in establishing the needed length scales in the images. Using shadow images, the size, number, distribution, and velocity of bubbles in the wake of a ventilate hydrofoil were determined.

Using the results of the bubble size analysis, mass transfer measurements can be related to the bubble characteristics. The measured distributions of bubble surface area along with disturbed chemical equilibrium measurements were used to characterize the liquid film coefficient of the bubbles, a crucial parameter in mass transfer, and relate it to parameters of the flow field.

The numerical development of advanced, efficient computational routines and software tools that can simulate conventional hydropower turbine aeration problems for advanced hydropower development has been undertaken. The computational code has been implemented in parallel platform, which allows for efficient supercomputing of the bubbly flows. For this purpose, large eddy simulation (LES) of high-resolution, fully turbulent bubbly two-phase flow has been developed, based on a purely Eulerian (two-fluid approach) framework. The velocity field, pressure field, void fraction and density field for both phases is the output. The code can be used for general dilute bubbly flows but is also optimized for flow around hydrofoils. The results gained by the computational code will help in our understanding of the underlying physics of the bubbly flows. Moreover, the code can be used for simulating, predicting and efficient design of aerating hydrofoils for industrial purposes.

II. Background

Conventional hydropower has the potential to contribute a substantially larger percentage of our Nation's energy requirements than the present state. However, many environmental risks resulting from these facilities have been identified. Decreased water quality ranks among the most notable risks, in the form of greatly reduced dissolved oxygen quantities in the discharged water to the downstream environment. The nearly anoxic environment created in the tailwater discharge of hydropower facilities poses great environmental risks to aquatic flora and fauna.

The impoundments necessarily for creating the hydraulic head to operate conventional hydroturbines, produce appreciable energy and justify the economic expense of these projects initiate the deterioration of the water quality. The residence time of water within reservoirs is long; therefore, processes such as fish and plant respiration and other biological oxygen demands decrease the dissolved oxygen quantities, especially at greater depths within the reservoir. Only surface waters are occasionally replenished with oxygen through minimal transfer processes resulting from wind and wave action. Water discharged downstream of the dam needs to have adequate levels of dissolved oxygen to support the aquatic communities (ORNL 2010).

Aerating turbines are currently developed without accurate experiments on the size of bubbles that are generated by the entrainment and bubble breakup processes. Most specifically, the size of bubbles generated is guesswork that is not well represented. SAFL has developed a new shadowgraph technique that can examine the bubble sizes in a highly aerated shear flow, such as occur in a hydroturbine. This technique is used to quantify bubble size and air entrainment for a variety of flow velocities and flow shear rates on a minimum of two blade designs: one with well-studied hydrodynamics and one that is related to Alstom's aerating turbine technology. In addition, gas transfer measurements designed to quantify oxygen transfer will be undertaken. The adsorption-desorption, disturbed equilibrium technique that is well established at our laboratory will be utilized.

The experiments on the first blade design will be immediately made available to the general community as a test-bed for any aerating turbine software. SAFL has experience with this process of developing test-bed measurements, through the U.S. Office of Naval Research (ONR), where a similar experimental program was developed to supply data from a cavitating hydrofoil as a test-bed for three selected CFD programs. Our experience with the ONR in a similar program justifies our certainty that we can successfully supply this data to the hydroturbine industry. With well-verified software, the turbine industry will be able to investigate different aerating turbine designs successfully with CFD programs, avoiding multiple, cumbersome and expensive model turbine tests. Optimization of turbine configurations and operating conditions can occur prior to physical model testing and installation, therefore drastically reducing the installation and maintenance costs associated with conventional hydropower. Additionally, if the turbine manufacturer's and hydropower facilities are able to demonstrate improved aeration and adequate dissolved oxygen levels within the discharged water, permitting and environmental setbacks will be minimized and can accelerate the process leading to facility operation. These considerations all provide a lowered cost of operation and energy.

III. Experiments

1. Experimental Set Up

The experiments were conducted in the high-speed water tunnel at Saint Anthony Falls Laboratory (SAFL) of the University of Minnesota. The tunnel is capable of velocities in excess of 20 m/s. The test section measures 0.19m (W) x 0.19m (H) x 1.2m (L), and is fitted with observation windows on three sides. A special design of the tunnel allows for the removal of large quantities of air during experiments, allowing for long time-period experiments with little to no effect on test section conditions. Figure 1 provides a schematic of the SAFL water tunnel. Two NACA0015 hydrofoils, specially designed to incorporate air ventilation, were installed in the test section employing a cylindrical mounting plug that allowed adjustable angles of attack (α). The hydrofoils are 190 mm in span and 81 mm in chord. Air was injected into a slot spanning the hydrofoil by means of a compressed air line. In one of the hydrofoils (from here on referred to as the SAFL foil), this air injection slot had a width of 0.5 mm and was located 5 mm from the leading edge. In the second hydrofoil (from here on referred to as the Alstom foil), this slot had a width of 0.33mm and was located in the trailing edge. A special design of internal ducting insured an even air distribution across the span of the hydrofoil.

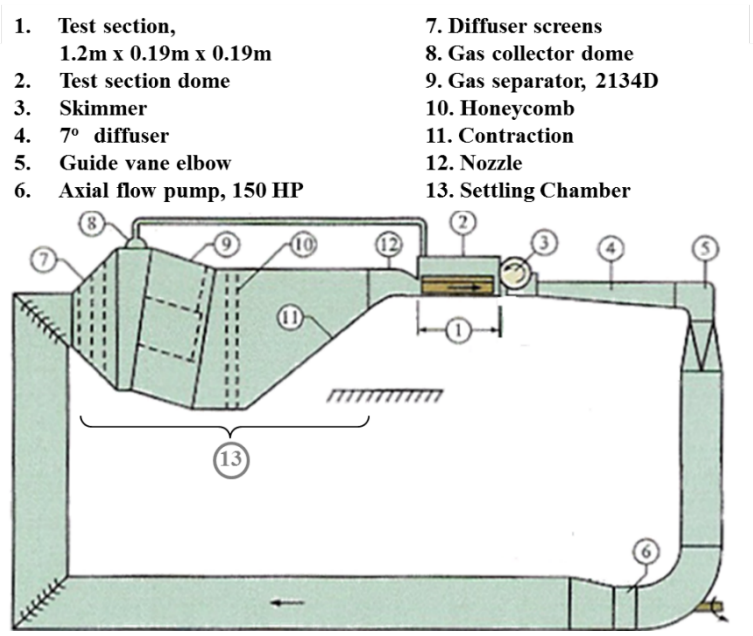

Figure 1. SAFL water tunnel

Validyne AP-10 absolute pressure transducer was used to measure absolute pressure in the test section. A Validyne DP-10 differential pressure transducer was employed to measure the differential pressure between the settling chamber and test section, which in turn was used to calculate test section velocity. The pressure transducers were calibrated before each series of experiments using a mercury filled manometer. The pressure transducer calibrations produced linear best fits with R-squared values typically 0.9999 or higher for both the transducers. Errors inferred from a least squares fit line were approximately 0.1 kPa for both pressure transducers.

These errors produced a maximum error in the measured velocity of 0.11 m/s, with typical errors being closer to 0.02 m/s.

2. Dissolved Oxygen Instrumentation and Measurement Procedure

A YSI thermistor probe was used to monitor temperature in the water tunnel. The probe is mounted in a plug on the settling chamber where it is submerged in the circulating flow of the water tunnel. An Omega Engineering FMA-2609A mass flow controller was used to set and measure airflow to the hydrofoil. Two Hach luminescent dissolved oxygen (LDO) probes and controller were used to measure DO concentration in both the settling chamber and the elbow vane downstream of the diffuser.

A disturbed equilibrium technique was used to estimate gas transfer rates by initially degassing the water to the lowest level possible and then reoxygenating the water, while taking continuous DO concentration measurements (Giovannettone and Gulliver 2008). During deoxygenation a portion of water was withdrawn from the tunnel and circulated through a degassing chamber under vacuum where the water was discharged into the chamber through nozzles, creating a cloud of falling droplets. The degassing loop was run overnight, reducing the DO concentration to approximately 4 ppm. Immediately prior to an aeration test, the water tunnel was run without air injection until the water was thoroughly mixed. A test commenced by setting the test section velocity and airflow rate. The experiment was run for approximately 10 hours or until the oxygen concentration exceeded 99% of saturation.

3. Air Injection Configurations

3.1 Near leading edge

During the experiments using the SAFL foil, the hydrofoil was installed in the test section. As shown in Figure 2, a narrow spanwise slot allowed air to be injected into the flow near the leading edge of the hydrofoil on its suction side.

For the gas transfer measurements, the full span length of the injection slot was used for air injection. This results in a dense spanwise bubbly wake. However, in order to make bubble measurements, ventilation was limited to a narrow 9.6 mm long slot section (5% of the full slot length) at the center of the span. This configuration ensured that bubbles remained within a narrow depth of field from the center of the test section. Videos of the bubbly wake verified that the lateral drift or spread of the bubbles was minimal. Silberman (1958) investigated the production of bubbles by an orifice in liquid shear flows. His findings indicated that the bubble diameter depends only on air injection rate and water velocity, not on orifice characteristics (e.g. size) as long as the gas issues as a jet from the orifice. Similarly, it is believed that the bubble sizes coming out of the injection slot are not dependent on the slot width. Since the injection slot width is constant in our experiments, it is reasonable to posit that the bubbles produced from the limited (5%) slot length are representative of the bubble population that exists when the full span is ventilated. For these bubble size analysis experiments, air flow rates were selected that were 5% of those used in the gas transfer testing. Thus, for any air flow test condition, the air flow rate per unit slot length was kept constant. Fifteen different experiments were conducted at test section water speeds of 5, 7.5 and 10 m/s, ventilation gas flow of 10, 20 and 30 LPM per unit

span and hydrofoil angle of attack (AoA) of 0, 4 and 8 degrees. The bubbly wake images were obtained at 3 streamwise distances of 109, 243, and 377 mm downstream of the hydrofoil center (or 1.3, 3.0 and 4.7 times the chord length, respectively).

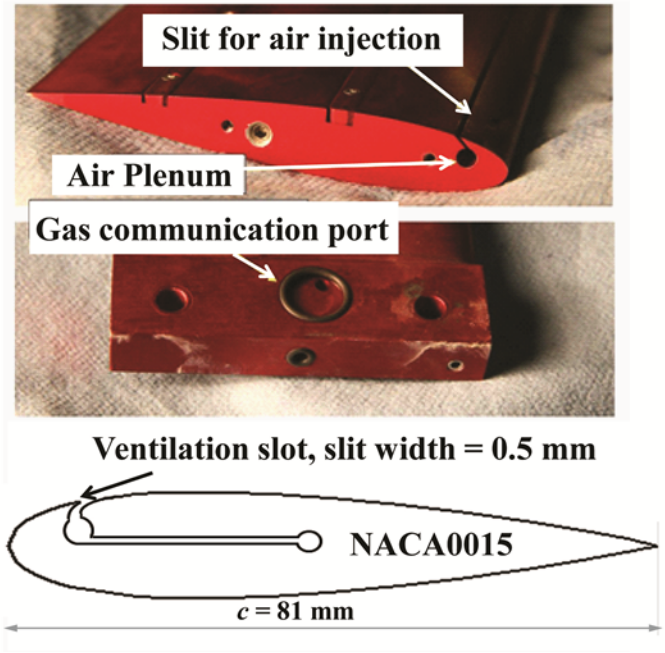

Figure 2. Details of the NACA0015 ventilated foil (adapted in part from Karn et al, 2015b).

3.2. At trailing edge

The Alstom foil, also a 2-D NACA 0015 foil having the same dimensions as the SAFL foil but incorporating an aeration slot centered in the trailing edge, was designed and fabricated. This foil used the same mounting plug and air source that had been used previously by the SAFL foil. When assembled, the foil was air tight along all joins and contained a 1 mm wide slot that ran from the tunnel wall on the mounted side to 5 mm from the non-mounted foil end. With the use of shims of various thicknesses, a number of slot widths 1mm or less could be tested. Renderings of the Alstom foil are shown in Figs. 3-6.

Since the aeration slot location and associated plenum of the Alstom foil were different than that of the SAFL foil, it was decided to rapid prototype (3-D print) an approximate version of the foil to do preliminary testing in static water. (See Fig. 7.) The primary intent of this testing was to assess the ability of the foil design to uniformly discharge air along the length of the slot. The prototyped foil was submerged in static water, leveled, and ventilated using the design air flow rates that had been used in the SAFL test program. At all flows, the foil discharged the ventilation air uniformly along its length. As a result, the final foil was CNC machined in aluminum and anodized.

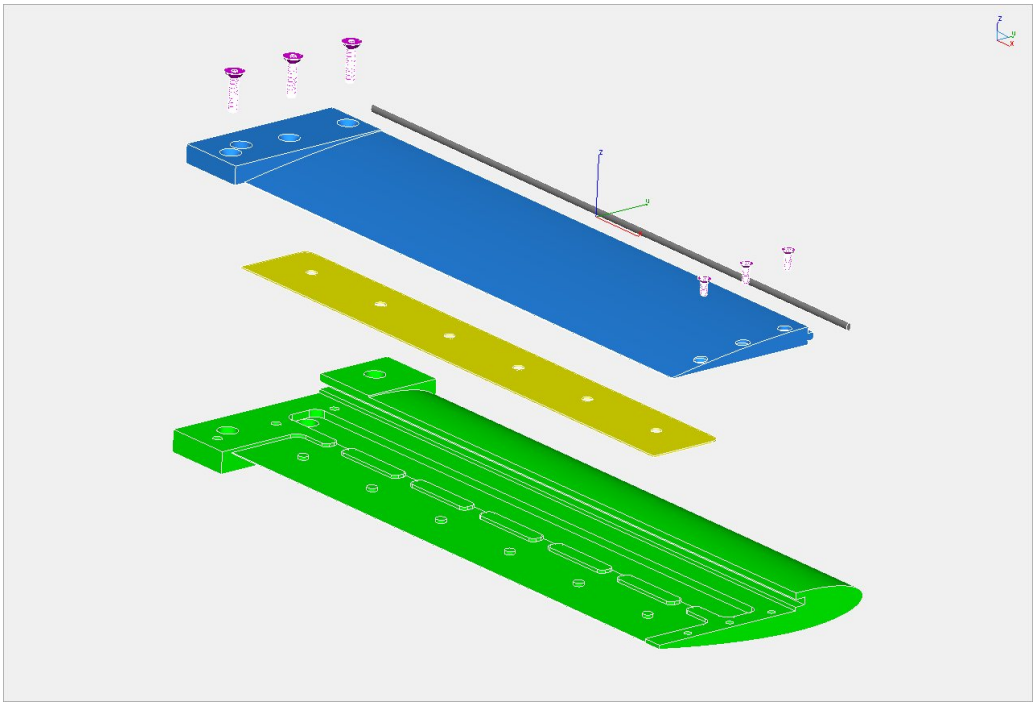

Figure 3. Expanded view of computer rendered Alstom foil

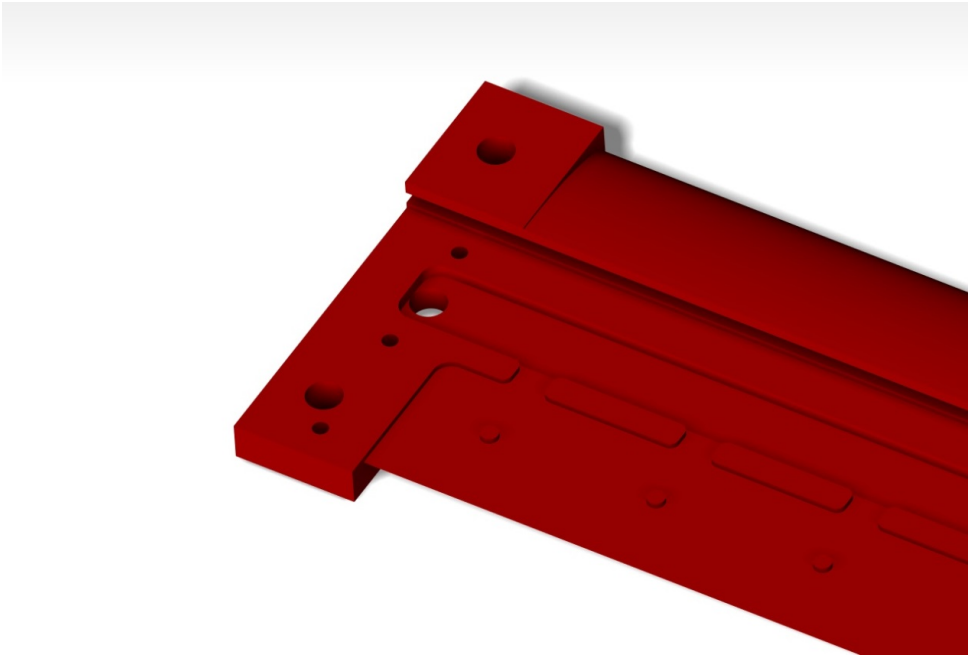

Figure 4. Alstom foil rendering, interior mounting base close-up

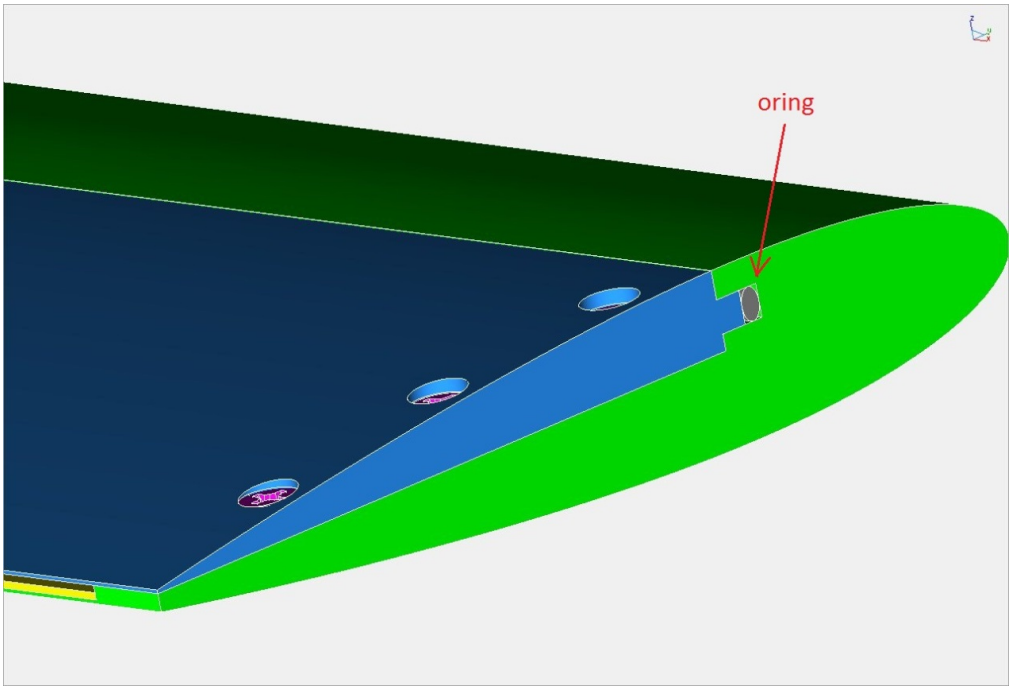

Figure 5. Alstom foil rendering, non-mounted end close-up

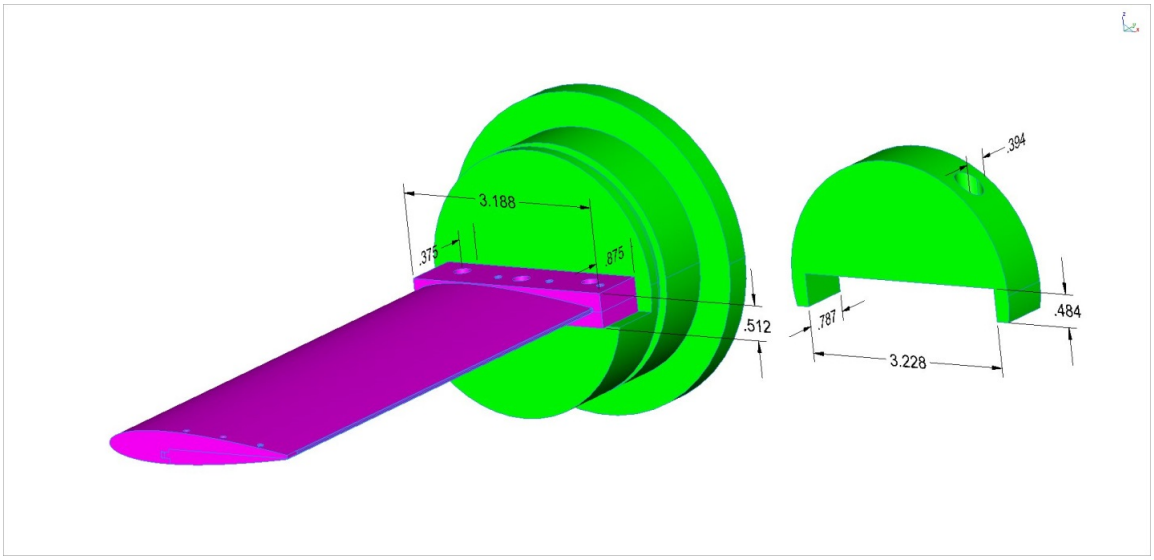

Figure 6. Alstom foil rendering, foil with mounting plug

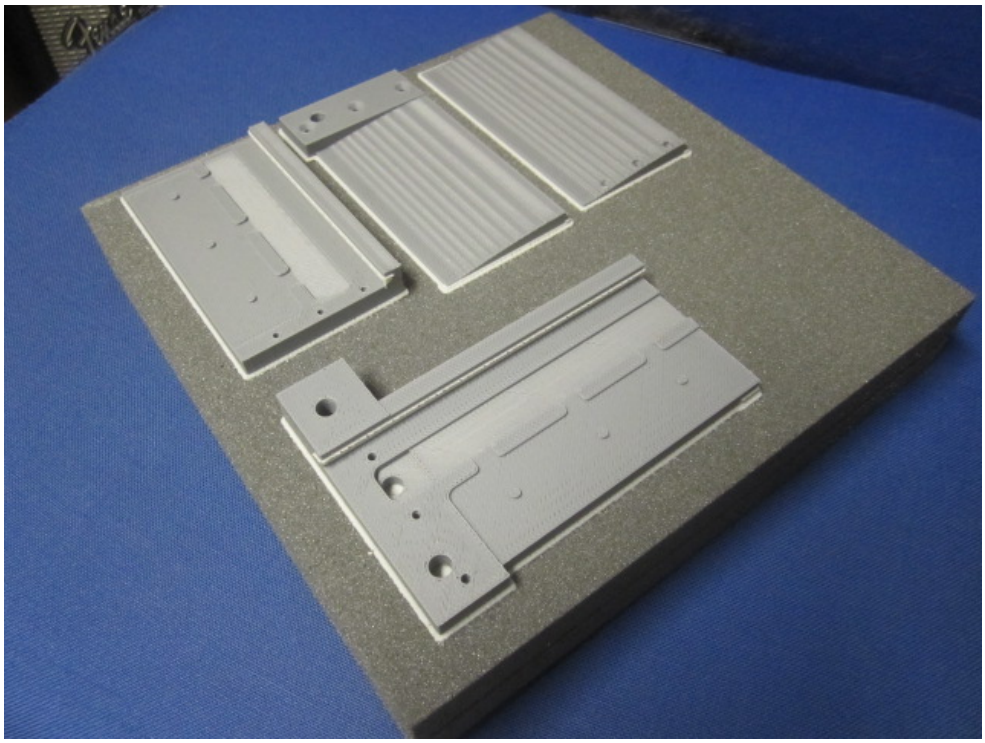

Figure 7. Rapid prototyped Alstom foil for preliminary testing

After preliminary testing of the foil, it was determined that a 0.5 mm shim adhered to one side of the 1 mm slot worked best to distribute the air flow uniformly along the slot length. With 0.17 mm of adhesive, this produced a ventilation slot width of 0.33 mm.

Testing of the Alstom foil paralleled that conducted for the SAFL foil, namely oxygen transfer testing and bubble size and velocity measurement. As with the SAFL foil, tests were conducted for 15 testing combinations of test section velocity, angle of attack, and ventilation air flow rate. The gas transfer test program employed the entire slot length. Details on the gas transfer test methodology are given elsewhere in this report. Again, mirroring the SAFL foil test program, bubble size and velocity were measured after blocking all but the center 5% portion of the ventilation slot using a back lit bubble shadow imagery technique. (See Figs. 7-9.) 1000 double frame images were acquired and analyzed with Matlab based software for bubble size analysis and Lavision PIV software (DaVis 7.2) for bubble field velocity. Details of the bubble sizing and velocity measurement methodologies are described in detail elsewhere.

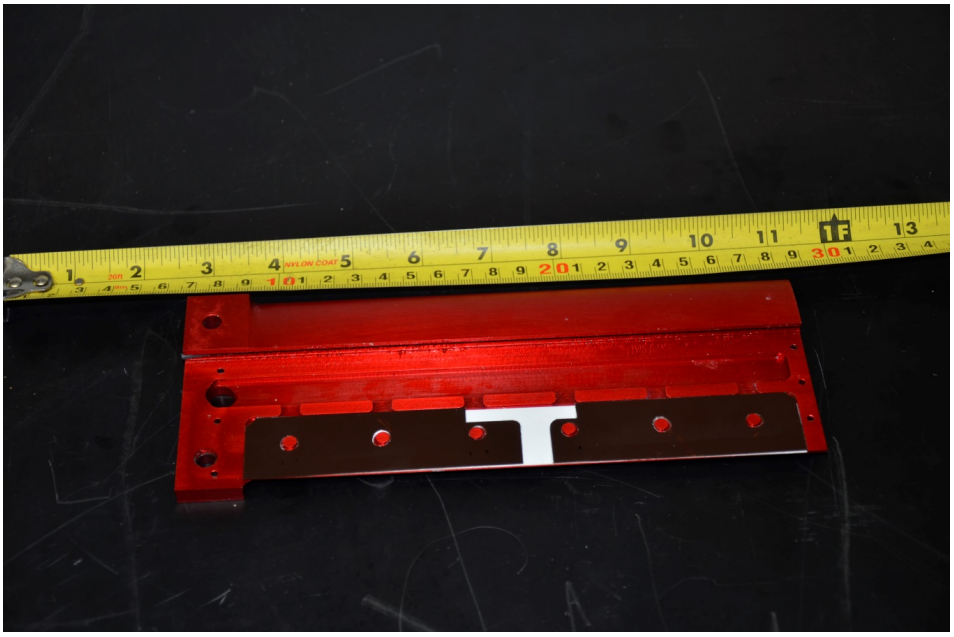

Figure 8. Disassembled Alstom foil with shims blocking all but 5% of slot length for use with high speed imagery

Figure 9. Close-up of Alstom foil interior with blocking shims

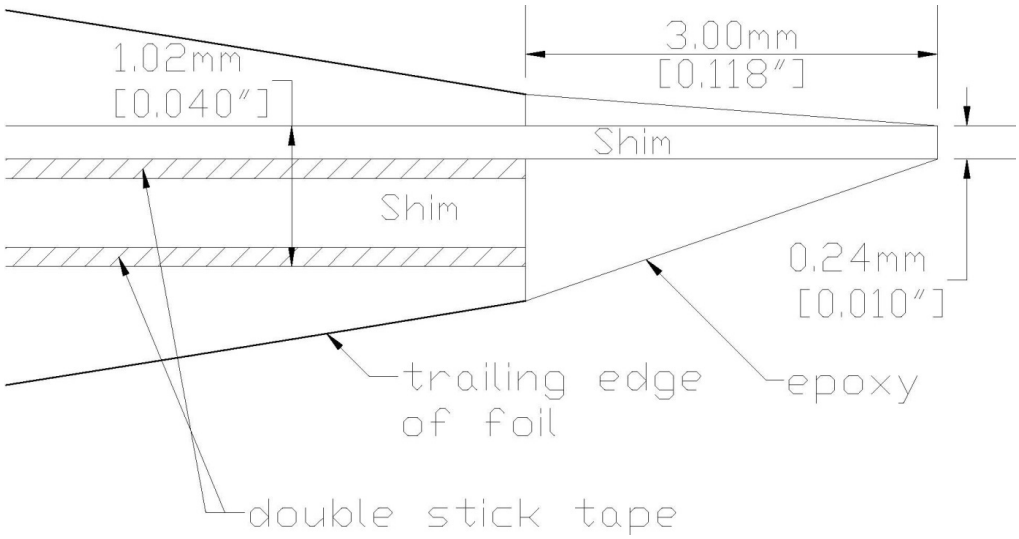

Figure 10. Alstom foil, trailing edge detail showing extended blocking shim and epoxy fill

Figure 11. Alstom foil with extended blocking shims and epoxy filling of trailing edge

4. Particle Shadow Velocimetry

Particle Shadow Velocimetry (PSV) employs direct in-line volume illumination using low power sources such as LED arrays and an optical setup to produce a narrow depth-of-field for 2D plane imaging. Figure 12 shows a schematic of the experimental setup as has been reported previously by Karn et al. (2015a). A 1K × 1K pixel Photron APX-RS camera (capable of 3000 frames/s at full sensor size) with a 60 mm telephoto lens was used to acquire images. A custom-made pulsed

LED light source from Innovative Scientific Solutions Inc. was used to illuminate the flow, with the pulsed array having flash rates up to 10 kHz, a 5 μs minimum pulse width and rise and fall times around 200 ns. To improve the uniformity of the back-lighting in the images, a light shaping diffuser was placed between the light source and the flow.

In the PSV technique, two LED light pulses separated by a short duration are synchronized with camera exposures in order to obtain two consecutive (or, double) images. In our experiments, the time duration between two pulses varied between 100-230 μs depending upon the free stream velocity. Using the image pairs, the instantaneous velocity field of the bubbles was obtained using commercially available Particle Image Velocimetry (PIV) software (DaVis 7.2 from LaVision). The image pairs were captured at a double-frame rate of 25 image-pairs/s and the exposure time for individual images is set to 15 μs to prevent blurring in the images. A data set consisted of 1000 image-pairs taken over a period of 40 s. The field of view (FOV) of the captured images was approximately 60 mm × 60 mm. The imaging system was calibrated prior to the beginning of the experiments using a grid with line spacing of 2.5 mm × 2.5 mm covering the entire field of view located at the water filled test section centerline. Calibrated pixel dimensions were 0.059 mm in both dimensions. The image depth of field was approximately 10 mm and the focus plane was at the test section centerline. The lateral (spanwise) spread in the bubble plume was measured at the measurement locations and the calculated uncertainty in bubble size and velocity due to out-of-plane location uncertainty was 1.6% near the foil and 3.2% at the most downstream location (i.e. 377 mm). The bubble sizes were in the range of 2 to 68 pixels, which correspond to bubble diameters of 0.12 to 4 mm. (The term 'size' and 'diameter' are used interchangeably in this document.)

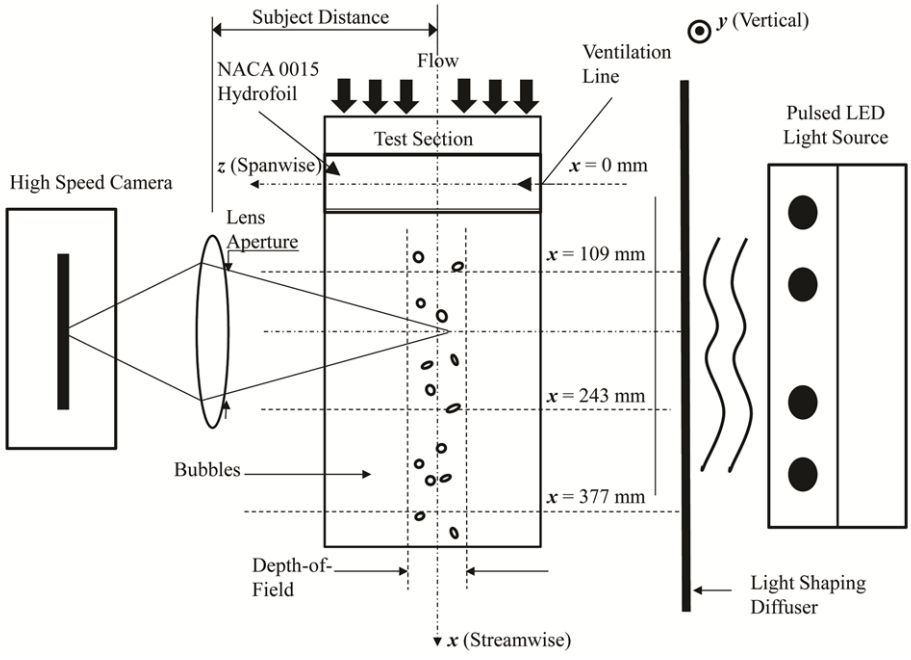

Figure 12: Schematic of the experimental setup for shadow imaging of bubbly flows in an aerated hydrofoil wake.

IV. Image Analysis

1. Image Analysis Technique

Figure 13 provides a sample bubble image from our experiments. The bubbly wake was characterized by a wide bubble size distribution ranging from microbubbles to large bubble clusters. The bubbles could be either in-focus or out-of-focus. An image analysis technique, as described in Karn et al. (2015a), was employed to extract the information about the bubble locations and the bubble sizes from the bubble images. It consisted of three major steps. First (1), the original grayscale images were binarized. This was followed by (2) categorization of bubble regions. The bubble regions were labeled and characterized by a series of metrics including area, centroid, major and minor radius (projected bubbles were assumed to be ellipses) and circularity factor. Based on the area of each region, the bubbles were divided into tiny spherical bubbles, intermediate-sized bubbles and large bubbles or clusters. Lastly (3), bubble separation and information extraction was performed. A multilevel segmentation approach was used to extract the bubble locations and dimensions from the images. 'Cluster Processing' using advanced morphological operations and a "watershed transform" extracted individual bubbles from bubble clusters. The information for all identified bubbles including their x and y-coordinates and minor and major radius was then tabulated.

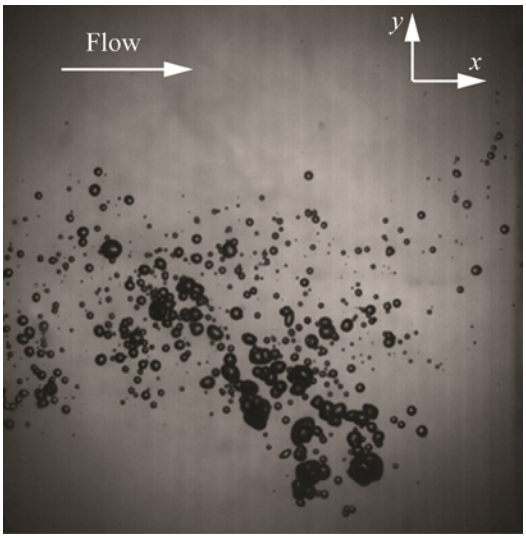

Figure 13: A sample bubbly wake image obtained in shadow imaging experiments.

2. Validation of Image Analysis Technique

The bubble information extracted from our image analysis was used to estimate the ventilation flow rate during the experiments, which in turn was compared with the ventilation rate set by the mass flow controller to validate the efficacy of our image analysis technique as shown in Figure 14.

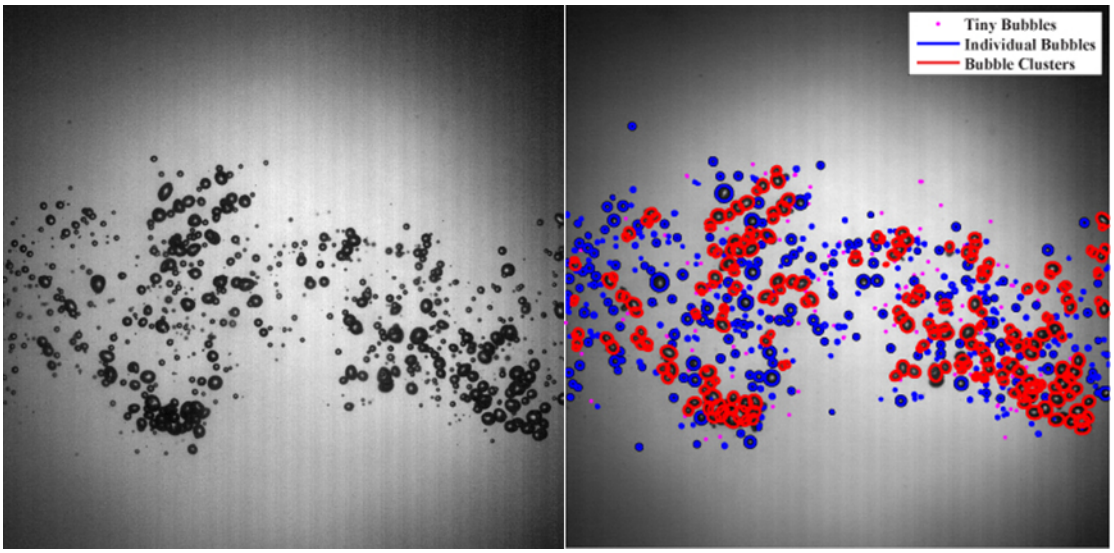

Figure 14. (a) A bubble image from the experiment, and (b) the same image after undergoing image processing. Note that all the bubbles in the image are captured by the image analysis technique.

Air absorption in the bubbly wake was neglected considering the small time-scales (<< 1s) between air injection and image capture. The estimation of ventilation air flow rate from bubble images consisted of three steps: (1) extract 2D bubble size information, (2) derive the volume and velocity of individual bubbles, and (3) calculate the volume flow rate from the volume and velocity information of all the bubbles accounting for the changes in pressure and temperature.

In the first step, the extraction of 2D bubble information was accomplished by the proposed image-processing technique. In this step, the semi-major axis (a) and semi-minor axis (b) lengths of the elliptical bubbles were determined. Second, an elliptical bubble was rotated around its major axis to obtain a prolate spheroid or an ellipsoid of revolution. Then, the volume of this prolate spheroid was determined as $(4\pi/3)b^2a$. Figure 15 presents the mean streamwise velocity of bubbles in the wake obtained using the SIV technique described previously. As can be seen in Figure 15, the bubble velocities in the wake remain almost constant in the streamwise direction. It is noteworthy that non-symmetric velocity fields are observed having higher velocities above the centerline, even at test conditions of zero angle of attack. This is due to the fact that the ventilated air was injected from the suction side of the hydrofoil which was located on the bottom of the foil.

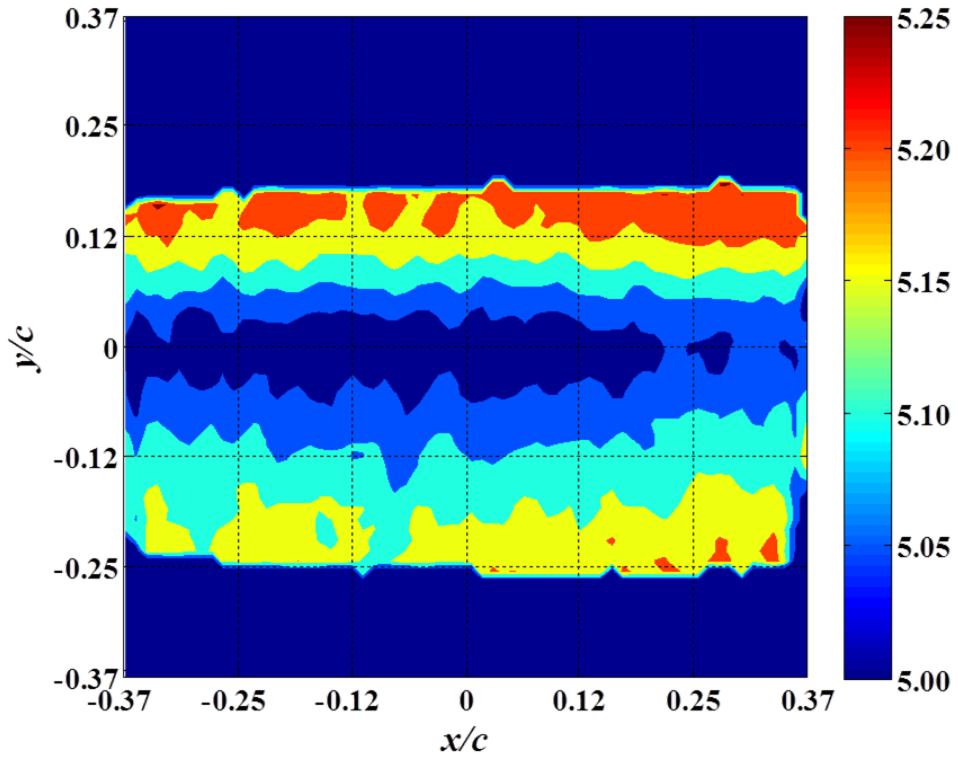

Figure 15: The mean horizontal velocity field obtained using PSV technique (The origin in this contour plot is located at a distance of 377 mm from hydrofoil center of rotation). The units on the color bar are m/s.

Finally, in the third step, the volume and velocity information of all the bubbles were used to calculate the volume flow rate. To compare with the corresponding volumetric flow rate at standard temperature and pressure as set by the mass flow controller (also known as mass flow rate), the volume flow rate measured from bubble images was adjusted with respect to the pressure and temperature in the test-section. In our experiments, the images were captured at three different downstream locations and the ventilation flow rate was measured using the above procedure at each of them. Finally, steps 1 and 2 were repeated for all bubbles to obtain a total air flux for one single image. This expression is given by

$$\dot{Q}_{total} = \frac{\beta^3}{M} \sum_{k=1}^{M} \dot{Q}_{single,k} \tag{1}$$

$$\dot{Q}_{single} = \sum_{i=1}^{N} \left(\frac{u_i}{w}\right) \left(v_i \times \frac{P_{TS}}{P_0} \times \frac{T_0}{T_{TS}}\right) \tag{2}$$

$$v_i = (4\pi/3) a_i b_i^2 \tag{3}$$

where M and N denote number of images over which averaging is done (M = 1000 for our experiments) and the total number of bubbles in a single image, respectively, β represents the pixel dimension and w refers to the width of a single bubble image (1024 pixels or ~60 mm). u_i

and v_i are the velocity and volume of individual bubbles, respectively. Finally, P_0 and T_0 correspond to standard temperature and pressure, and P_{TS} and T_{TS} are the measured pressure and temperature in the test-section. The volume flow rate thus derived was then averaged over all 1000 images to obtain the mean value of bubble image derived air flux. Figure 16 shows the mean ventilation rates calculated at each of the three downstream locations for a single test condition.

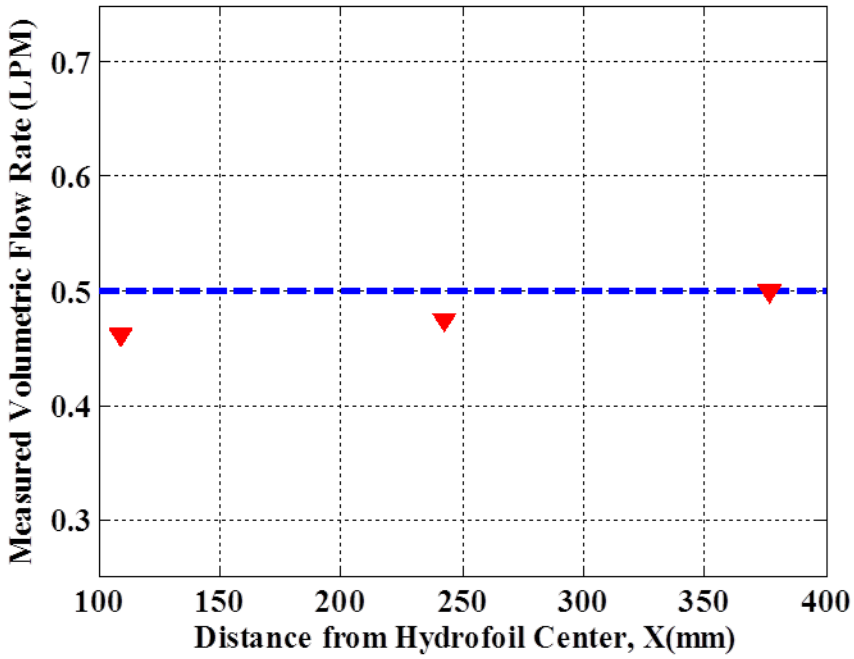

Figure 16. Volumetric flow rates from bubble measurements as a function of downstream distance in the bubbly wake compared with the input flow rate of 0.5 SLPM (shown in blue)

As can be seen, the mean ventilation volumetric flow rates calculated from the bubble images compare well with the actual volumetric flow rate of 0.5 SLPM., the difference within 9% of the actual value at all the three downstream locations. As the presence of bubble clustering reduces in the downstream direction, the mismatch decreases to less than 1%. Larger mismatch occurring closer to the hydrofoil is likely to be associated with the higher uncertainty in extracting bubble information from very dense bubble clusters. The clustering of the bubbles underestimates the volumetric flow rate as bubble images coincide, i.e. the bubbles hide one another. This shows that the accuracy of the image processing technique decreases with increased clustering.

3. Adjustments to Image Analysis Technique for Alstom Foil Bubbles

Small adjustments to the image analysis algorithm needed to be made for the Alstom foil. As soon as the gray scale image was read into MATLAB, it was converted to a binary image. In the binary image, the pixels that are a part of a bubble are represented as a 1 and pixels that are not a part of a bubble are represented by a 0. This conversion from a gray scale image to a binary image was done by extended H-minima transform (Karn et al 2015a). This transform requires a

threshold value for the conversion to binary images. This threshold was applied to the difference in grayscale intensity values of background and the bubble shadows, and was therefore robust in recognizing the bubble shadow regions for a particular test case. However, the threshold value did need to be adjusted when Alstom foil images were analyzed since the Alstom bubbly wake varied considerably in both the streamwise and cross stream directions. In addition to threshold adjustment, in cases where the Alstom foil produced very large bubbles, the intermediate bubble selection algorithm was removed from the processing. In visual reviews of bubble selection results, it was found that large bubbles were often selected by the intermediate size algorithm as multiple smaller, very ellipsoidal bubbles. Removing the intermediate selection algorithm meant that a small number of intermediately sized bubbles would be missed, but the larger bubbles were selected correctly. This was done for 9 of the 45 image sets.

V. Numerical Simulations

Since the development of a computational tool capable of performing large eddy simulation of two-phase two-way coupled bubbly flows is of interest, the proper filtered form of the governing equations has to be extracted and employed. The derivation process accompanied by interfacial momentum forces as well as sub grid scale modeling will be explained in section 1. The details of numerical method and discretization schemes are presented in section 2.

1. Governing Equations

1.1. Filtered two-fluid model equations

Since the governing equations and numerical approaches to tackle the two-phase problems are not unique, i.e. different governing equations are derived for different numerical approaches, an important phase of the project is to employ the proper sets of equations. A detailed exposition of different averaging methods, including ensemble averaging, time averaging, statistical averaging and volume averaging, is provided by Drew and Passman (1999) and the filtering procedure of multi-fluid formulation is covered by Lakehal et. al. (2002). Here, we summarize the relevant results that pertains to our work.

The basic idea in volume averaging in multi-phase flow is to describe the motion of flow in terms of the phase-averaged variables, since multiple phases may be present at each point. This process leads to the macroscopic description of the motion of flow known as instantaneous phase-averaged equations, i.e. each phase is seen as a continuum. For the turbulence modeling another averaging is required which leads to a double averaging applied to the original microscopic equations. For this project we have employed a formulation by performing a single component-weighted volume averaging procedure which leads to filtered two-fluid equations. This procedure, which employs a spatial filter function, requires a single averaging instead of double averaging (ensemble-space or space-space) over the component weighted Navier-Stokes equations. The topological equation $\frac{D}{Dt}\chi^{k} = 0$ is used to describe the motion of the interface, where D/Dt is the total derivative with the interface velocity as the advection velocity. χ^{k}, is known as phase indicator function which is shown schematically in Figure 17.

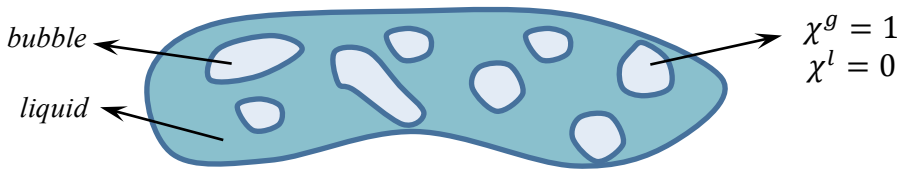

Figure 17. Definition of phase indicator function

Multiplying the microscopic Navier-Stokes equations by the phase indicator function and provoking the topological equation yields the microscopic component-weighted set of equations in continuum format. In this work, the standard low pass filtering operation on a function *f(x,t),* defined in Pope (2000), is employed to gain the filtered field represented by $\overline{f(x)}$. Applying the

filtering operation on the microscopic component-weighted form of equations yields the filtered form of the two-fluid model (TFM) equations, as below

$$\frac{\partial}{\partial t}(\alpha^k \tilde{\rho}^k) + \nabla.(\alpha^k \tilde{\rho}^k \tilde{u}^k) = \Gamma^k \tag{4}$$

$$\frac{\partial}{\partial t}(\alpha^k \tilde{\rho}^k \tilde{u}^k) + \nabla.(\alpha^k \tilde{\rho}^k \tilde{u}^k \otimes \tilde{u}^k) = \nabla.\left[\alpha^k(\tilde{\Pi}^k - \tau^k)\right] + \alpha^k \tilde{\rho}^k \vec{g} + M_k + \sigma_k \tag{5}$$

Here, α^k is known as void fraction of phase k, defined as $\alpha^k = \overline{\chi^k}$. $\tilde{\rho}^k$ is the filtered component weighted density, defined as $\tilde{\rho}^k = \overline{\chi^k \rho^k}/\alpha^k$. $\tilde{u}^k$ is the filtered mass weighted (Favre) averaged velocity vector for phase k, defined as $\tilde{u}^k = \overline{\chi^k \rho^k u^k}/\overline{\chi^k \rho^k}$. Γ^k is the interfacial mass source term, defined as $\Gamma^k = \overline{\rho(u-V).\nabla\chi^k}$. σ^k is the interfacial momentum source term, defined as $\sigma^k = \overline{\rho u(u-V).\nabla\chi^k}$. Similar to the single phase flow, τ is the sub grid stress tensor for unresolved scales, defined as $\tau_{ij}^k = \rho^k(\widetilde{u_i u_j} - \tilde{u}_i^k \tilde{u}_j^k)$, which needs modeling for both phases. M_k is the interfacial momentum transfer term due to interface forces and defined as $M_k = -\overline{\Pi.\nabla\chi^k}$. The interfacial mass and momentum source terms are assumed negligible, i.e. $\Gamma_k = 0, \sigma_k = 0$. The effect of viscous molecular and turbulent stresses can be combined and represented as effective viscosity μ_{eff} which is used to relate the stress to the strain rate.

1.2. Interfacial momentum source terms

The interfacial momentum transfer term M_k encapsulates the effect of the forces exerted on each phase by presence of other phase. It is customary to decompose the total momentum transfer term into several terms, mainly drag, lift, virtual mass and turbulent dispersion forces, i.e. $MG = F_D + F_L + F_{VM} + F_{TD}$. In this work we have considered all of the mentioned interfacial forces.
The drag force has the dominant contribution, among other forces, to the interphase forces in bubbly flows. It represents the resistance force felt by a bubble as it moves steadily in the surrounding liquid. We employed the standard approach to model the drag force in bubble swarm.

The drag force has an empirical drag coefficient C_D which shows the intensity of the drag force. Based on the flow regime, different expressions are proposed for the drag coefficient. For instance, for the bubble column test case, the flow regime is in the distorted region, therefore the drag coefficient is estimated by $C_D = \frac{2}{3}\sqrt{EO}$. EO is the Eotvos number defined as $EO = g(\rho_L - \rho_g)d_B^2/\sigma$.

Lift force is the resultant of movement of a bubble through a fluid that is in shearing motion. The lift force is normal to the relative velocity, due to circulation of the liquid around the bubbles. A comprehensive study on the lift force in bubbly flows is carried out by Hibiki and Ishii (2007). Similar to drag coefficient, lift coefficient C_L has to be assumed prior to the calculation. There is no consensus on the lift coefficient, but it is usually taken as $C_L = 0.5$. We have also considered $C_L = 0.5$ in this project.

The virtual mass force is a result of a moving bubble through a fluid, while it accelerates. The bubble tries to accelerate some of the surrounding fluid as it accelerates. This results in an interaction force trying to decelerate the bubble motion while accelerating the surrounding fluid.

The virtual mass coefficient is taken as $C_{VM} = 0.5$ for dilute suspensions of spheres in a fluid, as in our project.

The last interfacial force we have considered is known as turbulent dispersion force. To account for influence of turbulent eddied, the idea of turbulent dispersion has been developed by Lopez De Bertodano (1994). Turbulent fluctuations results in dispersion of phases from high volume fraction regions to low volume fraction regions. The turbulent dispersion force is modeled as a resultant of gas holdup gradient, turbulence intensity, slip velocity and the bubble Schmidt number Sc usually taken as Sc = 1. It is worth noting that all of the above mentioned interfacial momentum forces are nonlinear and as a result make the gas momentum equation computationally costly.

1.3. Model simplification

The set of equations for Euler-Euler bubbly flows are cumbersome, computationally, since they have to be solved in a coupled manner with non-linear terms. Also, a major challenge in the two-fluid models is the calculation of the pressure field, since an explicit equation for pressure calculation does not exist. It is more complicated than single-phase flows because now two-continuity equations have to be combined with the momentum equations. As a result, unlike the pressure equation in single-phase flows which is linear, the derived pressure equation is quadratic which requires more additional iterations per time step. Hence, employing an efficient computational procedure is significant. In our work, we have followed the work of Sokolichin and coworkers to simplify the filtered equations which is more appropriate for computational simulation of dilute bubbly flows. The model is based on mixture equations in terms of the liquid and gas density and velocity fields. Under certain conditions, valid for the dilute bubbly flows, the mixture equations can be simplified to a more tractable form. For the liquid phase, the mixture equations are solved and accounted for the liquid phase variables. Adding up the filtered momentum and mass balance equations for gas and liquid phases yields the set of equations known as mixture equations. Note that the interaction momentum term is canceled out by performing the summation. For the dilute gas/liquid environment, the mixture equations can be simplified further. Owing to the fact that $\rho_G \ll \rho_L$ some terms pertaining to the ratio of gas/liquid density can be ignored without much loss of accuracy. Also, for dilute bubbly flows, with sufficiently small gas holdups, the mixture quantities can be approximated by the liquid quantities, i.e. $\rho_m = \rho_L$ and $u_m = u_L$, where the subscripts m and L denote the mixture and liquid phase properties, respectively. We can also assume the liquid density to be constant in all terms except the bouyancy term. This is similar to the Boussinesq approximation in the modeling of free convection problems in single-phase flows. Hence, the mixture balance equations can be simplified as follows:

$$\nabla.(u_L) = 0 \tag{6}$$

$$\frac{\partial}{\partial t}(\rho_L u_L) + \nabla.(\rho_L u_L \otimes u_L) = -\nabla.\tau_m - \nabla p + (1-\alpha_G)\rho_L g \tag{7}$$

The simplifications made, specifically the incompressibility of the liquid phase, reduces the computational cost of the numerical simulation since the classical numerical methods for single-phase can be employed for calculation of pressure and liquid velocity. The simplified mixture momentum has an extra term, compared to single-phase problems. The last term on the right

hand side represents the gravitational force which is proportional to the local gas holdup. For the gas phase we use the original filtered equations (Eqs. 4 and 5) with slight modification in the mass balance equation to account to turbulent mixing effect known as bubble path dispersion. As mentioned by Sokolichin (2004), the bubble path dispersion results from the interactions between the bubbles and from the influence of the liquid phase turbulence on the bubbles. In other words, the movement of bubbles in the liquid phase generates some level of turbulence in the liquid phase. The generated turbulence, in turn, affects the behavior of the neighboring bubbles. This effect is even more important in low gas holdups and small bubble sizes. In our work, the effect of bubble path dispersion is modeled through a diffusion like term on the right hand side of the gas mass balance equation. To calculate the gas density, an equation of state is required. The ideal gas law is used to calculate the gas density in this work, i.e. $\rho_G = p/RT_0$. R is the specific gas constant, 287.04 J/kgK°, and T is the absolute temperature in Kelvin degrees.

In this work we have employed the partially-transformed equations in curvilinear coordinate to benefit the flexibility of simulating flow in domains with non-uniform non-orthogonal computational cells, such as simulation of flow around hydrofoil. The compact tensorial form of the simplified filtered balance equations in the generalized curvilinear coordinates ξ_j read as below

$$J\frac{\partial U_L^j}{\partial \xi_j} = 0 \tag{8}$$

$$\begin{aligned}\frac{\partial}{\partial t}\left(\rho_L U_L^q\right) = \frac{\partial \xi_q}{\partial x_i}\left[\frac{\partial}{\partial \xi_j}\left(-\rho_L U_L^i U_L^j\right) + \frac{\partial}{\partial \xi_j}\left(\frac{\mu_L}{J} g^{jk}\frac{\partial u_L^i}{\partial \xi_k}\right)\right] + \\ \frac{\partial \xi_q}{\partial x_i}\left[\frac{\partial}{\partial \xi_j}\left(\frac{\mu_L}{J}\frac{\partial u_L^m}{\partial x_i}\frac{\partial \xi_j}{\partial x_m}\right) + \frac{1}{J}(1-\alpha_G)\rho_L g_i\right] - \frac{1}{J} g^{jq}\frac{\partial p}{\partial \xi_j}\end{aligned} \tag{9}$$

$$\frac{\partial}{\partial t}(\alpha_G \rho_G) = J\frac{\partial}{\partial \xi_j}\left(-\alpha_G \rho_G U_G^j\right) + J\frac{\partial}{\partial \xi_j}\left(\frac{1}{J} g^{jk}\frac{\rho_g}{\rho_L}\frac{\mu_L^{turb}}{S_c}\frac{\partial \alpha_G}{\partial \xi_k}\right) \tag{10}$$

$$\begin{aligned}\frac{\partial}{\partial t}\left(\alpha_G \rho_G U_G^q\right) = \frac{\partial \xi_q}{\partial x_i}\frac{\partial}{\partial \xi_j}\left(-\alpha_G \rho_G U_G^i U_G^j\right) - \frac{1}{J} g^{jq}\alpha_G\frac{\partial p}{\partial \xi_j} + \frac{1}{J}\frac{\partial \xi_q}{\partial x_i}(M_G)_i \\ + \frac{\partial \xi_q}{\partial x_i}\left[\frac{\alpha_G \mu_G}{J} g^{jk}\frac{\partial u_G^i}{\partial \xi_k} + \frac{\partial}{\partial \xi_j}\left(\frac{\alpha_G \mu_G}{J}\frac{\partial u_G^k}{\partial x_i}\frac{\partial \xi_j}{\partial x_k}\right) + \frac{1}{J}\alpha_G \rho_G g_i\right]\end{aligned} \tag{11}$$

In the above equations, J is the Jacobian of transformation, u_G^i and u_L^i are the ith component of the filtered Cartesian velocity of gas and liquid phase, respectively. U_G^i and U_L^i are the contravariant volumetric flux of gas and liquid. g^{ij} is the contravariant metric tensor. μ_G and μ_L are the effective viscosities of both phases.

1.4. Turbulence modeling

As mentioned earlier, the effective viscosity, is typically decomposed into molecular viscosity and turbulent viscosity. In two-phase bubbly flows, the turbulent stress is generated by two separate mechanisms, namely shear induced turbulence and bubble-induced turbulence, i.e. $\mu_{eff} = \mu_m + \mu_{SI} + \mu_{BI}$.

Shear-induced turbulence, which is independent of existence of bubbles, is sustained by the action of shearing on a fluctuating velocity field. Bubble-induced turbulence is a result of bubble agitation in bubbly flows. The approach to model the turbulence effects are explained in the subsequent sections. It is worth noting that the turbulence in the gas phase is assumed to be in equilibrium with the liquid turbulence. In other words, the gas phase follows the liquid phase in the SGS level, i.e. $\rho_L \mu_{eff,G} = \rho_L \mu_{eff,L}$.

To close the filtered equations of the two-fluid model (TFM), a model is required to approximate the sub-grid stresses. The sub-grid stresses are key factors in bubbly turbulent flows as they model the unresolved dissipative scales of motion. In this work, we have employed the dynamic procedure of Germano to evaluate the eddy viscosity. In the eddy viscosity concept, the sub-grid stresses of phase *k* are related to the resolved strain rate tensor by introducing the turbulent viscosity which is calculated by the Smagorinsky model. For details the reader is referred to the work of Germano et. al. (1991). In our work, we have employed the box filter taken as the average grid spacing of a computational cell, i.e. $\widetilde{\Delta} = \sqrt[3]{V}$ (V is the volume of the computational cell).

In bubbly flows, the interaction of bubbles with turbulent eddies makes another source of turbulence in the liquid phase, known as bubble-induced turbulence. Several approaches have been proposed in the literature for modeling the additional eddy viscosity as a result of BIT. The simplest model was proposed by Sato and Sekoguchi (1981). The Sato model is based on the bubble diameter as the length scale. Milelli et. al. (2001) employed the Sato model but used a different length scale for BIT based on the mixing length of the dispersed phase. The model reads

$$\mu_{BI} = C_s \widetilde{\Delta} \rho_L \alpha_G |u_G - u_L| \tag{12}$$

We have implemented both models of Sato and Milelli in our code but found Milelli model a better fit for available experimental results in two-phase bubbly flows.

1.5. Near-wall boundary condition

Resolving all the turbulent scales of motion near solid walls in turbulent bubbly flows requires very fine mesh and often computationally impractical. The reason is the presence of very small but energetic coherent structures in the viscous sublayer which have to be resolved. This problem is more pronounced in the hydrofoil simulation since the Reynolds number is very high. To address this numerical issue, wall models have been proposed. In this work we have employed "equilibrium stress balance" wall model developed by Cabot and Moin (2000).

The model is categorized as "wall stress models" and is based on turbulent thin boundary layer equations. The eddy viscosity is approximated by the simple mixing-length model with near-wall damping as

$$\frac{\nu_t}{\nu} = \kappa l^+ \left(1 - e^{-l^+/19}\right)^2 \tag{13}$$

where $l^+ = u_\tau l/\nu$ is the dimensionless distance from wall and u_τ is known as the local instantaneous shear velocity. The full thin boundary layer equation can be simplified to get the

"equilibrium stress balance" model. As a result, it reduces to an ordinary differential equation which can be integrated from the wall to the first off-wall computational node. Newton method is employed to solve, iteratively, the algebraic equation to obtain the shear velocity. Our experience shows that usually 4-5 iterations suffices to get a converged solution. Once the shear velocity is calculated, the tangential component of the velocity vector at the ghost node (exterior to domain) of the first off-wall node is calculated. It is worth mentioning that the normal component of the velocity at the ghost node is obtained by imposition of zero flux across the boundary, i.e. $(\tilde{u}_l)_{ghost} = -(\tilde{u}_l)_{\delta}$.

1.6. Solution procedure

In this section, we present the procedures we followed to solve the governing equations. To advance the solution for each time step, the procedure is done in 7 steps, as below

1) The shear-induced eddy viscosity of the liquid phase is calculated using the liquid velocity field of the previous time step. First, the Smagorinsky coefficient is calculated by the dynamic procedure of Germano. The Smagorinsky coefficient is then used to calculate the shear-induced eddy viscosity.
2) The eddy viscosity corresponding to the bubble-induced turbulence is calculated by the algebraic Equation (12).
3) The liquid mass and momentum, Equations (8) and (9), are coupled to solve for the liquid velocity vector and pressure field. The coupling is done via the standard fractional step method developed for single-phase flow, except with the additional buoyancy term. The buoyancy term is evaluated with the gas holdup of the previous time step.
4) The gas density field is calculated by the algebraic ideal gas law, using the pressure obtained in step 3.
5) The gas momentum Equation (11) is solved, using the calculated liquid velocity and pressure field from step 3.
6) The gas mass balance Equation (10) is solved to obtain the fresh void fraction field.
7) Check the convergence of void fraction field. If converged, proceed to next time step, otherwise go to step 1 and redo the steps with the fresh gas holdup.

The condition for convergence of the gas holdup is defined as when the change in infinity norm of the initial gas holdup in step 3 and fresh gas holdup in step 6 is less than a certain amount. In our work we considered $\epsilon = 10^{-6}$ as the condition, i.e. $\left\|(\alpha_G)_{initial} - (\alpha_G)_{fresh}\right\|_{\infty} \leq 10^{-6}$. In the present work, the solution procedure converges after 2 or 3 iterations.

2. Numerical Method

We divide the solution procedure into three different flow solvers. The first step is calculation of pressure field and liquid velocity. The second step is the gas momentum balance and the third step is gas mass balance equation solver. In the following sections, all aspects of our numerical approach are provided.

2.1. Pressure and liquid velocity solver

The fractional step method of Ge and Sotiropoulos (2007) is employed to integrate in time the momentum and mass balance equations of the liquid phase (Eqs. 8 and 9). Here, the buoyancy term corresponding to the local gas holdup should also be added to the right hand side of the momentum equation. In the first step of the fractional step method, an intermediate liquid flux field U_L^* is computed through momentum equation solution. The Crank-Nicolson scheme is used for temporal discretization and second order central scheme is employed for the spatial discretization. The Jacobian-free Newton-Krylov method is used to solve the momentum equation with the GMRES method as the solver for the linearized system. The obtained liquid flux field does not satisfy the mass balance condition, in general. So the pressure correction Poisson equation is solved to obtain the pressure correction $\Pi = p^{n+1} - p^n$ with the Neumann boundary condition $\frac{\partial \Pi}{\partial n} = 0$ imposed on the boundary. Second order central differencing scheme is employed to discretize the above equation. The GMRES method with the algebraic multigrid, as the preconditioner, is employed to solve the pressure correction. For details of the implementation the reader is referred to work of Kang and coworkers, our former group member. Once the pressure correction field is calculated, the pressure field is updated by $p^{n+1} = p^n + \Pi$ and the liquid flux vector is projected onto the divergence-free.

It is worth mentioning that the fractional step method is implemented in hybrid staggered/non staggered method of Ge and Sotiropoulos in curvilinear coordinates. It can be shown that the above implementation yileds 2nd order accurate velocity field in time and space, and 1st order accurate pressure field in time and 2nd order in space.

2.2. Gas momentum solver

Once the pressure and the gas density are obtained, the gas momentum Equation (11) can be discretized and solved for the gas flux field U_G. The Crank-Nicolson discretization is employed to solve for the gas flux field. Similar to liquid phase momentum solver, the Jacobian-free Newton-Krylov method with GMRES as the linear solver is employed to solve the resulting system of equations. According to Sokolichin and coworkers (1997), due to existence of discontinuities in the gas holdup field first-order upwind scheme for calculation of the convective flux is usually employed. The first order upwind leads to huge numerical dissipation and reduces the whole accuracy of the solution to 1st order accurate. Second order accuracy of the scheme can be retained by employing a second order central scheme in smooth regions but switches the scheme to monotone upwind scheme near discontinuities. These schemes are known as total variation diminishing (TVD) schemes. In this work, we have employed a TVD scheme with superbee flux limiter. The scheme is written as below

$$F_{i+1/2}^{TVD} = F_{i+1/2}^{UP} + \phi_{i+1/2}(F_{i+1/2}^{CS} - F_{i+1/2}^{UP}) \tag{14}$$

Where $F_{i+1/2}^{TVD}$, $F_{i+1/2}^{UP}$ and $F_{i+1/2}^{CS}$ denote the corrected flux with a limiter, the upwind flux and the central difference flux, respectively, at the cell face $i + 1/2$. ϕ is the *superbee* flux limiter defined as $\phi(\theta) = \max[0, \min(1,2\theta), \min(2, \theta)]$. θ is the ratio of the slope at the neighboring interface in the upwind direction to the slope of the current interface. Second order central differencing scheme is employed for discretization of all other terms in the right hand side of the gas momentum equation. Similar to the liquid momentum equation, the hybrid staggered/non staggered formulation is employed.

2.3. Gas mass solver

The second-order Crank-Nicolson scheme is used to temporally discretize Equation (13). To retain the second-order accuracy in space, TVD scheme with superbee flux limiter is employed to discretize the advective term, while second order central differencing is used for the turbulent dispersion term. The existence of outflow boundary condition (for the hydrofoil and bubble column problems) for the gas phase poses a numerical issue known as violation of compatibility condition. At the outflow boundary, the gas momentum and mass balance equations are not solved, rather they are extrapolated from the interior solution. As a result, the global integral gas mass may not be conserved. As such, the gas mass balance Equation (10) would be ill-posed because of drainage/accumulation of mass inside the computational domain. To remedy this problem, we propose a correction of gas holdup inside domain based on local volume-weighted void fraction. Integration of the gas mass balance equation over the domain and applying the divergence theorem yields

$$RES = \frac{\partial}{\partial t}\int_{\Omega} \alpha_G \rho_G d\Omega + \int_{\Gamma} \alpha_G \rho_G (u_G . \hat{n}) d\Gamma - \frac{1}{Sc}\int_{\Gamma} \nu_L^{turb} \rho_G \frac{\partial \alpha_G}{\partial \hat{n}} d\Gamma \tag{15}$$

$\hat{n}$ is the unit vector normal to the boundary and is the domain bounded with boundary Γ. Integration of gas mass balance equation may not be zero in the case of an outflow boundary condition, hence leaving a residual RES. To make the residual zero at each time step, we distribute the mass drainage/accumulation RES over the domain by modifying the gas holdup in the domain, i.e.

$$(\alpha_G)_{modified} = \left(1. - \frac{RES}{\int_{\Omega} \alpha_G \rho_G d\Omega}\Delta t\right)\alpha_G \tag{16}$$

This approach prevents the growth of mass deficit in the domain. It is worth noting that, computationally, the gas density, void fraction and pressure are defined at cell centers, while the liquid and gas fluxes are defined at the cell faces.

Based on the mathematical formulation explained in section IV.1 and the numerical methods explained in section IV.2, the coding of the computer program was implemented in parallel C language accompanied by the efficient PETSC and BoomerAMG libraries. PETSC was employed for efficient parallel linear and non-linear Krylov sub-space solvers. BoomerAMG provides powerful algebraic multigrid as a preconditioner for the GMRES method.

VI. Results and Discussion

1. Bubble Measurements

1.1. Application of image analysis technique to a reference test case.

Bubble size, shape and velocity data were processed using the techniques previously described. From those results, a reference case (angle of attack = 0^o, water velocity = 5 m/s, air flow rate = 0.5 SLPM, position = 377mm or 4.7c downstream from foil center, c = cord length) was chosen and is described here. Figure 18 shows typical bubble size and shape distributions observed in the wake for the reference case. Bubble size (or bubble diameter) is taken to be the geometric mean of minor-axis (b) and major axis (a) lengths i.e. d = $\sqrt{ab}$. Similarly, eccentricity of bubble projected areas (hereafter referred to as 'bubble eccentricity') is defined as: $e = \sqrt{1-(b/a)^2}$, suggesting that a perfectly circular bubble has an eccentricity of zero. Figure 18(a) shows the PDF of all of the bubbles detected in the 1000 images taken of the reference case (blue bars) as well the range of the individual image PDFs (red bars). The bubble size distribution is bimodal, similar to the reports of Tse et al., with peaks at 0.30 mm and 0.62 mm. This suggests that the bubbly wake contains an excess of small-sized bubbles at the first mode (around 25-40%) which are significantly smaller than the Sauter mean diameter. The fraction of 0.62 mm bubbles is 8-16% of the total and the fraction of larger bubbles decreases with increase in size. There are very few bubbles with bubble diameter greater than 1.5 mm. Moreover, the range of individual image PDFs (red bars, 18a) do not change significantly when experimental conditions are varied. For this reason, the ranges in the PDFs are not shown in subsequent figures.

Figure 18b presents a three-dimensional histogram of fraction of bubbles with bubble diameter and eccentricity. As observed from the figure, about 25% of the bubbles are very small and have zero eccentricities (i.e. are spheres). Non-zero values of e can be observed only for bubbles larger than 0.5 mm. For instance, 8% of the bubbles are of size 0.6 mm with e = 0.6. It is worth mentioning here that tiny bubbles, below 180 μm in size, are assumed by the bubble detection algorithm to be always spherical. For bubbles of this size, it is difficult to estimate the eccentricity accurately since the bubble image occupies only a few pixels. However, images of these very small sized bubbles taken at a higher magnification/resolution has confirmed our assumption regarding sphericity of these bubbles. A variety of bubble shapes are found in the bubbly wake viz. spherical, ellipsoidal, and wobbling, highly elongated bubbles etc. The bubble shape and size distributions in the bubbly wake are determined by the occurrence of bubble deformation, breakup and coalescence processes in the wake. The variation in experimental parameters (water velocity, ventilation air flow rate, hydrofoil angle of attack) govern the occurrence of these processes. It is well known that the breakup processes in turbulent dispersions are influenced by continuous phase hydrodynamics whereas the contact and collision of bubbles determine the bubble coalescence process. The collision between bubbles is caused by their relative velocity and is affected by the bubble density in the flow.

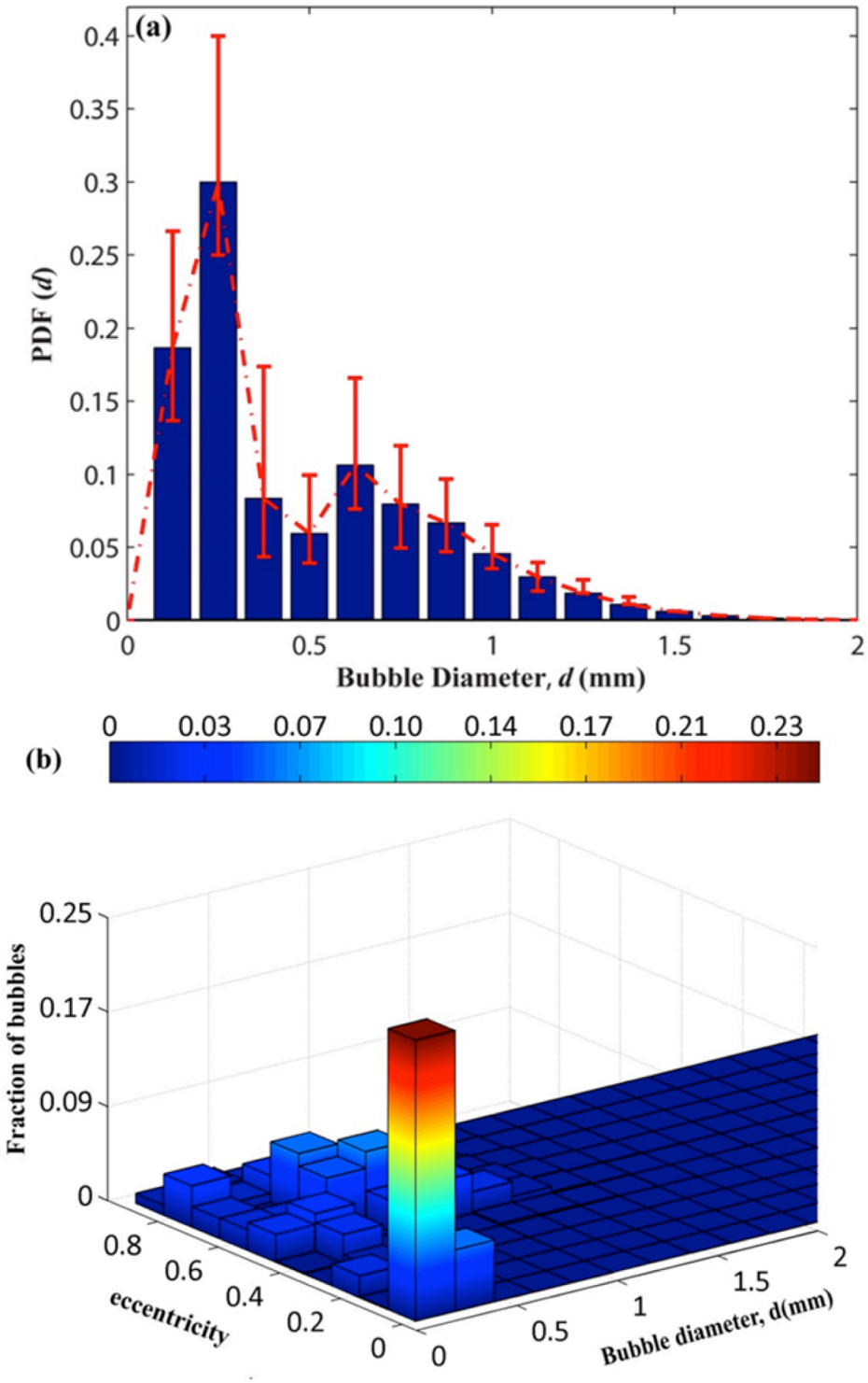

Figure 18: (a) Bubble size distribution for the reference case and (b) bubble shape distribution: fraction of bubbles as a function of eccentricity and size for the reference case. The red bars in (a) show the range between maximum and minimum values.

1.2. Void fraction measurements

Figure 19 shows a contour plot of the local void fraction in the bubbly wake for the reference case. For the calculation of local void fraction, the entire FOV is divided into a number of windows of size 0.94 mm x 0.94 mm (16 × 16 pixels). First, the projected areas of all the bubbles within each window are traced and the volume of all the bubbles is calculated assuming a third radius equal to the semi-minor axis of the projected ellipse. The ratio of the total volume of all the bubbles and volume of each window (the depth of each window determined by the depth of field) gives the local volume void fraction in the wake. As the figure shows, the local void fraction can reach as high as 0.15. The maximum local void fraction values occur below the centerline (i.e. y = 0). It should also be noted that the slot is located approximately 6 mm below the centerline and the void fraction distribution in the transverse direction is symmetrical about the elevation of injection slot. The figure shows that the void fraction decreases with distance from the injection slot elevation. The greater void fraction at the location of the injection slot is due to both a larger number of bubbles and greater size of bubbles at this location. A detailed description of these results is provided in a recent report by Karn et al (2015b).

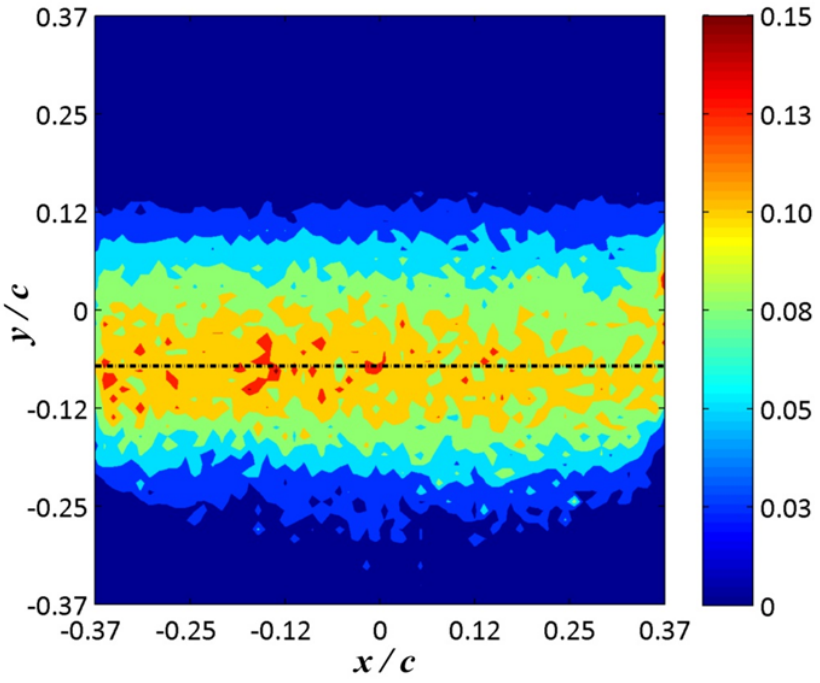

Figure 19: Local void fraction in the bubbly wake for the reference case. Origin (0,0) of the above plot is horizontally displaced 4.65c from the hydrofoil center of rotation. The horizontal line shows the elevation of the injection slot.

1.3. Bubble Velocity Measurements in the wake

The turbulence in the wake flow downstream of a hydrofoil affects both bubble size and velocity in the wake. The bubble velocity fluctuations, in turn affect the local liquid velocities. The bubble velocity measurements were made at three downstream locations, x/c = 1.34, 3 and 4.65

The PSV analysis of the bubbly wake images show that for the reference case, the wake related bubble velocity deficit was 6.7% of the free stream velocity at the location closest to the foil and decreased to 3.4% at the furthest downstream location (Karn et al 2015a). Figure 20 presents the normalized bubble velocity deficit profiles for the reference case with all 3 measurement locations included.

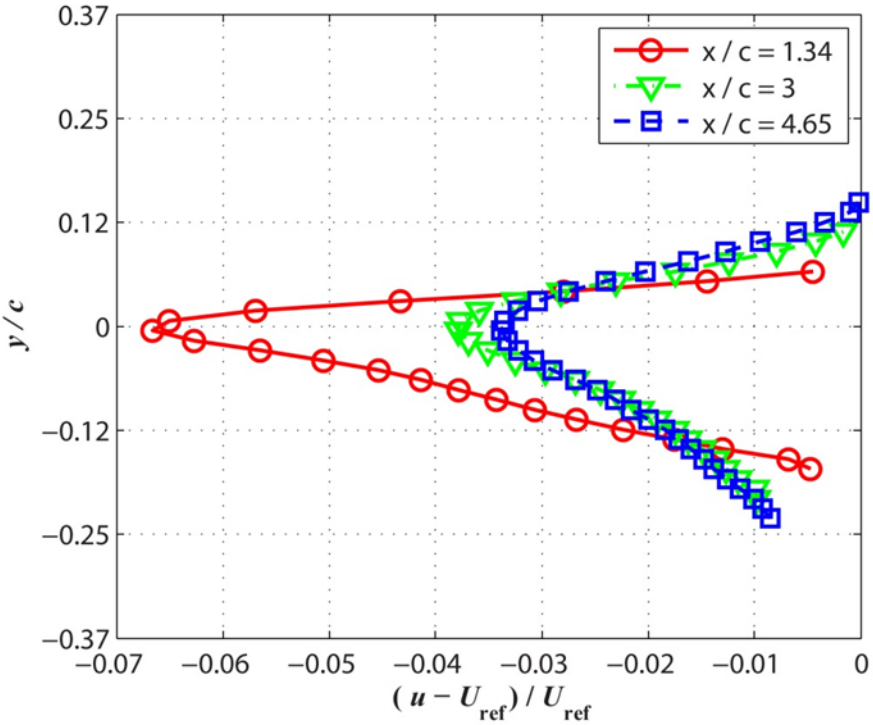

Figure 20: Averaged bubble velocity profile for the reference case at three different stream-wise locations. U_{ref} is the velocity at the edge of the wake at the measurement location. Uncertainty in velocity measurement at each data point is 5.2%.

1.4. Effect of variation in angle of attack of hydrofoil

. To investigate the effect of variation in AoA on the location of bubbles of a particular size, all the bubbles measured at a particular AoA (i.e. combining all 3 measurement locations) were sorted into six equal size bins spanning the bubble size range 0 to 3 mm. Figure 21 shows how the bubbles of difference sizes are vertically distributed in the wake for the three angles of attack.

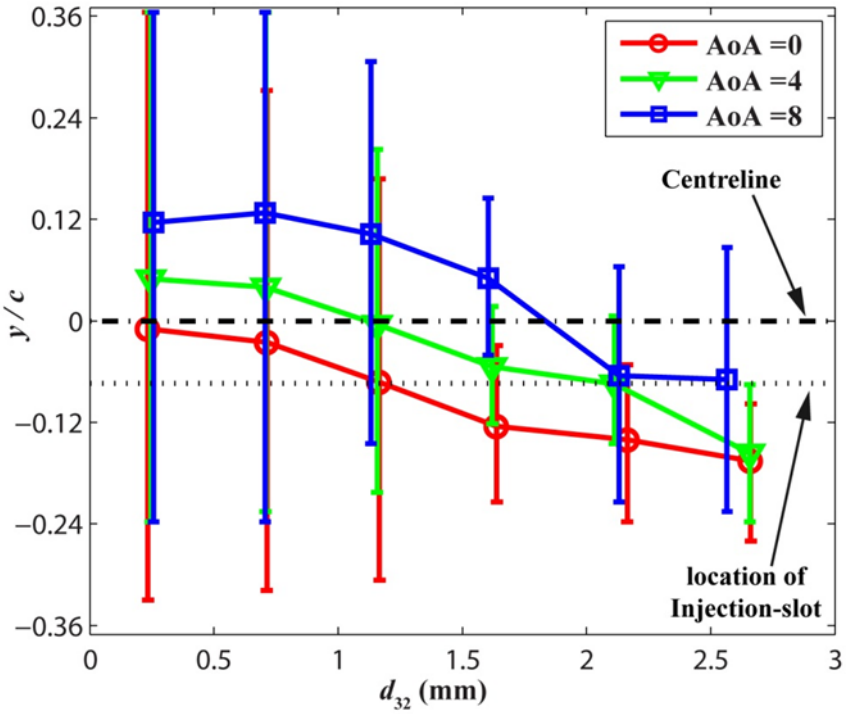

Figure 21: Spread of bubbles in the wake at different angles of attack. The symbols denote Sauter mean diameter and mean vertical location of all the bubbles in a size bin. The bars represent the vertical regions over which bubbles in each size bin are observed.

1.5. Effect of injection scheme

Two 2-D aerating hydrofoil configurations were tested in SAFL's high speed water tunnel. While these were both NACA 0015 hydrofoils, the location of the air injection slot was different. As described in previous sections of this report, the first hydrofoil tested (the "SAFL Foil") had its air injection slot located near the leading edge. The second hydrofoil tested (the "Alstom Foil") had its air injection slot centered on the trailing edge of the foil.

As described above, each hydrofoil was tested under 15 different conditions, varying angle of attack (0, 4, and 8 degrees), air flow (0.5, 1.0 and 1.5 SLPM), and water velocity (5, 7.5, and 10 m/s). At each of these conditions, the bubbly wake was shadow imaged, capturing double frames, with backlighting and a high-speed camera at 3 downstream locations: 109mm, 243mm and 377m from the center of the hydrofoil. Figure 22 shows images from the SAFL and Alstom foils, where images captured at different downstream distances have been shown on the same axis so that the relative distance of these measurement locations is apparent.

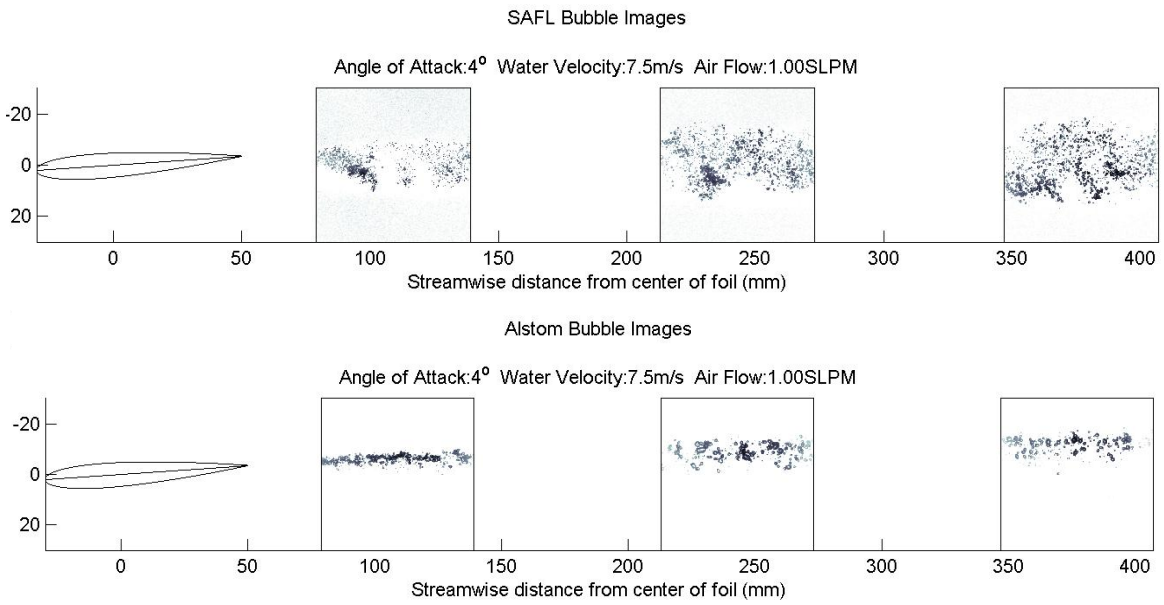

Figure 22: Example images of bubbles illuminated by a backlight. In both cases, the angle of attack of the hydrofoil was 4°, the water velocity was 7.5 m/s and the air flow rate was 1.0 SLPM.

In Figure 22, it is seen that the SAFL foil produces a bubbly wake which is much wider and comprised of generally smaller bubbles than the Alstom foil. Using the LaVision image analysis software package DaVis 7.2, particle shadow velocimetery (PSV) analysis was performed on all sets of double images taken by the high-speed camera. Each double image produced a velocity vector field based on the moving bubbles. It should be noted that all images had areas where there were no bubbles present as the bubble field varied both temporally and spatially. Where there were no bubbles, no velocity vectors were calculated. Averaging these 1000 velocity fields produced a single velocity field for each condition and location that was demonstrative of the bubble velocity field around the foil. A mean velocity vector was not computed for any location that had less than 100 valid vectors (10%) at that location throughout the 1000 vector field data set. This helped to eliminate extraneous data from the resultant mean vector field.

Figure 23 shows the streamwise bubble velocity field around the SAFL and Alstom foils at 4° angle of attack, 7.5m/s water velocity and a 1.0 SLPM air injection rate. As is also apparent in Figure 22, the SAFL foil disperses bubbles more widely in its wake, providing the PSV "seed" particles for the more widely characterized bubble velocity field. The Alstom foil bubbles are not as dispersed, resulting in a more narrowly characterized velocity field. The calculated velocities are only those associated with the bubble field in the wake and do not characterize the overall wake water velocities or extent.

As can be observed in the Figure 23 and the figures included in the Appendix, the SAFL foil appears to produce a wider bubble field in the imaged portion of the wake than the Alstom foil. This is not surprising given the location of the air injection. While the SAFL foil injects air near the leading edge of the foil, the Alstom foil injects air from the trailing edge, in the wake of the foil itself.

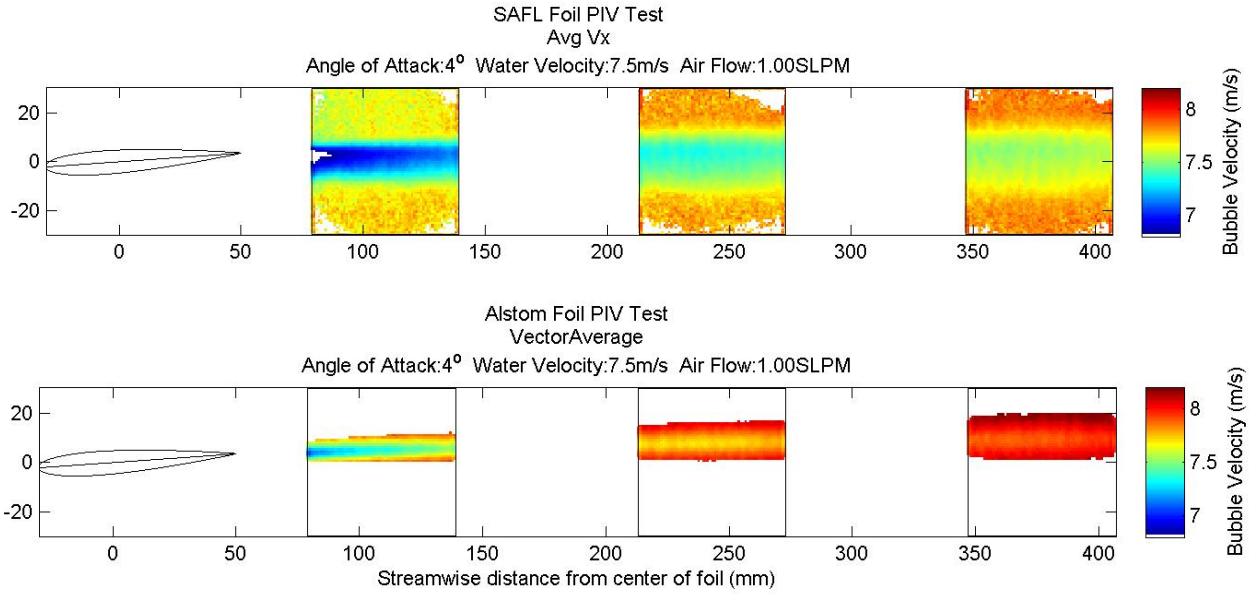

Figure 13: Mean streamwise bubble velocity fields for the SAFL and Alstom foils at 4° angle of attack, 7.5m/s water velocity and 1.0 SLPM air injection rate. Similar figures for all test conditions for each foil can be found in the Appendix of this document.

2. Bubble Size Distribution Results

Using the images of the bubbles, the bubble size distribution was determined using the image analysis technique described previously. The bubble size distribution has important implications for mass transfer.

2.1. Validation of Image Analysis Technique on Alstom Foil

As a metric of the bubble selection accuracy, the mass flow rate computed from bubble volumes derived from the images was compared to the mass flow controller setting for the test. For the Alstom foil, a small change was made to the method of computing the volumetric flow rate from the images. With the SAFL foil, the individual bubble velocity was determined using the velocity field for that particular image. For the Alstom foil, the velocity of each individual bubble was determined using the streamwise component of the unthresholded average velocity field for the test case. The unthresholded average velocity field is the velocity field that has not been filtered by removing a velocity measurement from a location if it does not have at least 100 valid velocity measurements at that location. For the reference case previously discussed (angle of attack = 0°, water velocity = 5 m/s, air flow rate = 0.5 SLPM), the results from the Alstom foil showed good agreement (Figure 24).

However, comparing the measured volumetric flow rates of other conditions generally did not compare as well (Figure 25). Bubble clustering was more pronounced for tests with higher ventilation air flow rates resulting in increasing disagreement between bubble integrated and actual air flux with increasing air flow. This suggests that the clustering of bubbles in these images reduced the ability of the image processing algorithm to identify all the bubbles. This lack of agreement is also more pronounced in the images that were taken at closer to the foil,

suggesting that bubble clustering again causes the bubble detection algorithm to miss bubbles. The dense clustering close to the foil is apparent in Figure 22.

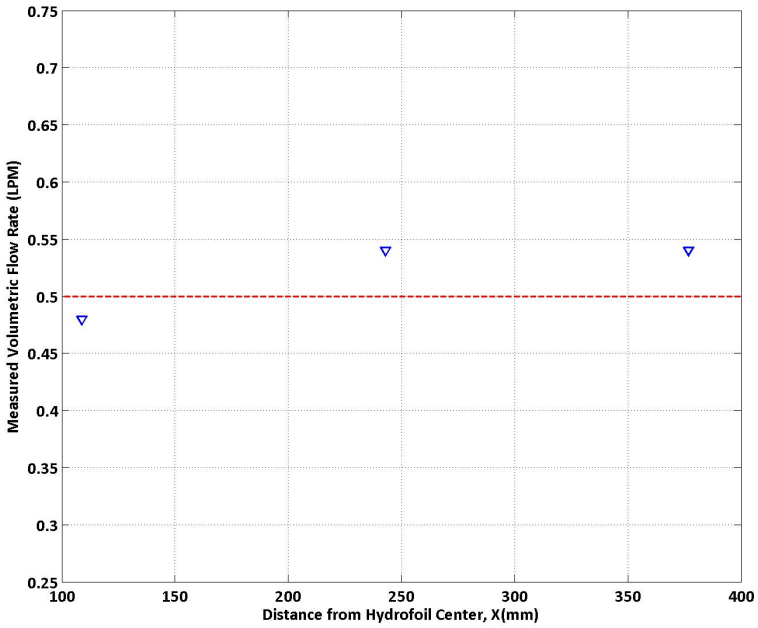

Figure 24: Alstom foil comparison of measured volumetric flow rate to the input flow rate of 0.5 SLPM at the reference case of 0^{o} angle of attack and 5 m/s water velocity.

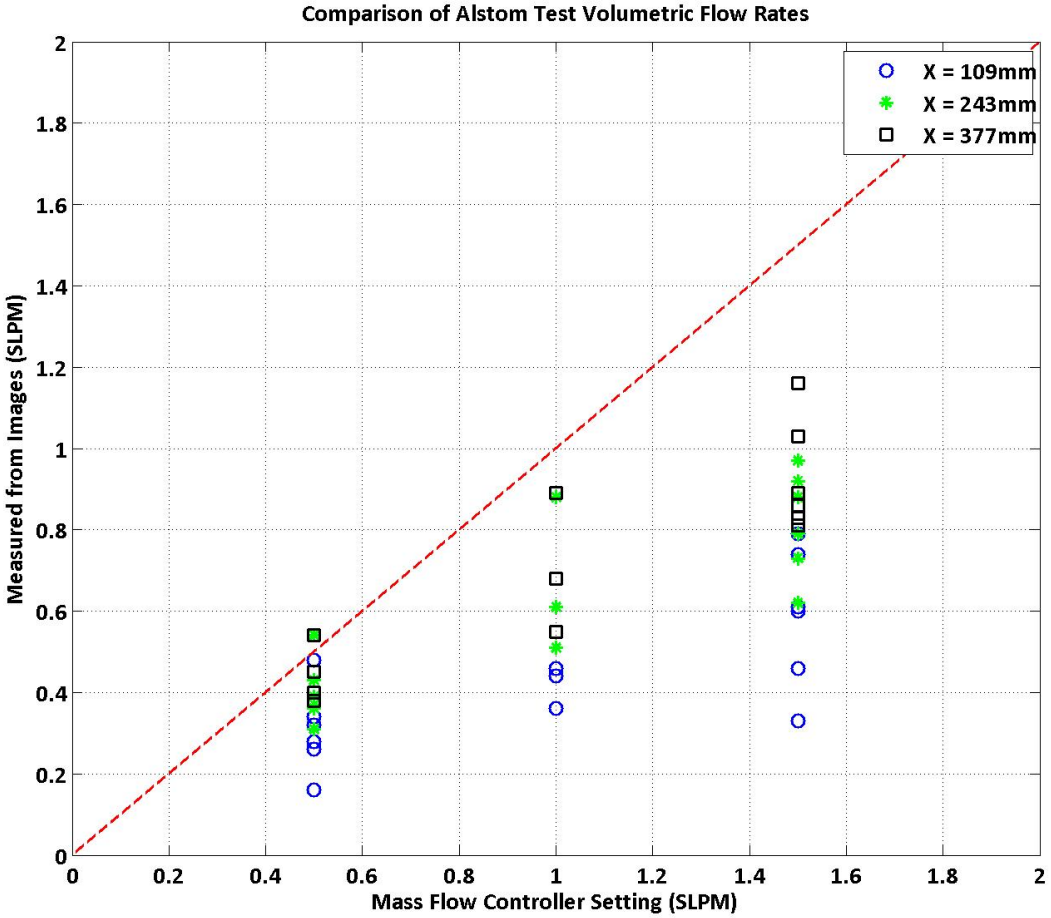

Figure 25: Comparison of Alstom measured volumetric flow rates to the input volumetric flow rate.

3. Bubble Size Comparisons

The Sauter mean diameter of the bubble population was computed for both the SAFL and Alstom foils for each of the 15 test conditions and for each of the three locations at these conditions. This resulted in 45 measurements of the Sauter mean diameter for each of the foils. Also, the bubble size distribution was plotted for each test condition. Initially, the data took the form of a probability density function (PDF) of bubble diameter. This method of plotting can be seen in Figure 26. However, it was decided that this way of analyzing the bubble size data misrepresents the gas transfer potential of the bubble population. A better understanding of the bubble size results, one that is more closely tied to the mechanics of gas transfer, can be accomplished be scaling the bubble diameter PDF by bubble surface area. Remembering that Sauter mean diameter (SMD) is defined as 6*bubble volume/bubble surface area, we scaled the number of bubbles of a certain size by their surface area/(total volume*6) to stay consistent with the SMD definition. See Figure 27. The integral (summation) of the bubble size PDF (histogram) scaled in this way equals the value of 1/SMD. Since it is shown below in section V.4.2 that the rate of gas transfer from a bubble population to the surrounding water scales as 1/SMD, we

believe scaling our bubble size data in this way most closely represents the associated gas transfer process. Examples of both plotting methods are shown below and the full set of plots is available in the Appendix.

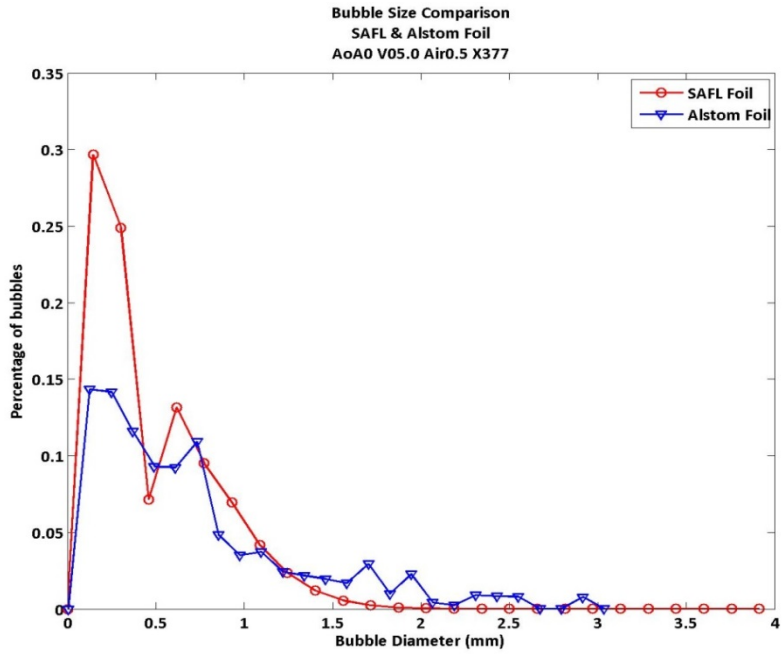

Figure 26: PDF of bubble diameter for both the SAFL and Alstom foils at the reference condition.

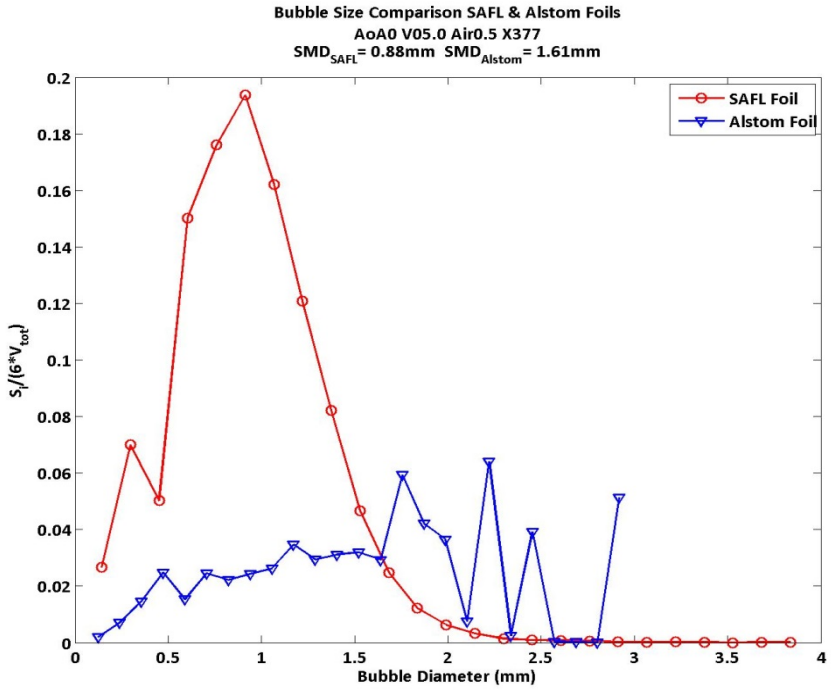

Figure 27: The bubble diameter PDF for the reference case, scaled by surface area/(total volume*6).

A summary of the Sauter mean diameters computed for all test conditions is shown in Figure 28. The average Sauter mean diameter of the SAFL foil was 0.8mm and the average Sauter mean diameter of the Alstom foil was 1.1mm. The histogram shows that both the SAFL and Alstom foils have a large number of conditions where the Sauter mean diameter of the bubble population is around 0.5mm. For the SAFL foil, the majority of conditions produced populations with a Sauter mean diameter in this range with a single condition producing an SMD greater than 1mm. The Alstom foil, on the other hand, produced bubble populations with Sauter mean diameters spread across a wider range and up to 1.8mm.

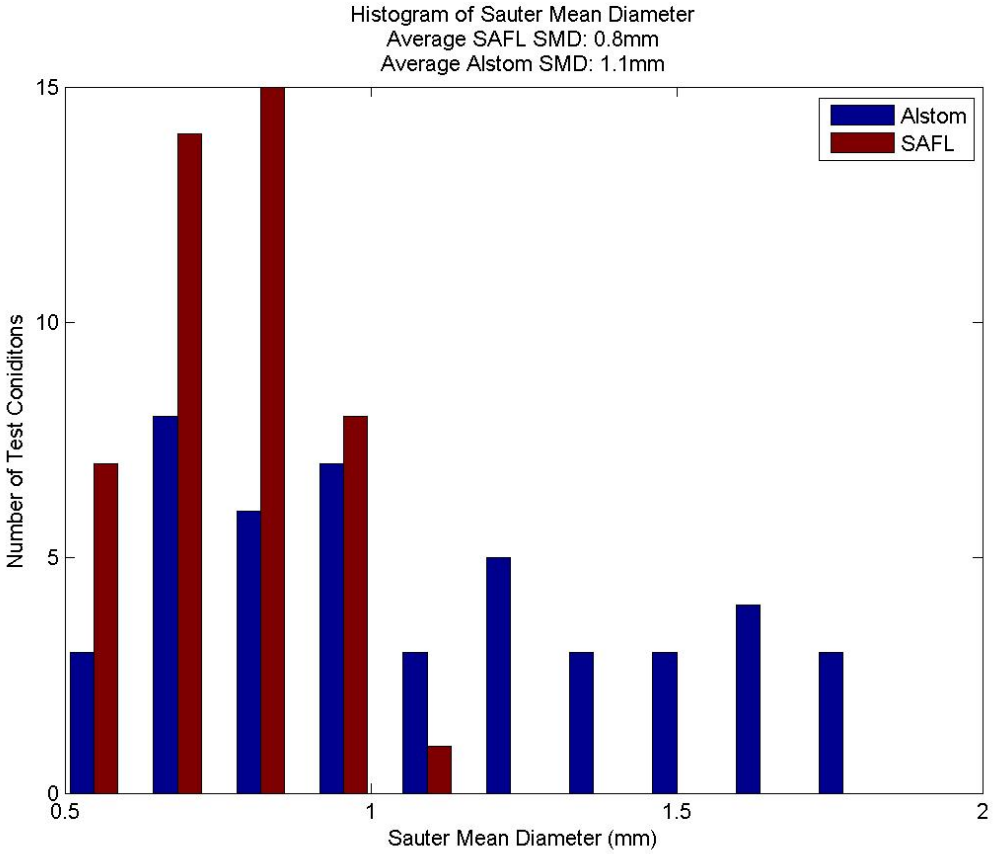

Figure 28: Histogram of computed Sauter mean diameter for the SAFL and Alstom foils.

In general, the Alstom foil produced bubble populations with SMDs equal to or greater than the SAFL foil for the same test condition. The larger bubbles produced by the Alstom foil were generally found to occur at low angles of attack and slow water velocities. Figures 29 and 30 show that the test conditions in which the Alstom foil SMDs were significantly larger than the SAFL foil SMDs occurred at 0^o angle of attack and at a water velocity of 5 m/s. Conversely, the bubble populations produced at 8^o angle of attack and water velocity of 10 m/s showed smaller differences between the two foil configurations. In general, the Alstom foil SMD equaled or exceeded that of the SAFL foil for the same test condition.

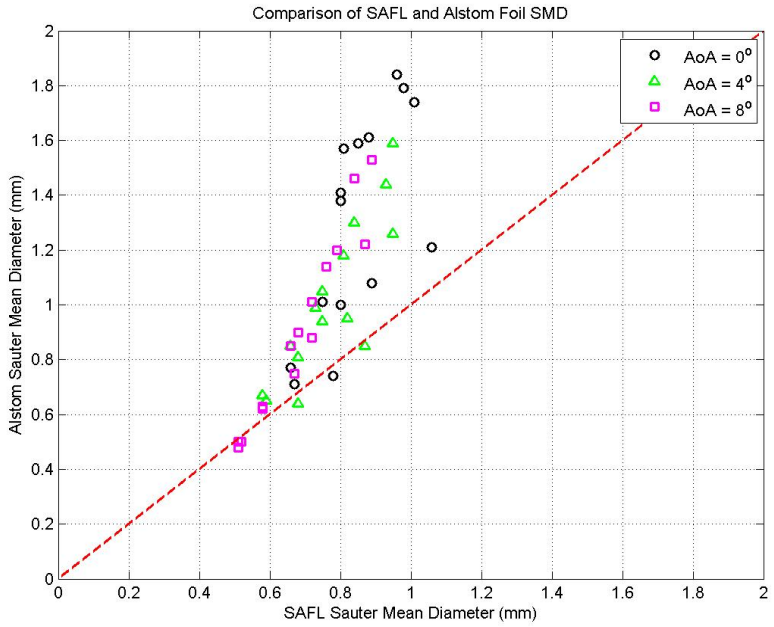

Figure 29. Comparison of the Sauter mean diameter of the bubble populations produced by the SAFL and Alstom foils. The colors of the markers represent the angle of attack of the foil. This plot illustrates the large difference between the SAFL and Alstom foil SMDs occurring in tests at 0^{o} angle of attack.

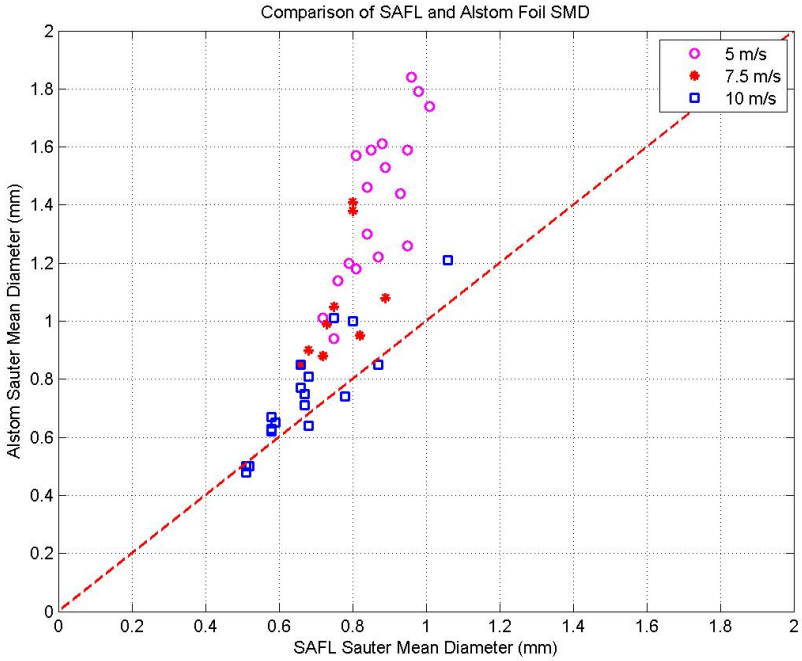

Figure 30. Comparison of the Sauter mean diameter of the bubble populations produced by the SAFL and Alstom foils. The colors of the markers represent the water velocity. This plot illustrates the large difference between the SAFL and Alstom foil SMDs occurring in tests at a water velocity of 5 m/s.

On the basis of these plots, it is conjectured that for the Alstom foil, which discharges air to the wake directly from the trailing edge, a non-zero angle of attack and higher water velocity tend to shear the bubbles down to smaller sizes. At 0^o angle of attack and 5m/s, the bubbles remain large because they are injected into the wake in the direction of the flow with minimal shear. For the SAFL foil, the bubbles experience significant shear at all velocities and angles of attack because they are injected orthogonally to the flow direction near the leading edge of the hydrofoil. This results in much less variation in bubble size and generally smaller bubbles for the SAFL foil compared to the Alstom foil.

4. Oxygen Transfer

4.1. Oxygen Transfer Coefficient

A one-dimensional model of the change in dissolved oxygen (DO) concentration in the tunnel was developed to fit the results of the physical experiments to a mass transfer theory using a single coefficient. The simplified conservation equation for the concentration of oxygen in a section of the tunnel is given by Equation (17):

$$\frac{dC}{dt} = U\ \frac{dC}{dx^*} = K_L a\ (C^* - C) \tag{17}$$

where C refers to DO concentration and C^* corresponds to equilibrium DO concentration in a particular section of the tunnel, x^* refers to a moving co-ordinate system given as $x^* = x - ut$, and $K_L a$ is the oxygen transfer coefficient, made up of the liquid film coefficient, K_L, and the specific surface area of bubbles, a, (or the surface area of bubbles divided by volume associated with those bubbles) given by Equation (18):

$$a = \frac{A_{St}}{V_w} \tag{18}$$

where A_{St} is the total surface area of the bubbles and V_w is the volume of water in which A_{St} is determined.

Non-linear regression software (Stenstrom et al. 1981) was used to estimate $K_L a$. Values of $K_L a$ were computed for all 15 tests for both the SAFL and Alstom foils from the DO concentration vs. time data. (See Figures 31 & 32.) These values were adjusted to 20 ^oC according to the equation (ASCE 2007):

$$K_L a_{20} = K_L a * 1.024^{(20-T)} \tag{19}$$

where T is the temperature of the water (^oC). The comparison of the $K_L a_{20}$ values of the 2 foils is shown in Figure 33. Further adjustment was made to compensate for the system pressure in the tunnel. While pressurizing the tunnel was unnecessary during the SAFL foil testing program, added system pressure was required for the Alstom foil tests which were run at 10 m/s and at non-zero angles of attack due to the presence of cavitation under these conditions. Unchecked, cavitation can be quite erosive and do extensive damage to both the foil and the tunnel. The fact that added system pressure affected the estimates of $K_L a$ is illustrated In Figure 33 by comparing the 2 test points labled AoA0_V10_Air3, one in bold, one not. These were for a repeated test

where one was pressurized and the other not. (For this condition, pressurization was not required but was specifically applied for one test to verify the effect on K_La.) The effect of tunnel pressurization can be seen. It is conjectured that the drop in K_La for the pressurized tests might be due to the bubbles being smaller, thus having less surface area for transfer, than those in the equivalent non-pressurized case. For this reason, the K_La values computed for the pressurized tests were further adjusted to compensate for the effect of pressurization by scaling the measure K_La values by the bubble surface area change due to pressurization which should in turn scale with the bubble volume change to the 2/3 power. The graph showing the Figure 33 data scaled in this way is shown in Figure 34.

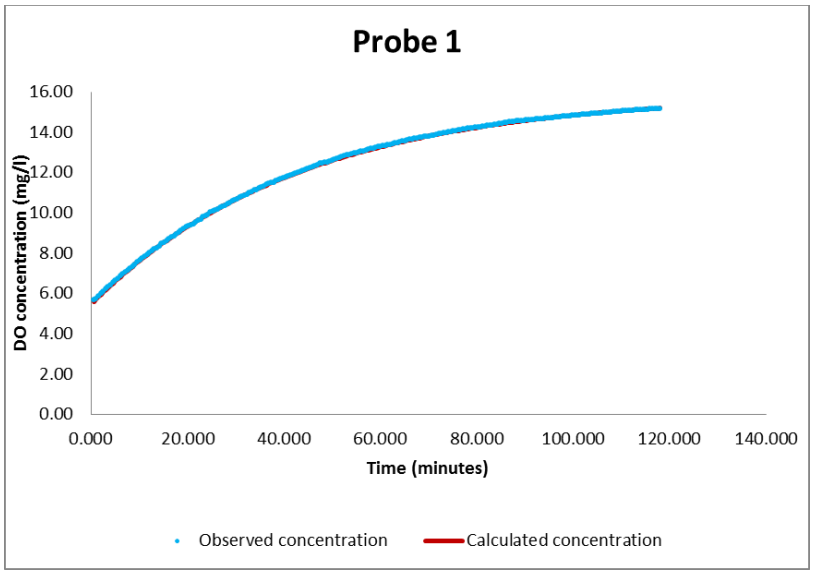

Figure 31. Typical DO time series data (AoA8, V7.5, Air20).

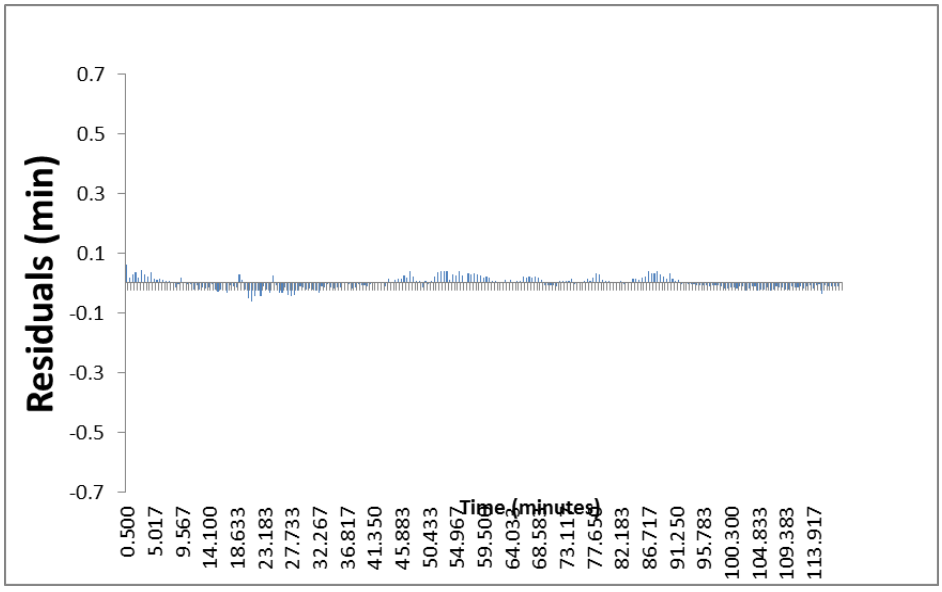

Figure 32. Residuals of best fit shown in Fig. 31.

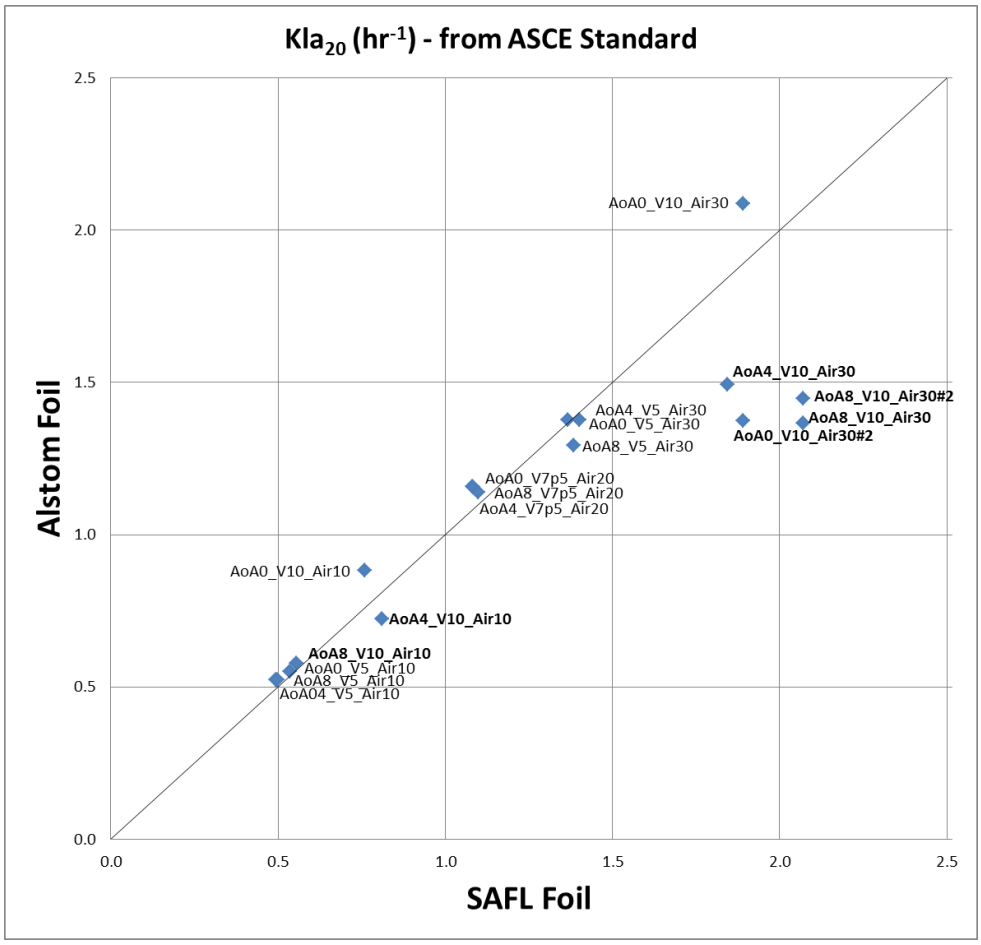

Figure 33. Comparison of SAFL and Alstom $K_L a_{20}$, adjusted to 20 degrees C, unadjusted for tunnel pressurization. Bold labels are tests conducted under pressurized conditions.

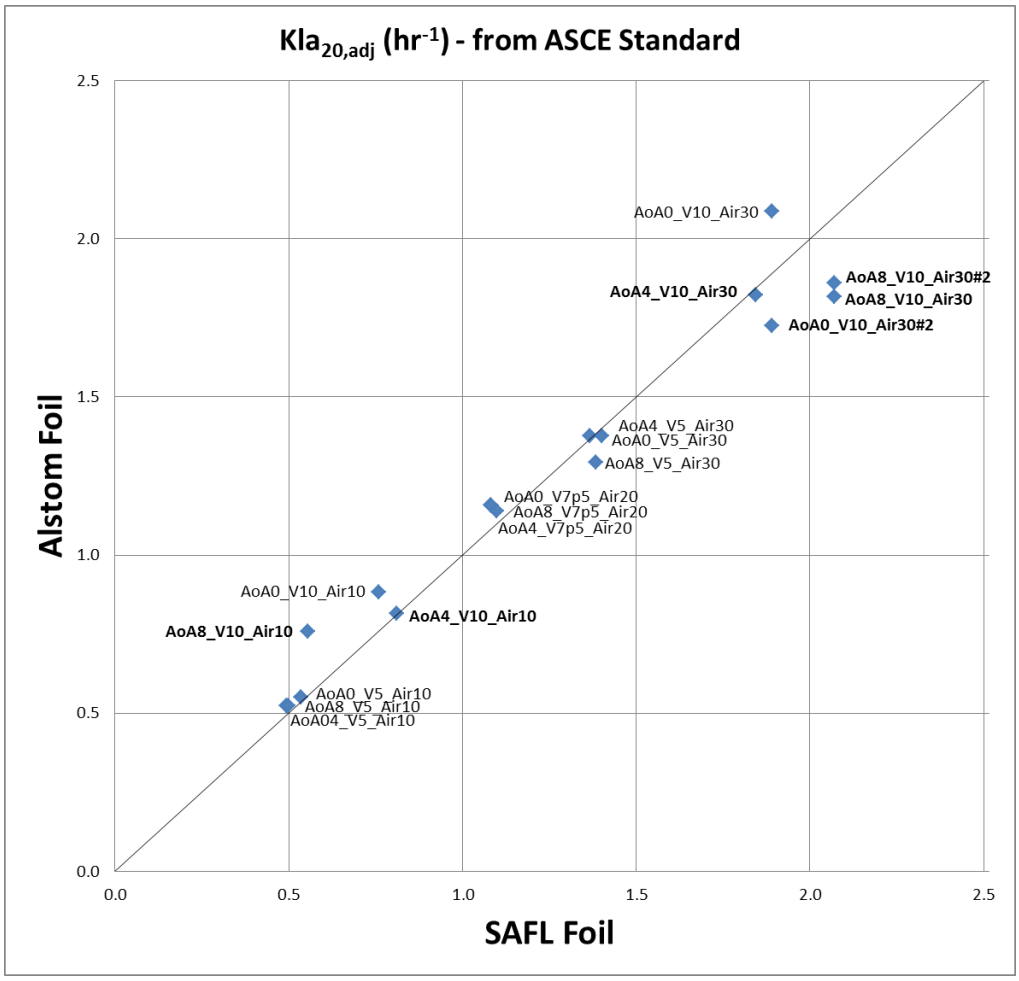

Figure 34. Comparison of SAFL and Alstom K_La_{20}, adjusted to 20 degrees C and for tunnel pressurization. Bold labels are tests conducted under pressurized conditions.

4.2. Oxygen Transfer Model

Bubble diameter is determined from from the shadow imaging experiments, and surface area weighted bubble diameter is defined as:

$$d_2 = \sqrt{\frac{A_{si}}{\pi N_{si}}} \tag{20}$$

where A_{si} and N_{si} are the bubble surface area and the number of bubbles from the shadow imaging experiments, respectively. Next, it is assumed that:

$$\frac{A_{si}}{N_{si}} = \frac{A_{st}}{N_t} \tag{21}$$

where N_t is the total number of bubbles corresponding to $A_{St.}$ Then, the combination of Equations (20) and (21) gives:

$$A_{St} = \pi d_2^2 N_t \tag{22}$$

The void fraction of air (φ) is given as:

$$\varphi = \frac{V_b}{V_w} = \frac{N_t \pi d_3^2}{6V_w} \tag{23}$$

where V_b is the total volume of bubbles in control volume V_w, and d_3 is the volume weighted bubble diameter determined from the shadow imaging experiments:

$$d_3 = \left(\frac{6V_{si}}{\pi N_{si}}\right)^{1/3} \tag{24}$$

where V_{si} is the total volume of bubbles from the shadow imaging experiments, and Equation (23) may be solved for N_t :

$$N_t = \frac{6\varphi V_w}{\pi d_3^3} \tag{25}$$

Equations (19), (22) and (25) may be combined to give:

$$a = 6\varphi \frac{d_2^2}{d_3^3} = \frac{6\varphi}{d_{32}} \tag{26}$$

where d_{32} is the Sauter mean diameter of the generated bubble population (Sauter 1926).

The equilibrium concentration C* is given by Henry's law and varies with temperature, pressure and solute content (Parkhill and Gulliver 1998; Daniil and Gulliver 1988). The mass transfer coefficient KL depends on the local air void fraction, the geometrical characteristics of the bubbles and local flow characteristics. Therefore, KL may be approximated by predictive relations Azbel 1981: Thompson and Gulliver 1997; Giovannettone and Gulliver 2008), but is best determined by controlled, flow-specific laboratory experiments. The theory of Azbel (1981) is employed to determine the liquid film coefficient in the model, KL,mod, as:

$$K_{\mathrm{L,mod}} = \beta \frac{D^{1/2}}{4\pi} \frac{u'^{3/4}}{(\nu_f l)^{1/4}} \frac{(1-\varphi)^{1/2}}{(1-\varphi^{5/3})^{1/4}} \tag{27}$$

Where, D is the water's diffusivity, ν_f is kinematic viscosity, l is a characteristic turbulence length scale, u' is a characteristic turbulent velocity, and β is a coefficient on the order of 1 to be determined by fitting with the experimental data.

The model partitions the water tunnel into six sections: test section, diffuser, right leg, bottom leg, left leg, and settling chamber. It requires inputs of test section velocity, test section pressure, average bubble diameter, airflow rate, water temperature, initial DO concentration, and DO system steady state or saturation concentration (referred to as 'saturation concentration' from now on).

A section's mean velocity is substituted for the characteristic turbulent velocity and the total bubble surface area is adjusted based on the change in bubble diameter caused by mass transfer and pressure changes using the ideal gas law. The model begins in the test section where it calculates KL,mod based on the inputs and tunnel geometry and an assumed value of β. A fourth-order Runge-Kutta method is employed to solve for the change in DO that result from the water's transit of the test section. The model then steps to the next section of the tunnel where it executes the same procedure using the DO concentration that leaves the previous tunnel section as the section's inlet concentration. This process is repeated for all remaining tunnel sections.

The bubbles will then leave the tunnel via the gas collector dome above the low velocity settling chamber. The loop is then repeated with the new concentration in the settling chamber as the inlet concentration to the test section, where air is venting through the hydrofoil. This process is repeated until a steady state concentration is reached. The time it takes for the water to complete one loop is known based on calculated section mean velocities throughout the water tunnel. This time is used to compare the calculated to measured DO concentrations where the LDO probes are located as a function of time.

4.3. Results of oxygen transfer model fit to experiments

The one-dimensional mass transfer model requires certain inputs such as liquid velocity, the test-section pressure (reference pressure) and temperature and the initial and steady state oxygen concentrations. The β coefficient and C^* at atmospheric pressure were adjusted in a curve-fit of the experimental data until the standard error of the fit to the measurements was minimized. Typical comparisons of the curve fit and the measurements are given in Figure 35, which also shows the impact of ventilation rate on gas transfer rate. The lower ventilation rate has a lower slope near time zero than the higher ventilation rate.

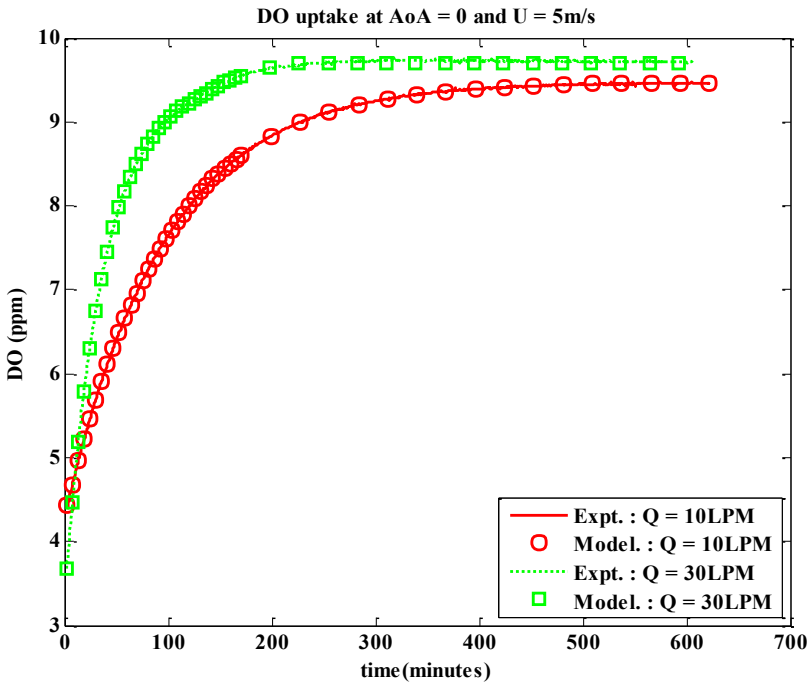

Figure 35: Typical fit of the DO model to measurements. Also shown is the effect of variation of ventilation rate on DO uptake at fixed AoA and water velocity

The experimental and model results are summarized in Tables 1 and 2 which show the variation of measured d_{32} and computed β and $K_L a$ across all test conditions for the SAFL foil and the Alstom foil, respectively. The following observations can be made from the tables:

1. The Sauter mean diameter decreased with an increase in water velocity at all angles of attack and all ventilation rates.
2. The Sauter mean diameter increased with an increase in ventilation rate for all angles of attack and water velocities.
3. The Sauter mean diameter for the Alstom Foil was generally higher than that of the SAFL foil under similar experimental conditions.
4. The Sauter mean diameter for the Alstom foil was close to that of the SAFL foil at the highest water velocity.
5. $K_L a$ increased with an increase in water velocity at all angles of attack and all ventilation rates.
6. $K_L a$ increased with an increase in ventilation rate for all angles of attack and water velocities.
7. There was no consistent trend in $K_L a$ with angle of attack.
8. In general, the $K_L a$ measurements for the two foils were relatively close to each other. This can also be seen in Figure 34.
9. The values of β for each angle of attack for the SAFL foil were relatively close with the exception of the value at 8 degrees AoA, 10 m/s water velocity and 10 SLPM ventilation rate.
10. The values of β for each angle of attack for the Alstom foil were more variable and greater than those of the SAFL foil.
11. The values of β increased with decreasing angle of attack for both foils.

12. The values of β for each angle of attack for the Alstom foil decreased with increasing velocity.

Table 1. Gas transfer results for the SAFL foil. d_{32} is obtained from bubble images. The β values are determined from a fit of the model to experiments.

AoA[+] (deg)	U (m/s)	Q (SLPM)	d_{32} (mm)	$K_L a$ (hr^{-1})	β
8	5	10	0.79	0.50	0.54
8	5	30	0.89	1.38	0.54
8	7.5	20	0.68	1.10	0.54
8	10	10	0.51	0.55	0.34
8	10	30	0.58	2.07	0.52
4	5	10	0.84	0.49	0.54
4	5	30	0.95	1.40	0.59
4	7.5	20	0.75	1.08	0.59
4	10	10	0.58	0.81	0.59
4	10	30	0.66	1.84	0.54
0	5	10	0.88	0.54	0.60
0	5	30	0.98	1.37	0.60
0	7.5	20	0.80	1.08	0.60
0	10	10	0.66	0.76	0.60
0	10	30	0.75	1.89	0.60

[+] AoA is the angle of attack

Table 2. Gas transfer results for the Alstom foil. d_{32} is obtained from bubble images. The β values are determined from a fit of the model to experiments. Rows in bold indicate tunnel pressurization.

AoA[+] (deg)	U (m/s)	Q (SLPM)	d_{32} (mm)	$K_L a$ (hr^{-1})	β
8	5	10	1.20	0.52	0.87
8	5	30	1.53	1.29	0.87
8	7.5	20	0.90	1.14	0.80
8	**10**	**10**	**0.50**	**0.58**	**0.75**
8	**10**	**30**	**0.63**	**1.37**	**0.75**
4	5	10	1.30	0.52	0.97
4	5	30	1.59	1.38	0.97
4	7.5	20	1.05	1.15	0.95
4	**10**	**10**	**0.67**	**0.72**	**0.87**
4	**10**	**30**	**0.85**	**1.49**	**0.87**
0	5	10	1.61	0.55	1.20
0	5	30	1.79	1.38	1.20
0	7.5	20	1.41	1.16	1.20
0	10	10	0.77	0.88	0.95
0	10	30	1.01	2.09	0.95

[+] AoA is the angle of attack

The 0.34 value of β seen at 8° angle of attack, 10 m/s water velocity and 10 SLPM ventilation rate for the SAFL foil (observation No. 9 above) seems to be the primary outlier in Tables 1 and 2. It is believed that this is the result of measurement error. The other values of β in Table 1 are consistently between 0.52 and 0.60. Since β was introduced to account for the substitution of the mean free stream water velocity for the characteristic turbulent velocity in Equation (27), its value is expected to be the ratio of these two velocities raised to the ¾ power. Thus, the ratio of turbulent to mean velocity (i.e. the turbulence intensity) is $\beta^{4/3}$. Turbulence intensities of 0.42-0.51 are realistic for the flow in the wake of a hydrofoil.

The measured values of β for the Alstom foil are all higher than for the SAFL foil (observation No. 10 above). There are two possible reasons for this:

1) The wake behind the Alstom foil was, in all cases, smaller than that behind the SAFL foil, as can be seen in the appendix. This would mean that exposure to the high velocity outside the wake would be greater for the bubbles of the Alstom foil than for the SAFL foil, resulting in a higher value of the fitted β.
2) The measurements of bubble size occurred only in the test section. It was assumed that this bubble size, with adjustments for pressure, would continue throughout the water tunnel without the coalescence of bubbles because a larger void ratio is normally required for coalescence (Azbel 1981). There is the possibility that coalescence of the bubbles could occur in the bottom horizontal leg of the tunnel, if bubbles rising to the top of the tunnel would result in a higher local void ratio that would not be mixed vertically by

turbulence. Figure 34 provides some support for this theory, because the two foils tend to give similar K_La values for a given experimental condition except at high K_La values, which may indicate that the water tunnel instead of the foil is the primary determinate of K_La and bubble size. A counter to this hypothesis is that the values of β vary with the angle of attack, which would not be the case if the tunnel, instead of the foil, were the primary determinate of bubble size.

The fact that the values of β for each angle of attack for the Alstom foil tended to decrease as the water velocity increased (observation No. 12, above) may be due to the challenges of measuring bubble size distribution in the smaller wake behind the Alstom foil, particularly close to the foil, at low water velocities and at high air flow rates. Figure 25 indicates that the total bubble volume derived from the Alstom foil images was less than that of the mass flow controller setting, indicating that there was substantial shadowing of smaller bubbles. The shadowing of smaller bubbles would result in a larger computed Sauter mean diameter than actually exists, and would result in a larger fitted value of β. This shadowing tendency was reduced at the larger approach velocities, and may not have had a substantial impact on Sauter mean diameter, for which the larger diameters in the flow field are most important.

Historically, the β coefficient has been difficult to determine, because all of the required parameters have not been available. Specifically, the bubble surface area and bulk coefficients needed for the analysis have often been unavailable, resulting is a greater empiricism in the results (Thompson and Gulliver 1997: Geldert, et al. 1998; DeMoyer, et al. 2003; Wilhelms et al. 2005; Schierholz, et al. 2006; Urban et al. 2008; Giovannettone and Gulliver 2008; Witt and Gulliver 2012). Determining a β value in the range of 0.52-0.60 for different hydrofoil angles of attack, and the fact that it generally stays constant over a range of water velocities and airflow rates (for the SAFL foil at least), is believed to be a verification of Azbel's (1981) theory. We believe, using the coefficients found in this study, that this theory can be applied to other high-velocity turbulent-wake bubbly flows. The variation in β for the Alstom foil at various angles of attack is believed to have been caused by challenges in determining Sauter mean diameter for the relatively compressed wake produced by the Alstom foil.

5. Results and Discussion of Numerical Simulations

Aimed at validating our developed in-house computational code, several test cases were carried out. In this section we present the most important test cases and the results.

5.1. Laminar single phase flow test case

The first step in validating the developed code was to validate the coupling between liquid phase momentum and the liquid mass balance equations. This was a significant step, since the pressure field and liquid velocity field are the unknowns in the single phase flow. As mentioned earlier the fractional step method is employed to integrate in time the equations. To run our code for single phase flow it suffices to set the gas void fraction everywhere as zero. As a result the gas mass and momentum equation should be satisfied to machine zero with the trivial solution of zero everywhere. The test case we considered for this section was the standard cavity flow for Re =1000. Although this is a laminar problem at low Reynolds number, it serves as an excellent test

case to validate the base liquid phase coupling routines. The streamlines for some selected time steps superimposed on the velocity magnitude contours are plotted in Figure 36.

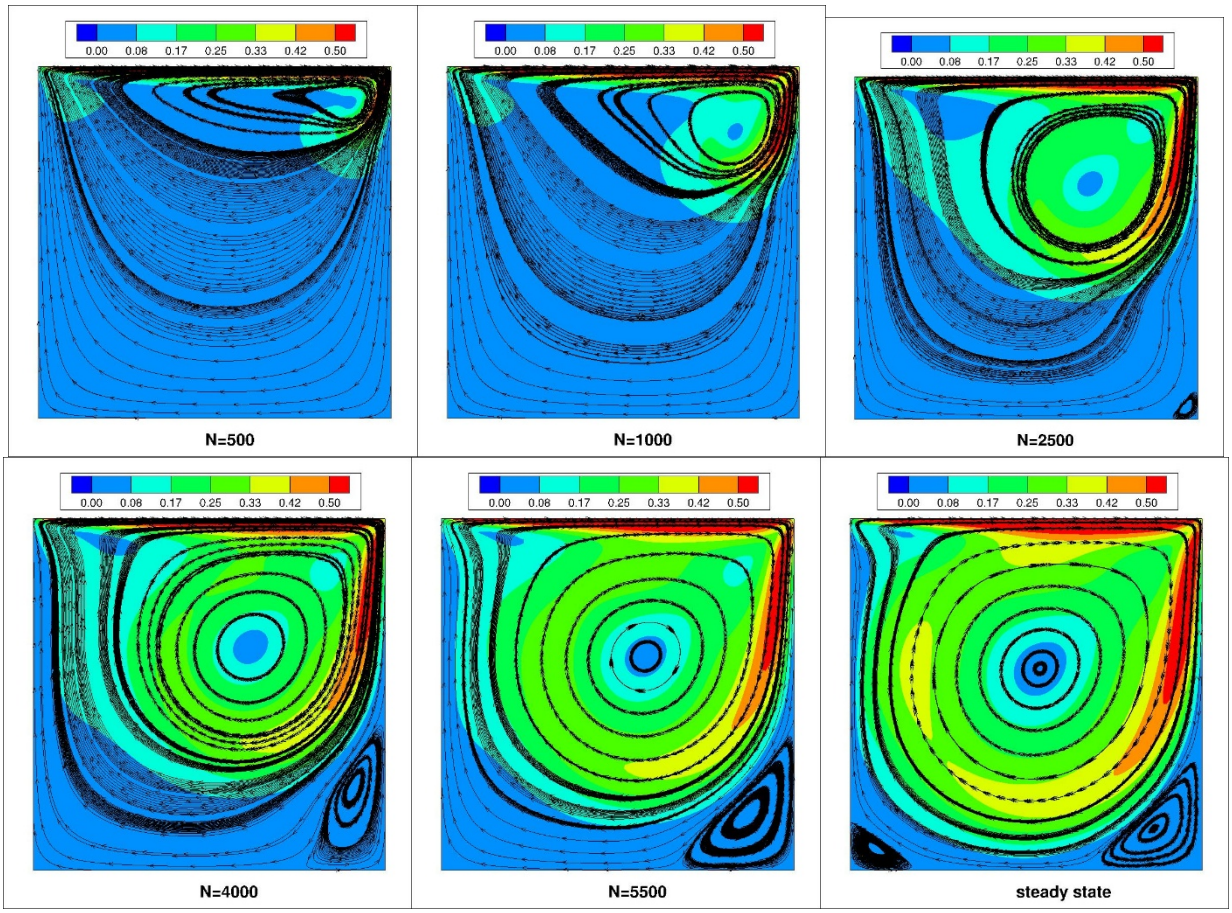

Figure 36. Streamlines superimposed on velocity magnitude

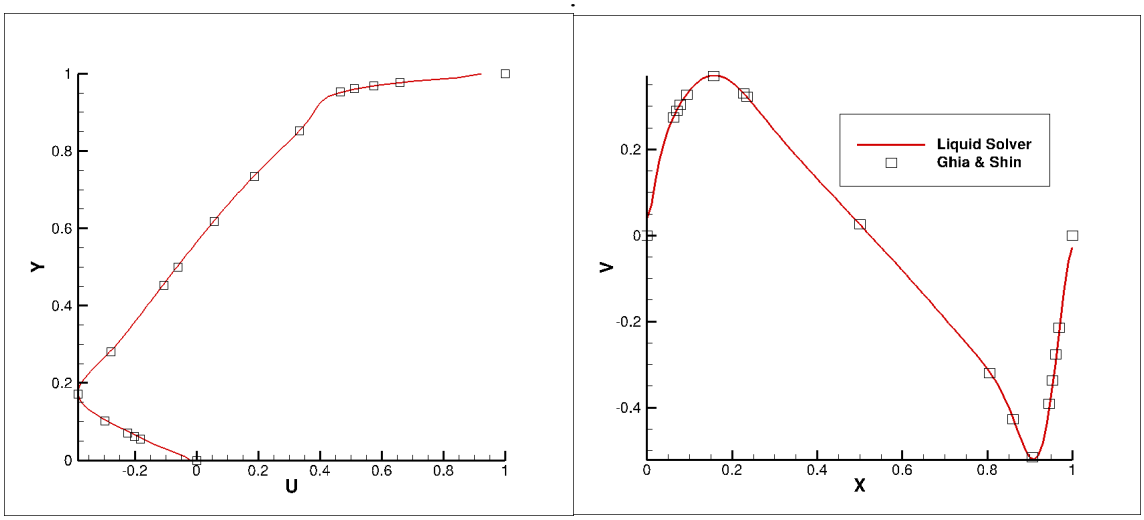

Figure 37: Comparison of the results from our code to the reported results by Ghia& shen for laminar lid driven cavity flow at Re = 1000

The results captured correctly and in a time-accurate manner. To quantitatively assess the results, the solution of the steady state at the horizontal and vertical middle planes are compared to the results of Ghia & Shen (1982), which is shown in Figure 37Figure 37 shows the correct implementation of the fractional step method for laminar flows.

5.2. Coupling of the gas void fraction solver with liquid phase solver for laminar flows

The next step is to validate coupling gas mass balance equation solution to that of the liquid phase solution. This requires solution of 3 equations out of 4 possible PDEs. To perform this test case, we have considered a patch of bubble in circular shape located in the same cavity as previous section (laminar with Re = 1000). The bubble patch is forced to move with a pre-specified velocity in the upward direction and allowed to exit the domain (outflow boundary condition) while the liquid boundary condition is identical to the previous section. This test case allows us to qualitatively observe the effect of bubble plume rising in a cavity, as the top lid is also moving. Also we expect the liquid phase solution converges to the steady state cavity flow after the bubble plume exits the domain. This proves that the coupling is implemented correctly and there is not leakage of error from the void fraction solver to the liquid phase solver, or vice versa. The streamlines, superimposed on the bubble patch position, are displayed for some representative time steps in Figure 38.

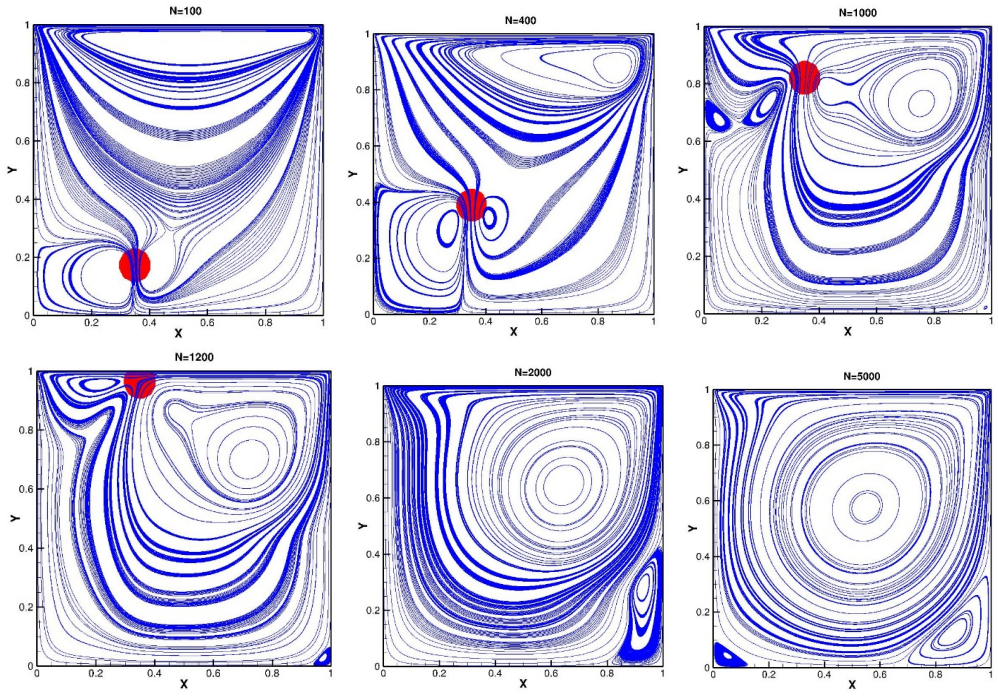

Figure 38: transient solution of rising bubble plume in a lid driven cavity problem for Re = 1000. (N denotes the number of time steps)

The solution shows that the numerical schemes we have employed could conserve the sharp gradients of the bubble patch area, with least smearing of the interface. This is primarily due to use of a proper flux limiter for the advective term. Also the boundary conditions are seen to be implemented correctly, as the bubble plume is exiting domain at N = 1200. Again, to assess the convergence to steady state results, the results at the steady state on the horizontal middle line are plotted in Figure 39 and compared with the numerical results of Ghia & Shen.

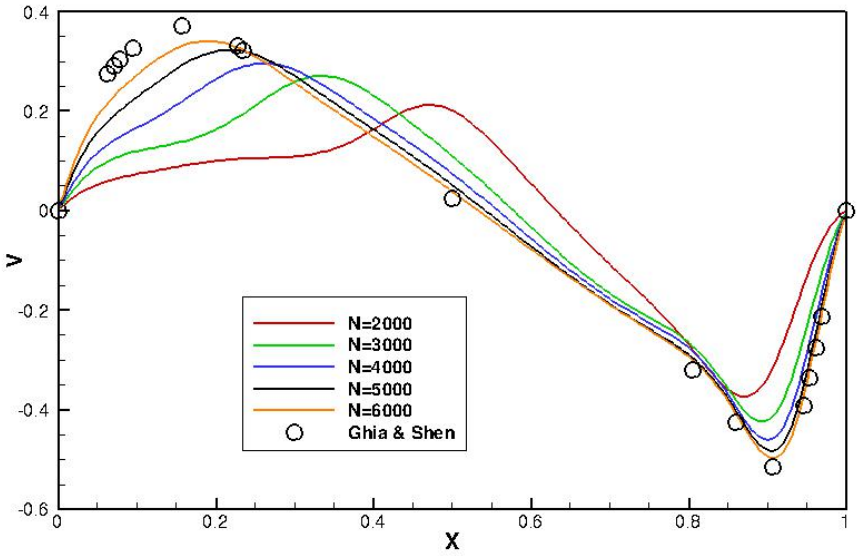

Figure 39: Vertical component of velocity on the horizontal middle line (y = 0.5)

Figure 39 shows the convergence of solution to the steady state results of Ghia & Shen. It is worth noting that the time to reach the steady state is longer in this case compared to the case without bubble plume, as expected. So, the conclusion is that the coupling of the void fraction with liquid phase is performed properly and in a bug-free manner.

5.3. Fully coupled solver for turbulent dilute bubbly flow

The benchmark test case of Deen's bubble column is considered to validate coupling of all main 4 Equations (30) – (33). In addition we have employed the Germano model to model the turbulence. This test case is turbulent bubble jet released from a bubble column for which time-averaged experimental data is provided in the literature by Deen (2000). The schematics of the problem is shown in Figure 40.

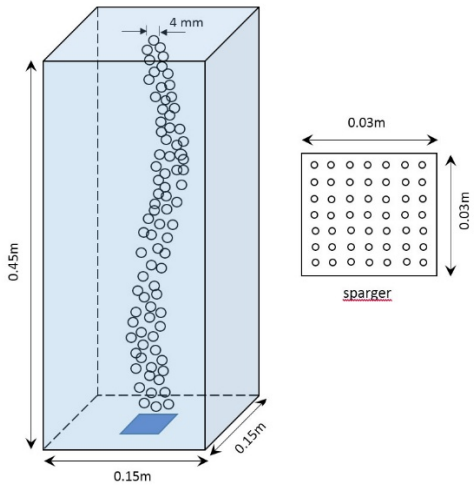

Figure 40. Schematic of the bubble column test case

The test case is a benchmark problem in the two phase bubbly flow field which has been studied numerically by many researchers to validate different numerical methods. The bubble column has a height of H = 0.45m with square cross section of W×D = 0.15×0.15m^2. Air is introduced into the bubble column through a W×D = 3×3cm^2 sparger at the bottom. The sparger has a 7×7 holes of 1mm diameter which is positioned at the center of the cross section at the bottom of the bubble column. 4grams of kitchen salt was added to prevent the bubble coalescence/breakup process. A 31x31x101 grid is employed for the simulation. This grid satisfies the grid resolution set by Mileli (2001). The superficial gas velocity of $u_s = 4.9\text{x}10^{-3}$ m/s is imposed at the bottom plane which corresponds to the gas jet velocity of $u_g = 2.806$ m/s from the sparger with the void fraction of $\alpha_G = 0.0427$. A constant time step size of Δt=0.001 which corresponds to CFL number of 0.5 is used for all time steps. The simulation was run until the flow reaches statistically stationary turbulence. Then after, time averaging was initiated and continued for another 250 seconds of physical time.

Figure 41 shows the instantaneous gas axial velocity contours superimposed on the liquid velocity vectors. Large and small vortices in the liquid phase are detectable moving through the bubble column while interacting with each other.

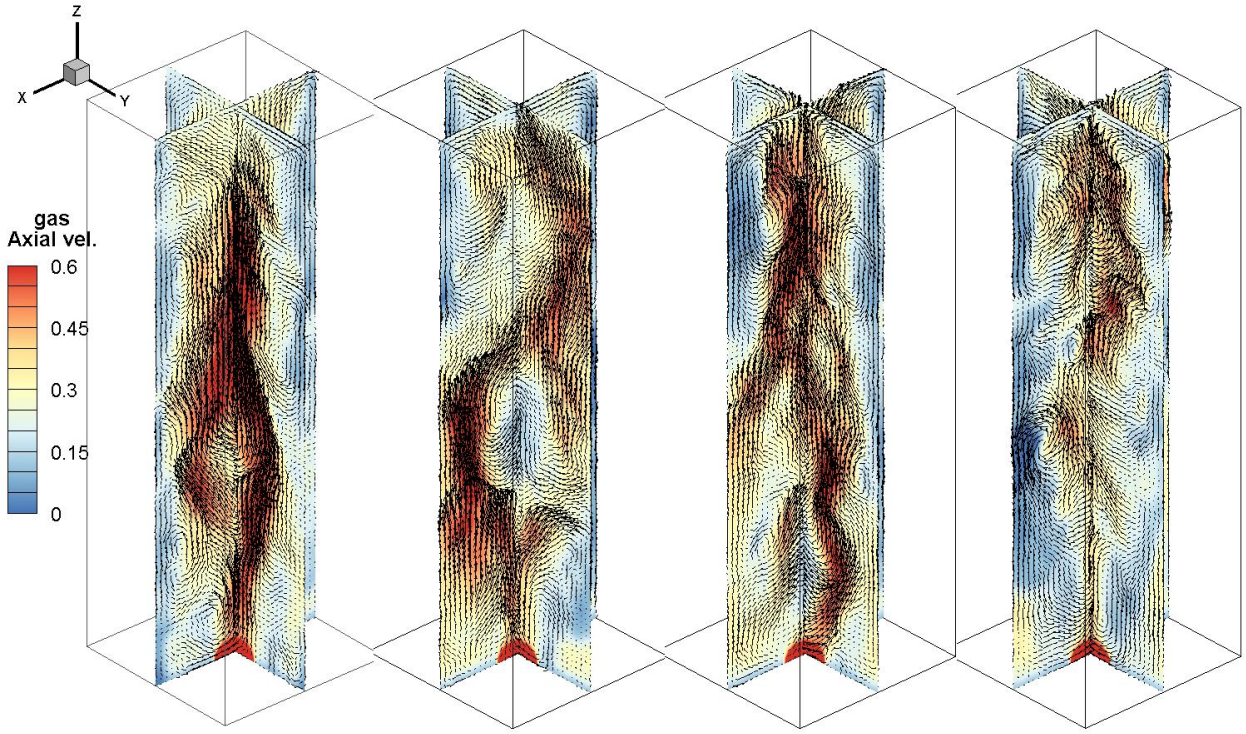

Figure 41. Instantaneous axial gas velocity contours superimposed on the liquid phase velocity vector on two middle planes

The time history of axial velocity component for the liquid phase for the point located at center of cross section (x = y = 0.075m) at height z = 0.25m, is plotted in Figure 42. For the purpose of comparison, the time history of the RANS approach ($k-\epsilon$) from the work of Deen et. al. and experimental data of Deen et. al (2000) are plotted on the same graph. The LES results indicate the chaotic velocity fluctuations in the bubble column and the strong coupling between the velocity fluctuations for both phases. It is clear from Figure 42 that, compared to RANS model,

the present LES captured the correct time history of velocity in terms of velocity amplitude and frequency. The $k-\epsilon$ model could only capture the large scale fluctuations while embedding small-scale fluctuations in *k,* while the present LES could resolve more scales of velocity profile, hence, capturing more physical velocity fluctuations.

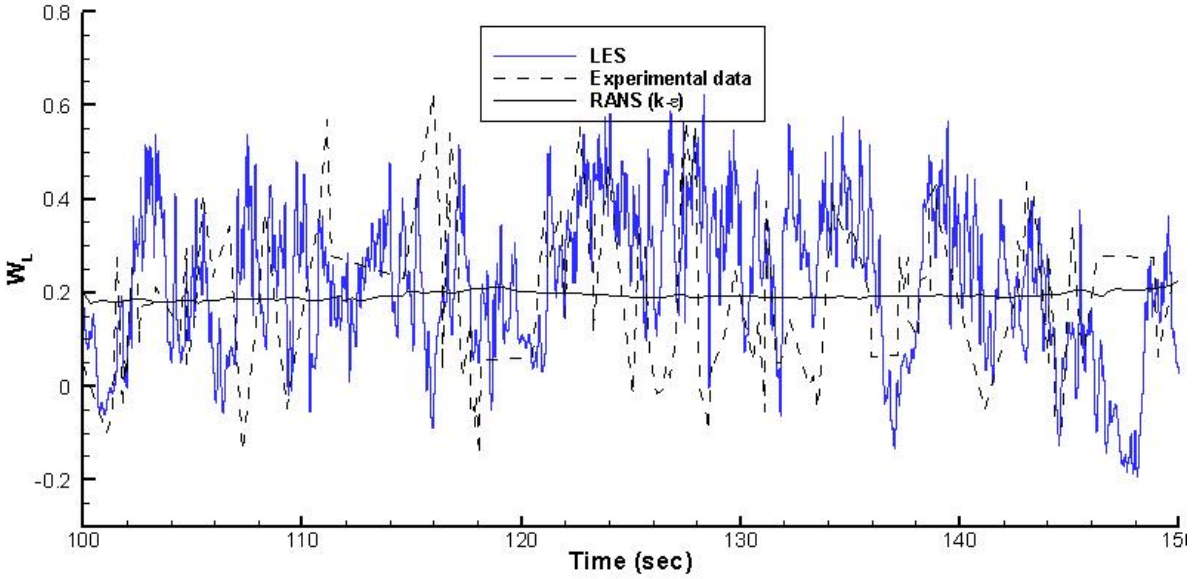

Figure 42: Time history of gas axial velocity and comparison with experimental data and RANS model

To validate the results of our mathematical formulation the time-averaged results are plotted in Figure 43 and compared with those of experimental data, which are plotted in Figure 44.

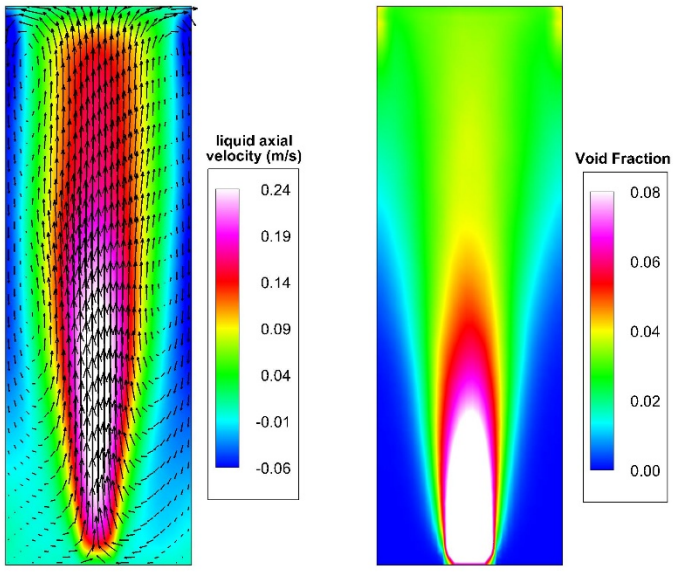

Figure 43. Time-averaged results for 250 seconds of physical time on the middle plane x = 0.075m. Left : time-averaged liquid axial velocity contours superimposed on the velocity vectors; Right : contours of time-averaged void fraction

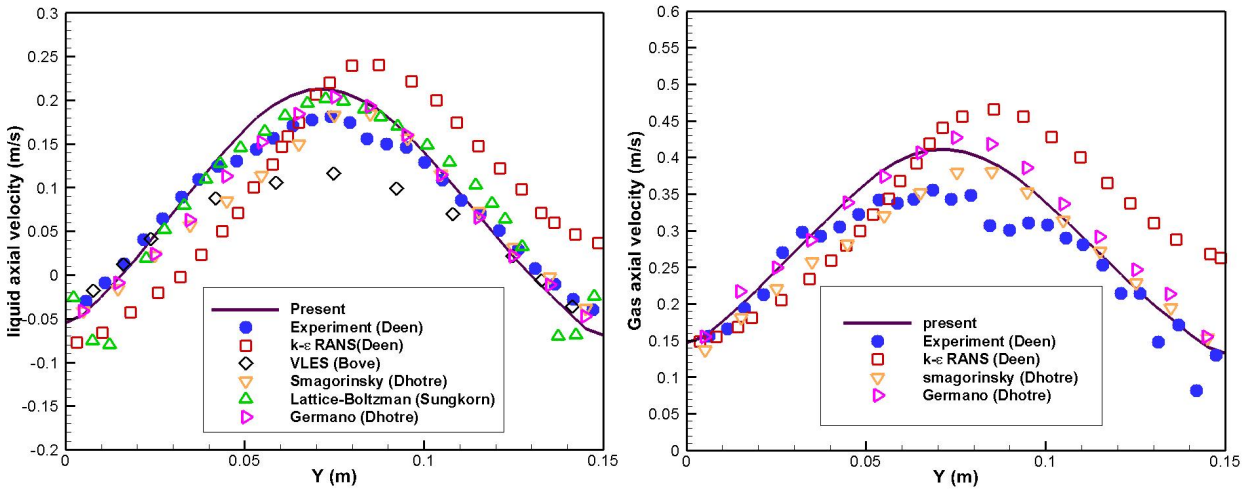

Figure 44. Comparison of the gas and liquid axial velocity component on the middle plane x = 0.075m at the height z = 0.25m with experimental data of Deen and other reported results in the literature

Figure 44 shows an excellent agreement between our computed results with experimental data. To study the second order statistics of turbulence quantities, the Reynolds stresses $\langle u'u' \rangle$, $\langle v'v' \rangle$, $\langle w'w' \rangle$ and $\langle v'w' \rangle$ of the liquid phase on the mid plane x = 0.075m are shown in Figure 45. Here, the $\langle\rangle$ denotes the time-averaging operation and u', v' and w' represent the fluctuating components in x, y and z directions, respectively. As expected, the contours are about symmetric around the centerline y = 0.075m. The axial Reynolds stress $\langle w'w' \rangle$ is about 3 times larger than the other stresses, which is an indication of anisotropic turbulence. The lateral and horizontal stresses $\langle u'u' \rangle$ and $\langle v'v' \rangle$ show the stresses to have a locally large quantity near the injection point of bubble. The stresses show a gradual increase from the release point of bubbles to the center of column, and decays gradually until the top of the bubble column. $\langle w'w' \rangle$ shows a similar behavior with a double peaked structure at the center. The highest axial turbulence stress does not occur in on the centerline, but slightly away from the centerline. Due to the boundary condition of free slip at the top, the $\langle w'w' \rangle$ gradually decreases from the center to reach its lowest quantity on the top surface. The shear stress $\langle v'w' \rangle$ shows an increasing trend from the injection point to center of column with an increasing angle, i.e. with an expanding width of the structure.

Our simulation results showed an excellent agreement with experimental data for both 1st order and 2nd order statistics of turbulence, in terms of velocities, RMS quantities and TKE. Overall, in addition to the ease in numerical convergence of solution, the proposed mathematical formulation demonstrated powerful approach in simulation of turbulent bubbly flows.

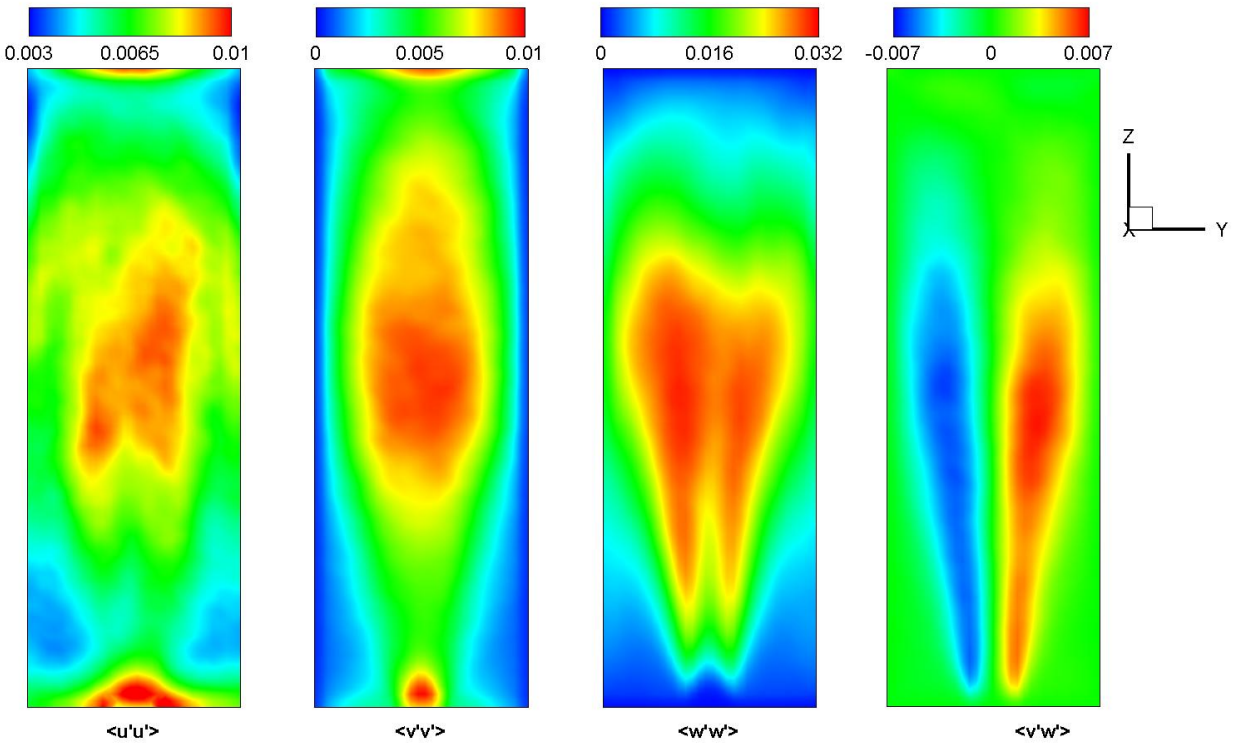

Figure 45. The Reynolds stresses on the middle plane (x = 0.075m)

5.4. Flow around airfoils

The next phase of the project was to enhance the code to be able to simulate flow around airfoils. The difficulty of flow around airfoils is the type of the grid to be used, if the body fitted type of grid is to be used. Either "C" or "O" or "H" type of grid should be employed for this problem. This needs further modification of the code. So the code should have been advanced one step further for the special case of airfoil flows. The advancement of the code is required due to presence of the virtual boundary created at the "wake cut". This consideration necessitates the fundamental change in all of the equations. Also special attention should be paid for the message passing between CPUs since they have to send information back and forth across the "wake cut". In our work, we implemented the "C" grid type. A typical "C" grid type from our work is shown in Figure 46. We ran the code for two test cases of single phase flow. Laminar flow and turbulent flow.

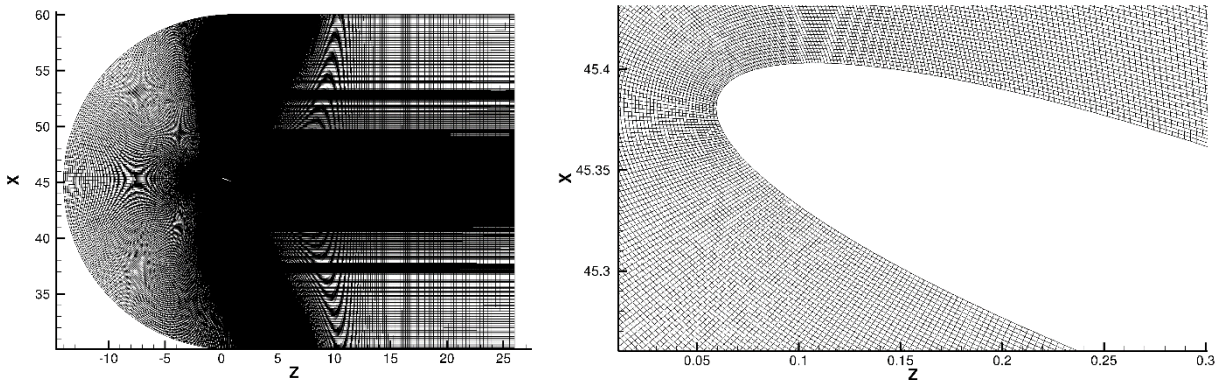

Figure 46. The body-fitted "C" grid type used to discretize the computational domain Left: The whole computational domain, Right: near the airfoil surface

For the laminar case, we considered NACA0012 with AoA =20°. We ran the case for different Reynolds numbers of Re = 5, 50, 800, 1000, 1600, 3000, 4000. The pressure and vorticity fields for Re = 5, 50 are shown in Figure 47.

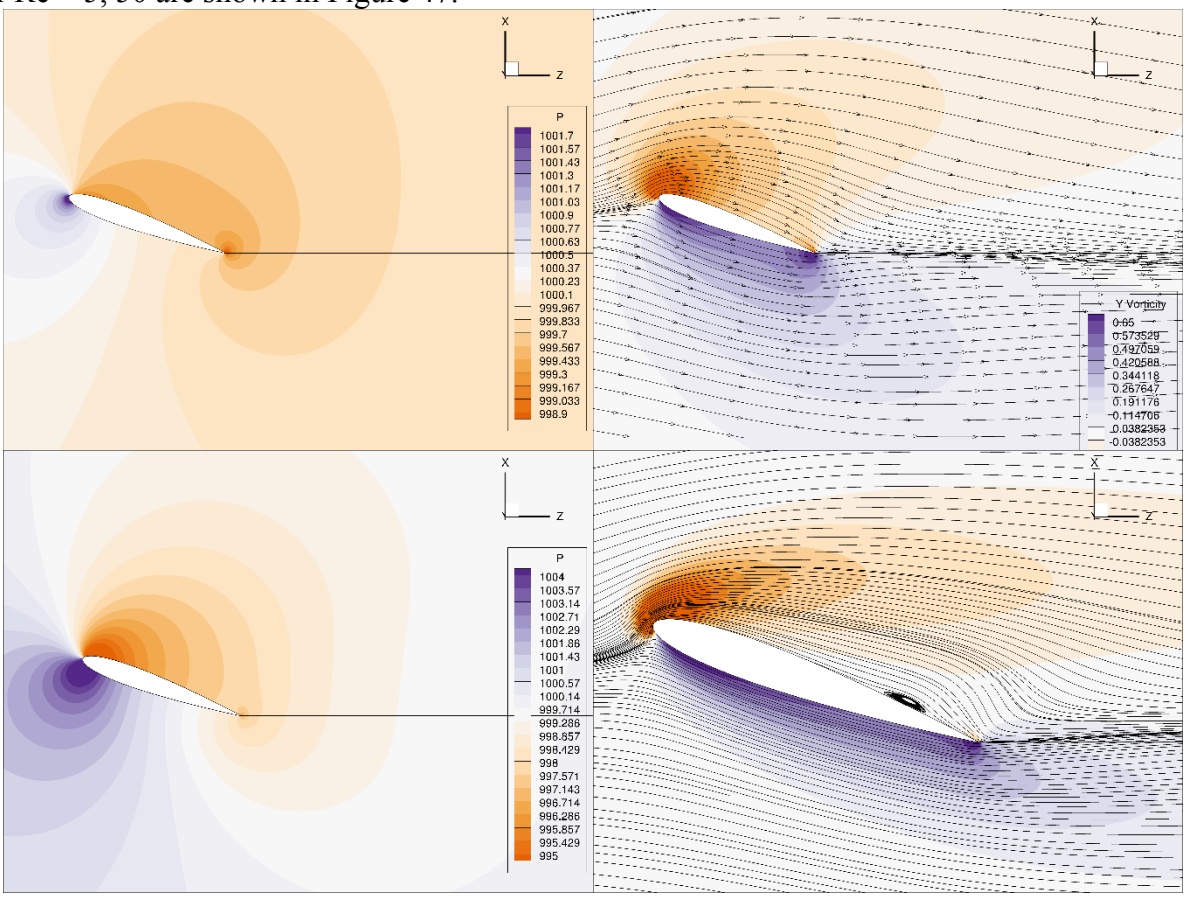

Figure 47. Pressure (left) and vorticity field (superimposed on the streamlines, right) for flow around laminar hydrofoil at Re = 5 (top), 50 (bottom)

The vortex shedding is reported to get very regular at Re = 800. So the vorticity contour is plotted in Figure 48.

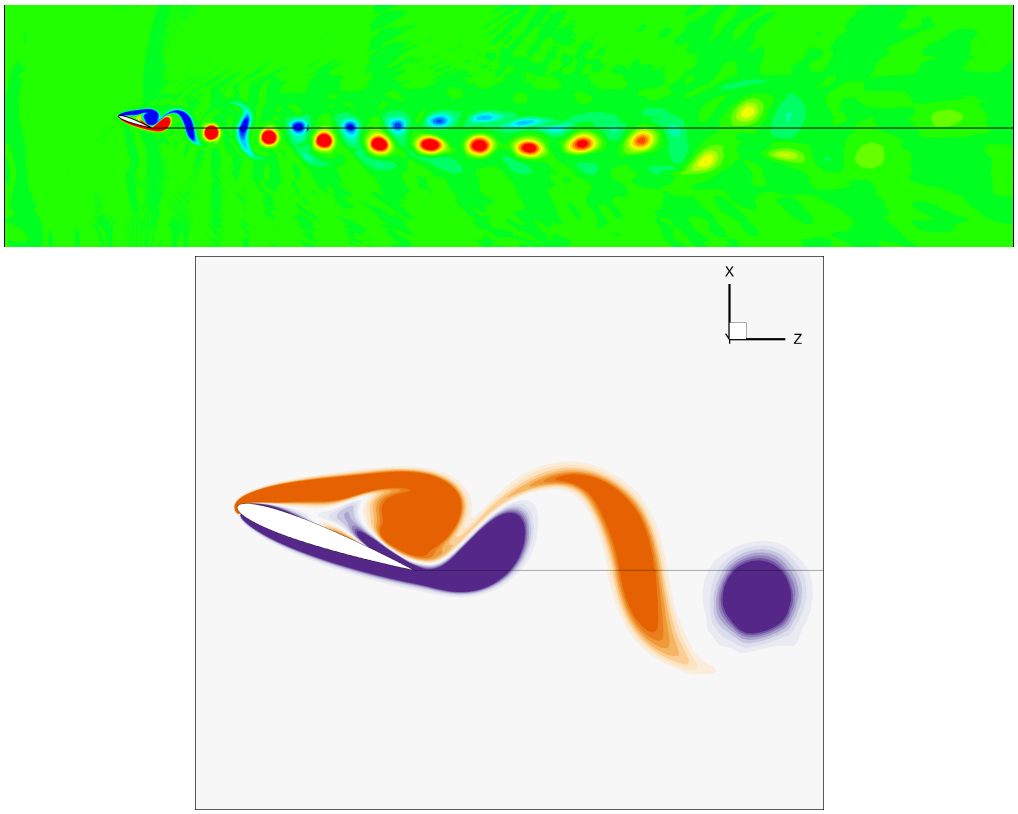

Figure 48. Regular vortex shedding for NACA0012 at Re = 800

To check for regular periodicity and amplitude of the drag and lift force, the drag and lift coefficients are plotted in Figure 49.

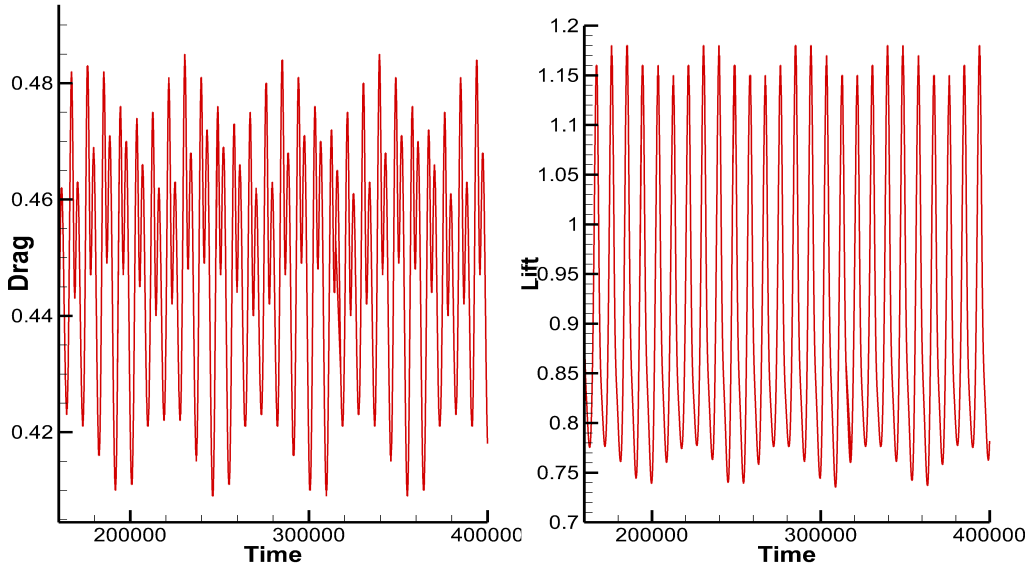

Figure 49. Regular drag and lift force time history for flow around NACA0012 airfoil with AoA = 20

The drag and lift coefficients reported in the literature for this case is $C_l = 0.96$, $C_d = 0.45$, which is in perfect agreement with our simulations. As the Reynolds number increases the flow pattern gets more complicated due to presence of other mechanisms of instability The complex and rich flow pattern is shown in Figure 50 for Re = 3000.

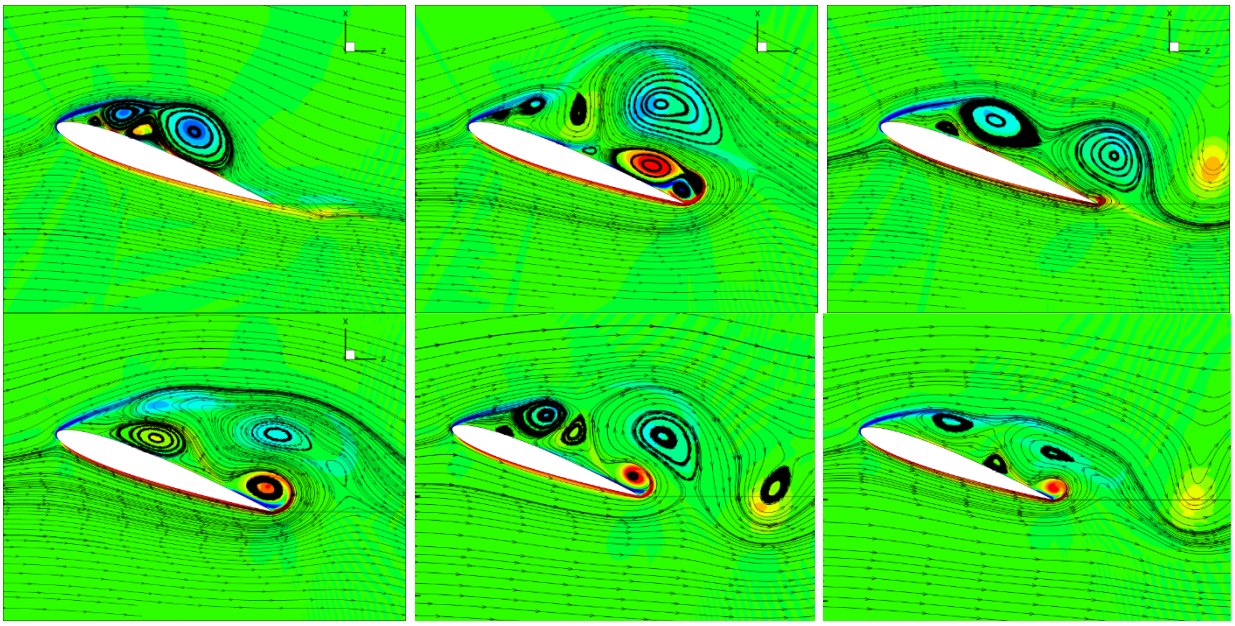

Figure 50. Rich flow physics around airfoil at Re = 3000

It is reported in the literature that instability mechanism for higher Reynolds numbers is mainly due to the Kelvin-Helmholtz instability from the strong shear layer at the leading edge of the airfoil. To visualize this feature, the pressure contours are plotted for Re = 4000 and compared to the available data in the literature. Both the reported data and our result are plotted for comparison in Figure 51.

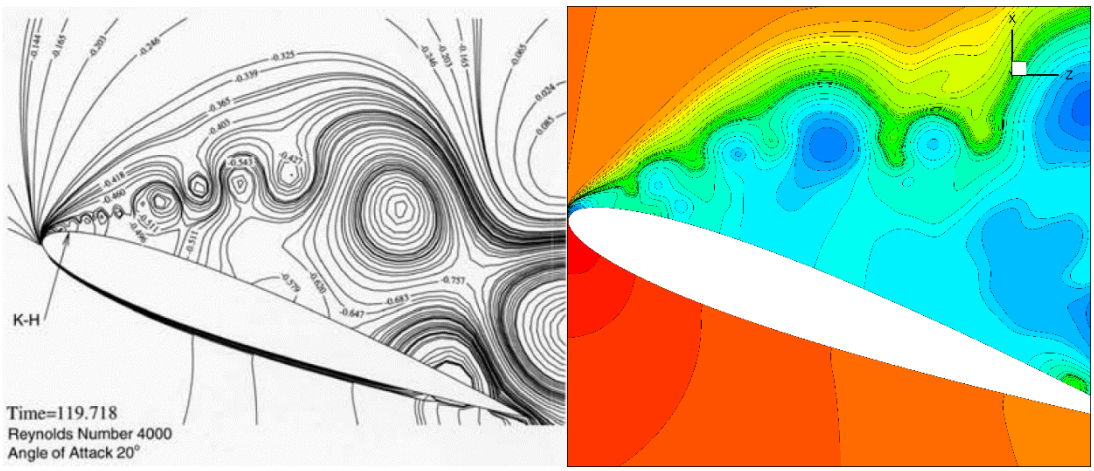

Figure 51. The shear layer instability in the form of K-H instability.
Left: reported literature, Right: Our result

Figure 51 shows that even though our grid is coarser, we could still capture correctly the K-H instability initiated from the shear layer at the leading edge. The code was also tested for the 3D test cases of airfoils. We considered the same problem, i.e. NACA0012 with AoA = 20, but with 3D simulation. The vorticity isosurfaces are plotted in Figure 52.

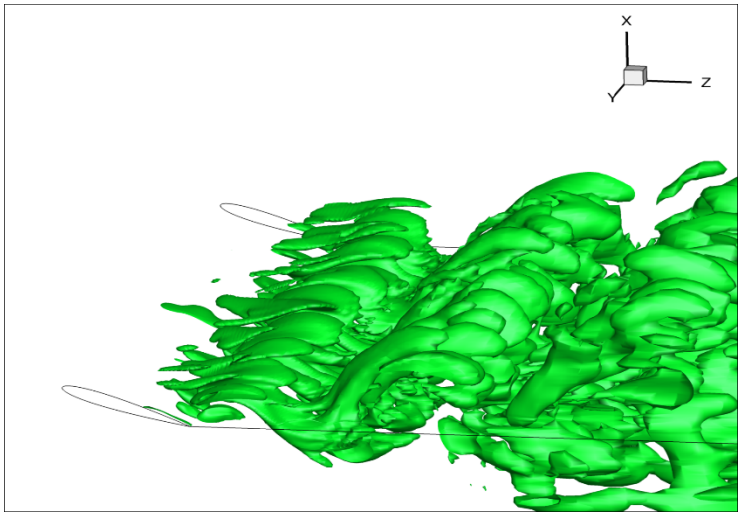

Figure 52. z-vorticity isosurface for Re = 800 around NACA0012 with AoA = 20

Figure 52 shows the 3D character of flow for this Reynolds number. To validate the code for turbulent flows, we extended the turbulence model to enable us for airfoil simulations. We considered E387 profile for a Reynolds number of Re = 200000 at AoA = 6°. The lift and drag coefficients are reported for this test case in the literature. The drag and lift coefficients are plotted in Figure 53.

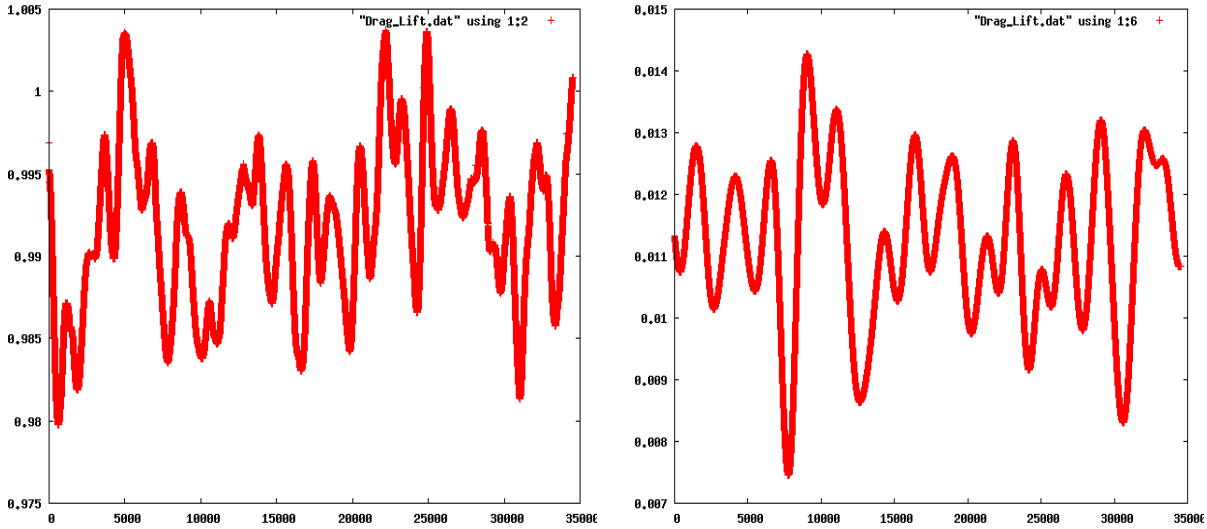

Figure 53 Drag and lift coefficients time history for turbulent flow around NACA0012 at AoA = 6

Table 3 summarizes the result for these force coefficients.

Table 3. Summary numerical results for flow around hydrofoils.

	Experiment	Present
Lift Coeff.	0.990	0.993
Drag Coeff.	0.14	0.115

Based on Table 3, the force coefficients are in good agreement with the experimental data of M. Selig.

Finally, we end this test case with study on the flow visualization for the laminar separation bubble length, separation point, the reattachment point and transition to turbulence. These lengths are shown in Figure 54.

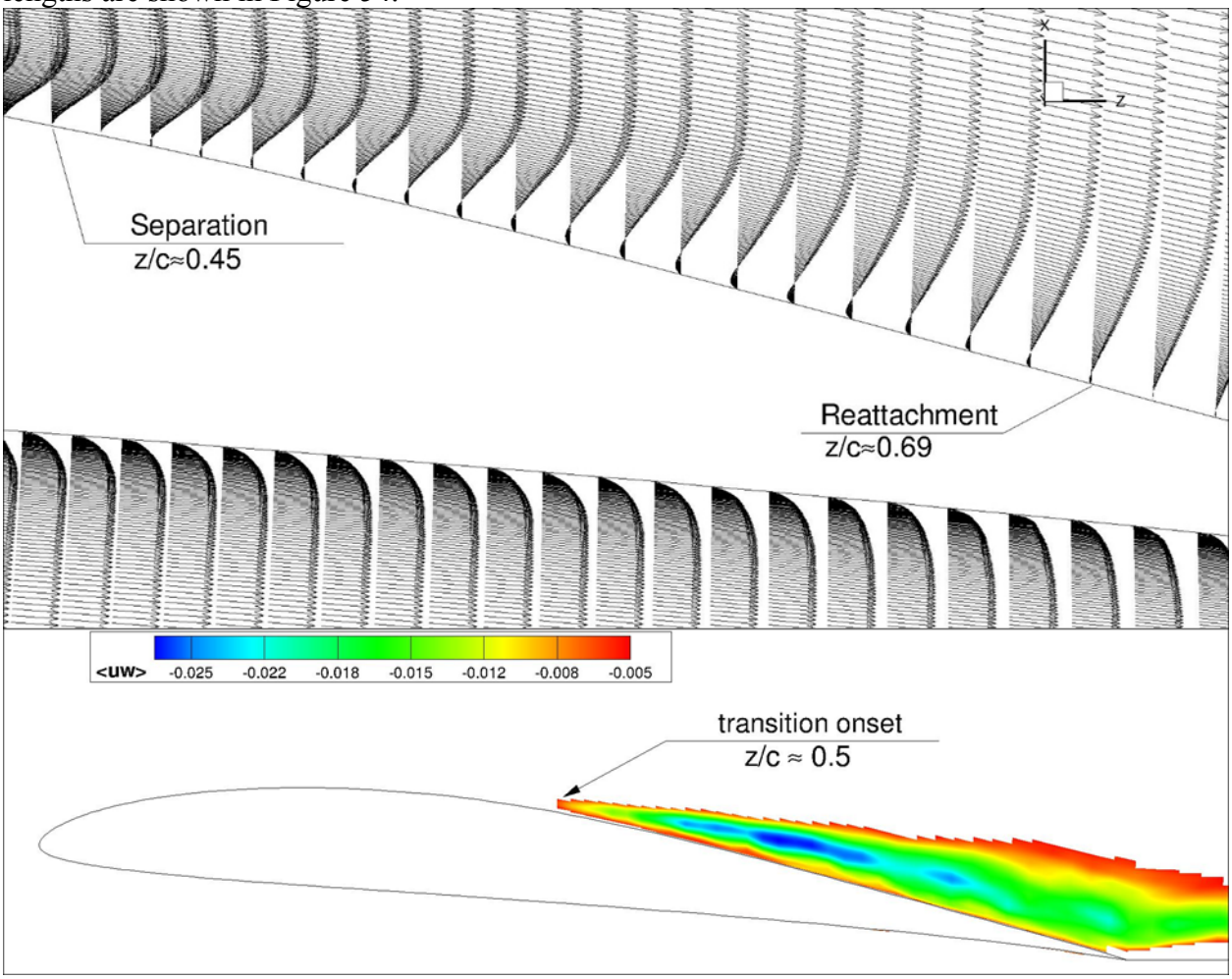

Figure 54. Separation, reattachment and point of transition to turbulence for flow around E387 profile. Top: contours of time-averaged streamwise velocity; Middle: time-averaged velocity vectors close to the hydrofoil surface; Bottom: contours of the Reynolds stress <uw> close to the hydrofoil surface

Contours are averaged in the spanwise direction. In the presence of a laminar separation bubble, transition takes place in the free shear layer above the surface of the airfoil. Downstream of this point, reattachment occurs in a process that is known to be unsteady as vortices are periodically generated and impinge on the airfoil surface. The experimental reported data and the results from our LES calculation are presented in table below.

Table 4. Comparison of LSB length, separation and Reattachment point

	Experiment	Present
Laminar separation point (z/c)	0.37	0.45
Reattachment point (z/c)	0.59	0.65
LSB length (Δz/c)	0.22	0.20

Comparing our calculated results, we conclude that our extended code for flow around hydrofoils shows promising results and was able to capture the correct physics.

5.5. Wall models for flow around hydrofoils

The requirement for the first grid line being in the viscous sublayer imposes computationally intense limitation on the resolution of grid near hydrofoil surface and any other walls in the computational domain. To address this issue, wall-models are employed. We implemented the wall model based on proposed model of Cabot & Moin (2000) and Wang & Moin (2002).

To validate the implemented wall model, we considered the fully-developed turbulent channel flow problem for Re_τ (shear velocity Reynolds number) of 180, 4000, 2000. The results were compared with DNS (direct numerical simulation) data of Jimenez (2006). Moser (1999) and Jimenez (2014). All of the results showed promising results for time-averaged, spatially-averaged velocity profiles and turbulence intensities. The comparison for $Re_\tau = 180$ are plotted in Figure 55.

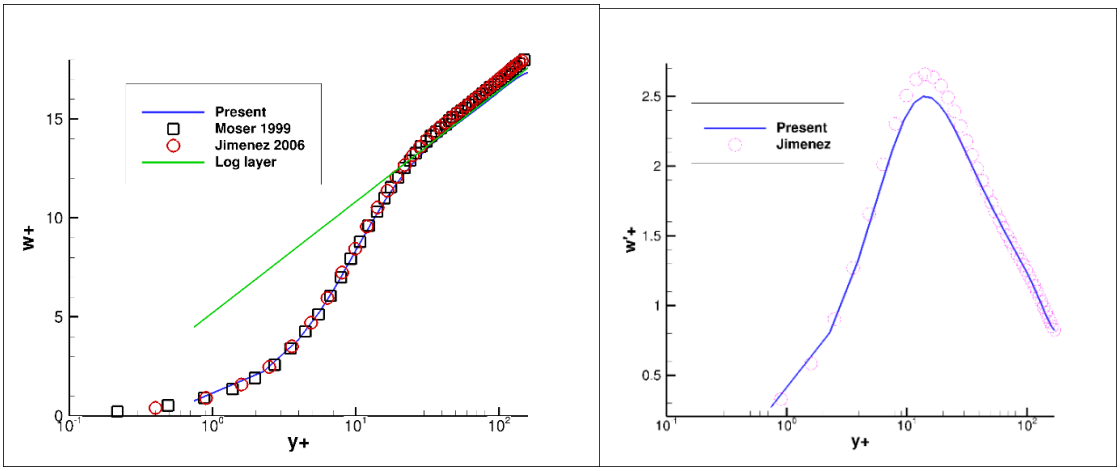

Figure 55. Law of the wall behaviour (left) and w_{rms} for the turbulent channel flow at $Re_\tau = 180$

Figure 55 shows a good agreement for 1st and 2nd order statistics of flow versus the reported DNS data of Moser and Jimenez. For the higher $Re_\tau = 20000$, the comparison of results with those of Jimenez is plotted in Figure 56.

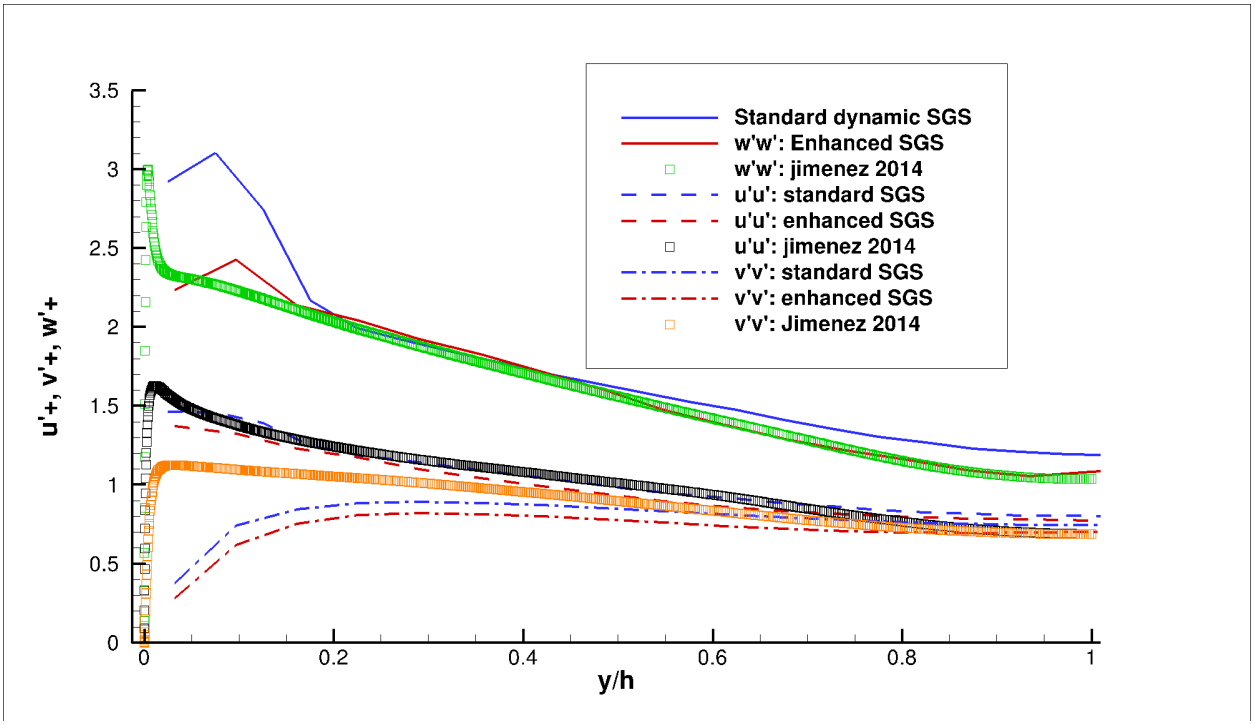

Figure 56. Comparison of second order statistics for channel flow
Our simulation: LES, Jimenez: DNS

Figure 56 also shows satisfactory results for the wall model implementation for the hydrofoil computational code.

5.6. SAFL Hydrofoil simulation

We have also implemented the same wall-model and proper boundary condition (wake-cut boundary conditions) for hydrofoil simulation for the gas phase. To replicate the experimental conditions, we simulated the liquid phase first to reach the steady turbulence and then we released gas from the hydrofoil. The pressure field around SAFL hydrofoil for U =10m/s and AoA = 8 is shown in Figure 57.

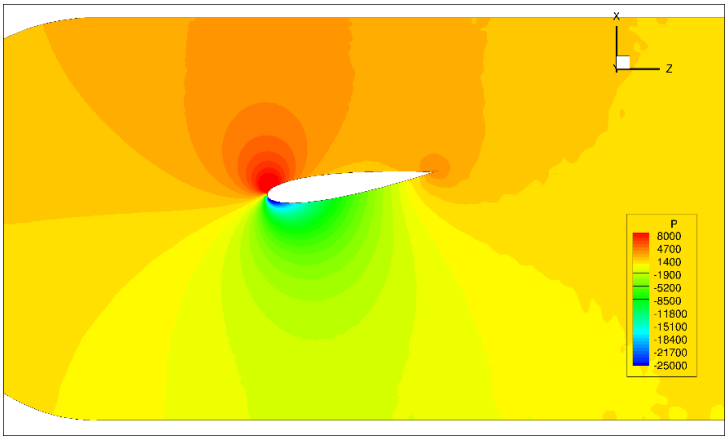

Figure 57. Pressure field in the water tunnel for U = 10m/s and AoA = 8.

Some initial results from the aerating hydrofoil are plotted in Figure 57. The void fraction field is plotted in Figure 58.

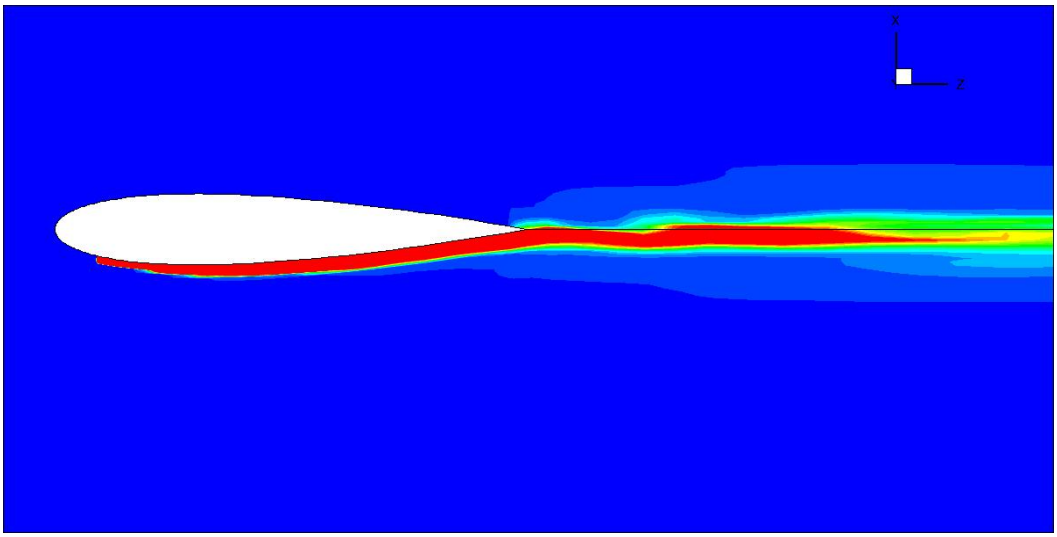

Figure 58. Gas holdup for NACA0015 at SAFL with 0.5 LPM of gas release rate with U_∞= 10 m/s with AoA = 0

As Figure 58 indicates, void fraction in the wake is observed to decrease gradually upon vertical displacement away from the centerline. However, a careful scrutiny of the void fraction field shows that the maxima of void fraction is achieved slightly below the centerline. Further, it is NOT symmetrical about the center line, rather such a symmetry is observed with respect to the injection slot location. Overall, these trends match pretty well with the trends observed in the experimental measurements as shown before. However, the above figure does not reveal any information about the spanwise spread of the wake. Such a trend is visible upon plotting the iso-surface of the void fraction, as shown in Figure 59.

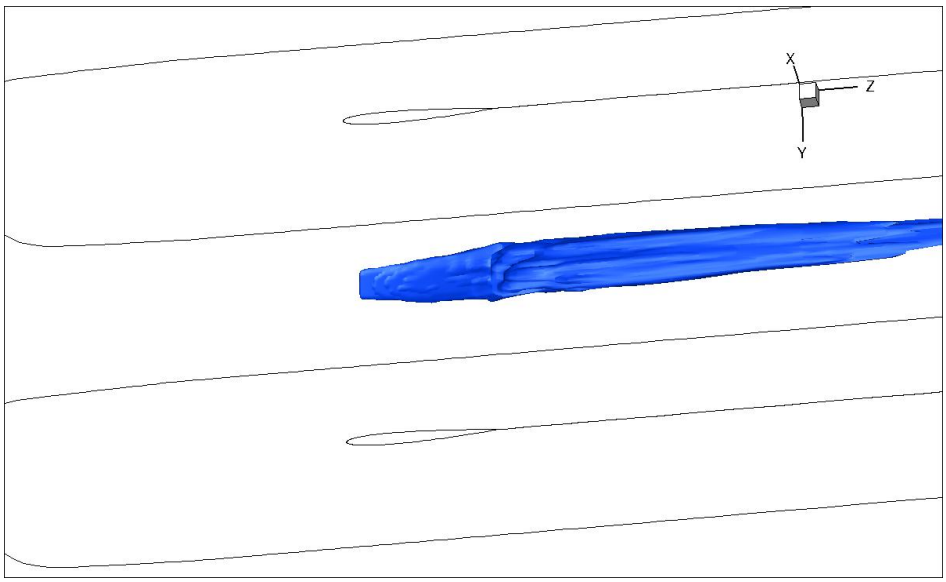

Figure 59. Iso-surface of void fraction

As Figure 59 indicates, a slight lateral expansion of the bubbly wake is observed between the injection slot and the trailing edge. However, upon further movement in the streamwise direction, no significant expansion of the wake is observed. It is noteworthy that similar observations have been reported by the wake width observations for the ventilated hydrofoils by previous authors (Karn et al. 2015a,b).

VII. Accomplishments

A high-speed bubble field image acquisition technique coupled to newly developed and improved algorithms to identify and characterize the bubble fields in the images obtained with high-speed video were successfully implemented. The wake behind a ventilated hydrofoil was investigated using the described techniques and algorithms. The bubbles in the wake of the ventilated hydrofoil were well captured, and their velocities were seen to represent the velocity field of the wake.

A final goal of these experiments was to investigate the effects of flow field on the resulting rate of oxygen transfer in the wake. Gas transfer was quantified through disturbed equilibrium measurements of dissolved oxygen (DO) concentration under different operating conditions. A one-dimensional mass transfer model was developed to lend insight into the mass transfer characteristics observed in these experiments using a mass transfer conservation equation and a predictive relation for K_L by Azbel (1981). For ease of application, mean free stream velocity (U) was substituted for characteristic turbulent velocity (u') in the predictive relation. Thus, a β coefficient was introduced to account for this difference, $\beta = (u'/U)^{3/4}$ where u'/U is the turbulence intensity. This β coefficient was determined by fitting the prediction of the numerical model with the experimental data obtained from the DO measurements in the water-tunnel. The gas transfer model required the flow information and Sauter mean bubble diameter as an input to predict the rate of gas transfer. The Sauter mean diameter of bubbles at different test conditions in the wake was determined by shadow imaging experiments.

The overall results of this study can contribute towards the development of a computational model that can relate the flow conditions in the bubbly flow regime to the bubble sizes entrained in the flow field and the resultant gas transfer. The current study provides a rich dataset on bubble sizes, void fraction in the wake and the rate of volatile compound (oxygen) transfer as a function of flow field parameters that can be used in the validation of computational models. Such computational models will enhance aeration design of auto-venting hydroturbines.

The following refereed publications resulted from this project:

1. Karn, A., Monson, G.M., Ellis, C.R. Hong, J., Arndt, R.E.A. and Gulliver, J.S. (2015). Mass transfer studies across ventilated hydrofoils: a step towards hydroturbine aeration, *International Journal of Heat and Mass Transfer*, 87,512-520.
2. Karn, A.. Ellis, C.R., Milliren, C., Hong, J., Scott, D., Arndt, R.E.A. and Gulliver, J.S. (2015). Bubble size characteristics in the wake of ventilated hydrofoils with two aeration configurations, *International journal of Fluid Machinery and Systems*, 8(2), 73-83.
3. Karn, A., Ellis, C., Arndt, R., and Hong, J. (2015). An integrative image measurement technique for dense bubbly flows with a wide size distribution, *Chemical Engineering Science*, 122, 240-249.
4. Lee, S.-J., Kawakami, E. and Arndt, R.E.A. (2014). Application of shadow image velocimetry to a ventilated hydrofoil wake, Journal of Visulaization, 17(4), 327-335.
5. Karn, A., Ellis, C. Hong, J., Arndt, R.E.A. (2015). Investigations into the turbulent bubbly wake of a ventilated hydrofoil: moving toward improved turbine aeration techniques, *Experimental Thermal and Fluid Science*, 64, 186-195.

6. Lee, Seung-Jae, Kawakami, E. and Arndt, R.E.A. “Recognition of highly overlapping bubbles in the wake of a ventilating hydrofoil” Proceedings of the 8th International Symposium on Cavitation August 14-16, 2012, Singapore.
7. Lee, Seung-Jae, Kawakami, E. and Arndt, R.E.A. “Measurements in the wake of a ventilated hydrofoil” Proceedings of ASME 2013 Fluids Engineering Division Summer Meeting FEDSM 2013 July 7-11, 2013, Incline Village, Nevada.
8. Ellis, C., A. Karn, J. Hong, S. J. Lee, E. Kawakami, D. Scott, J. Gulliver, R.E.A. Arndt, “ Measurements in the wake of a ventilated hydrofoil: A step towards improved turbine aeration techniques”. IOP Conf. Ser.: Earth Environ. Sci. 2014, 22 062009.

In addition, the following presentations were given on this project:

1. Arndt, REA “Turbine aeration design software for mitigating adverse environmental impacts resulting from conventional hydropower turbines” DOE Water Power Peer Review, Arlington, VA Feb. 24, 2014.
2. Arndt, REA “Measurements in the wake of a ventilated hydrofoil” Proceedings of ASME 2013 Fluids Engineering Division Summer Meeting FEDSM 2013 July 7-11, 2013, Incline Village, Nevada.
3. Arndt, REA “Improved performance with ventilation” 66th Annual Meeting of the Division of Fluid Dynamics of the American Physical Society, 24-26 November 2013, Pittsburgh, PA.
4. Arndt, REA “Turbine aeration design software for mitigating adverse environmental impacts resulting from conventional hydropower turbines” DOE Water Power Peer Review, Arlington, VA Feb. 24, 2014.
5. Karn, A. “Bubble size measurements in a bubbly wake”, 67th Annual Meeting of APS-DFD, San Francisco, 2014.
6. Gulliver, J.S., “Oxygen transfer across ventilated hydrofoils”. The 7th International Symposium on Gas Transfer at Water Surfaces, Seattle, 2015.
7. Arndt, R.E.A., “ Measurements in the wake of a ventilated hydrofoil: A step towards improved turbine aeration techniques”, 27th IAHR Symposium Hydraulic Machinery and Systems, Montreal, Canada, 2014.
8. Scott, D., Michael Sabourin, Sebastien Beaulieu, Christopher Ellis, Ashish Karn, “Optimizing dissolved oxygen transfer in Auto-venting turbines”, HydroVision International 2015, Portland, OR.
9. Hadj Mohammadi, M. and F. Sotiropoulos, "A computational model for large eddy simulation of dilute bubbly turbulent flows,” 66th American Physical Society, Division of Fluid Dynamics conference, November 2013, Pittsburgh, PA.

Finally, the following theses resulted from this project:

1. Monson, Garrett, “Study of Mass Transfer across Hydrofoils for use in Aerating Turbine,” M.S. Thesis, University of Minnesota, 2013.
2. Karn, Ashish, “Fluid dynamics of multiphase flows for applications in next generation underwater vehicles and aerating hydroturbines,” Ph. D. Thesis, University of Minnesota, 2015.

VIII. Conclusions

Our initial bubble analysis was carried out at relatively low airflow rates. It was found that as airflow rate was increased, bubble fields were produced that were too dense to employ the bubble shadow technique in its original configuration. Bubbles became indistinguishable at the higher flow rates that were deemed necessary for a practical air injection system. Lacking a viable alternative measurement technique, it was decided to reduce the ventilation slot length by 95%, masking off all but the center 5% of the slot. The air flow rates used in the gas transfer experiments were likewise reduced by 95% for these tests maintaining the specific air discharge (flow rate per unit slot length). All other parameters were held constant. It was felt that this technique would be equivalent to illuminating the wake with a thin sheet of light. Masking off all but the center 5% of the ventilation slot did not substantially alter the bubble size distribution, supporting our contention that the experiments accurately represent the flow physics of the original full slot gas transfer experiments.

The velocity characteristics of a bubbly flow can be obtained with the shadow image technique described here including direct image processing methods. With further analysis, it is expected that this technique can be used to more fully characterize the associated bubble plume distribution and velocity field under a variety of test conditions. The shadow imaging experiments in the bubbly wake of the SAFL hydrofoil for a reference case revealed that roughly 50% of the bubbles are quite small (< 0.35mm diameter). It was also found that larger bubbles (diameters between 0.5 mm and 1.5 mm) are the primary contributors to the total surface area of the bubbles, one of the primary drivers of gas transfer. Sauter mean diameter (SMD) increases by 11-14% (SAFL foil) and 11-31% (Alstom foil) as the ventilation airflow rate is tripled at all liquid velocities and decreases by 23-35% (SAFL foil) and 44-59% (Alstom foil) when the liquid velocity is doubled at the same airflow rate. The hydrofoil wake develops in a similar fashion at identical flow rates, with only the change in the bubble sizes as the superficial liquid velocities are varied. An increase in angle of attack from 0 to 8 degrees leads to a 10-29% (SAFL foil) and 17-60% (Alstom foil) decrease in SMD, water velocity and ventilation air flow rate being the same, although a consistent trend in gas transfer characteristics is not observed across all the conditions.

The position of the air injection had a significant effect on the bubble size distribution. Injection at the trailing edge resulted in larger bubbles, most noticeably at 0 degree angle of attack, presumably due to reduced shearing in the flow compared to injection close to the leading edge where the injected gas flow shears immediately on exit and mixes with the outer flow more effectively.

The rate of approach towards steady state concentration, as indicated by the K_La value curve-fit to the DO measurements, increased with an increase in air injection rate and approach velocity, and was relatively independent of angle of attack. It is noteworthy that the fitted K_La values for the two locations of air injection were relatively close under otherwise similar conditions. Thus, while the Sauter mean diameter was greater for the tail injection of air, the K_La values were close to the same. This is attributed to one, or both, of two potential causes. 1) The separation zone with trailing edge injection of air is substantially narrower than with injection close to the leading edge. This would expose the injected bubbles to a higher turbulent velocity, which may

have made up the difference that would be expected between the two injection points. 2) The bubbles are coalescing into larger bubbles or shearing down into smaller bubbles in another portion of the water tunnel, resulting in the characteristic bubble size being determined by the flow in this coalescence or shearing region.

The results of the model show that β decreases slightly with increasing angle of attack, is independent of ventilation air flow rate and water velocity for the SAFL foil. For the Alstom foil, it decreases with increasing water velocity but, again, is independent of ventilation air flow rate. Thus, particularly for the SAFL foil and for a given angle of attack, one of these values of β coefficient can serve as an input in a computational model that can numerically relate the DO uptake with the flow field. This is believed to be the first verification of Azbel's K_L relationship, because other attempts have not had the experimental measurements of bubble size distribution provided by this study and relied on empirical formulations for bubble size and surface area.

IX. Recommendations for Future Work

Our experimental procedures have been developed to the point that they can readily serve to evaluate future aerating turbine runner designs.

Future designs of hydrofoils can be tested for oxygen transfer in the water tunnel. In addition, one surprise of the comparative oxygen transfer tests on the SAFL and Alstom foils was that the K_La values were close to the same for the two foils operating under similar test conditions in spite of the differences seen in bubble population. Two possible reasons for this observation were given in sections V.4.3 and VI. A sensitivity investigation on this comparison would seem to be justified. The sensitivity investigation would be accomplished by installing a device designed to release larger bubbles into the test section of the water tunnel and running similar oxygen transfer tests on this device. A simple single orifice would suffice for this purpose. The comparison with the prior tests on the SAFL and Alstom foils would be informative.

It had been hoped that making DO measurements upstream and downstream of the water tunnel test section might allow us to differentiate mass transfer processes that are directly connected to the hydrofoil from those associated with the rest of the recirculating tunnel. Due to DO measurement uncertainty, this proved impossible. It may be possible to revisit this idea in future work, looking for alternative methods and/or devices capable of providing these measurements.

In addition, we think that expanding our ability to observe and differentiate bubble dynamics in other portions of the flow circuit would help in identifying the important features in the oxygen uptake process. This would be important in identifying the essential components of an aerating turbine-draft tube system with regard to oxygen uptake.

We propose to include the sharp-interface immersed boundary formulation to our developed two-phase flow code. A difficulty in the simulation of aerating turbines is the complex geometry of the blades, which prohibit us from utilizing a body-fitted grid. This drawback becomes more pronounced in real world complex rotating hydrofoils. Having a computational code capable of simulating flow around complex moving bodies is a key element in the simulation of aerating turbines. In aerating turbines, the rate of bubble breakup and coalescence is high. This element should be added to our computational code, allowing us to perform simulations of turbulent bubbly flows including the breakup and coalescence processes.

We also suggest adding an algorithm to the flow code to account for mass (DO) transfer across the bubbles. Many of the equations in the existing 1-D mass transfer model could be utilized to develop this algorithm. The result would be a computational code that could predict the oxygen transfer performance of a hydroturbine.

X. Acknowledgments

Professor Can Kang (on leave from Jiangsu University) provided considerable help in interpreting the data. Special mention must go Dr. Seung-Jae Lee and Mr. Ellison Kawakami who are responsible for development of SIV technique and the initial bubble image processing have left the project, but have continued to provide input to the preparation of this report. This project is supported by grants from the DOE EERE – Wind & Water Power Program, Dr. Jose Zayas, and Gary Nowakowski, Program Managers, from Alstom Power, Inc. and from the Institute on the Environment, University of Minnesota.

XI. References

ASCE (2007) Measurement of Oxygen Transfer in Clean Water: ASCE standard, ASCE/SEI 2-06, ISBN-13: 978-0-7844-0848-3, Reston, VA

Azbel, D., Two-phase flows in chemical engineering, K. Philip, Ed., New York, New York: Cambridge, (1981).

Canny, J., A Computational Approach to Edge Detection, IEEE Transactions on PAMI, 8(6) , 679-698, (1986)

Cabot, W., Moin, P, Approximate wall boundary conditions in the large-eddy simulation of high Reynolds number flow, Flow, Turbulence and Combustion, 63(1-4), 269-291, (2000).

Daniil, E.I., and Gulliver, J.S., Temperature dependence of liquid-film coefficient for gas transfer, J. Environ. Eng. 114(5) 1224–1229, (1988).

Deen, N. G., Hjertager, B. H., Solberg, T., Comparison of PIV and LDA measurement methods applied to the gas-liquid flow in a bubble column, Proceedings of the 10th international symposium on applied of laser techniques to fluid mechanics, Lisbon (Portugal), 38, (2000).

Drew, D. A., Passman, S. L., Theory of multicomponent fluids, Springer, (1999).

Ge, L., Sotiropoulos, F., A numerical method for solving the 3D unsteady incompressible Navier–stokes equations in curvilinear domains with complex immersed boundaries, Journal of computational physics, 225 (2), 1782–1809, (2007).

Germano, M., Piomelli, U., Moin, P., Cabot, W. H., A dynamic subgrid-scale eddy viscosity model. Physics of Fluids A: Fluid Dynamics, 3(7), 1760-1765, (1991).

Ghia, U. K., Kirti, N. G., Ghia, N., Shin, C. T., High-Re solutions for incompressible flow using the Navier-Stokes equations and a multigrid method, Journal of computational physics, 48, 387-411, (1982).

Giovannettone, J.P. and Gulliver, J.S., Gas Transfer and Liquid Dispersion Inside a Deep Airlift Reactor, AIChE J. 4(54), 850-861, (2008).

Hibiki, T., Ishii, M., Lift force in bubbly flow systems, Chemical Engineering Science, 62 (22), 6457–6474, (2007).

Honkanen M., Saarenrinne, P., Stoor, T., Niinimaki, J. (2005), "Recognition of highly overlapping ellipse-like bubble images," Measurement Science and Technology, 16, 1760-1770.

Hoyas, S., Jiménez, J., Scaling of the velocity fluctuations in turbulent channels up to Re_τ= 2003. Physics of Fluids, 18(1), 011702, (2006).

Karn, A., Ellis, C., Hong, J., Arndt, REA, An integrative image measurement technique for dense bubbly flows with a wide bubble size distribution, Chemical Engineering Science, 122, 240-249, (2015a).

Karn, A., Ellis, C., Arndt, REA, Hong, J., Investigations into the turbulent bubbly wake of a ventilated hydrofoil: moving towards improved turbine aeration techniques, Experimental Thermal and Fluid Science. (2015b). In Press.

Lakehal, D., Smith, B. L., Milelli, M., Large-eddy simulation of bubbly turbulent shear flows, Journal of Turbulence, 3, N25, (2002).

Lee,S.J. Kawakami, E. and Arndt, R.E.A., Application of a shadow image velocimetry to a ventilated hydrofoil wake, Journal of Visualization (2014) 17:327–335.

Lopez de Bertodano, M., Lahey Jr, R., Jones, O., Phase distribution in bubbly two-phase flow in vertical ducts, International Journal of Multiphase Flow, 20 (5), 805–818, (1994).

Lozano-Durán, A., Jiménez, J., Effect of the computational domain on direct simulations of turbulent channels up to Reτ= 4200. Physics of Fluids, 26(1), 011702, (2014).
Milelli, M., Smith, B., Lakehal, D., Large-eddy simulation of turbulent shear flows laden with bubbles, Direct and Large-Eddy Simulation IV, 461–470, (2001).
Monson., Study of Mass Transfer across hydrofoils for use in aerating turbines, Master's thesis. Saint Anthony Falls Laboratory, University of Minnesota (2013).
Moser, R. D., Kim, J., Mansour, N. N., Direct numerical simulation of turbulent channel flow up to Reτ= 590, Phys. Fluids, 11(4), 943-945, (1999).
Parkhill, K.P., and Gulliver, J.S., Indirect Measurement of Oxygen Solubility, Water Res. 31(10) 2564-2572 (1997).
Pla, F., Recognition of Partial Circular Shapes from Segmented, Computer Vision and Image Understanding, 63(3), 334-343, (1996).
Pope, S. B., Turbulent flows, Cambridge university press, (2000).
Sato, Y., Sadatomi, M., Sekoguchi, K., Momentum and heat transfer in two-phase bubble flows, International Journal of Multiphase Flow, 7 (2), 167–177, (1981).
Sauter, J., Determining size of drops in fuel mixture of internal combustion engines, National Advisory Committee for Aeronautics, (1926).
Selig, M. S., McGranahan, B. D., Wind tunnel aerodynamic tests of six airfoils for use on small wind turbines, Journal of solar energy engineering, 126(4), 986-1001, (2004).
Sokolichin, A., Eigenberger, G., Applicability of the standard k-ε turbulence model to the dynamic simulation of bubble columns: Part i. detailed numerical simulations, Chemical Engineering Science, 54 (13), 2273–2284, (1999).
Sokolichin, A., Eigenberger, G., Lapin, A., Lubert, A., Dynamic numerical simulation of gas-liquid two-phase flows Euler/Euler versus Euler/Lagrange, Chemical Engineering Science, 52 (4), 611–626, (1997).
Stenstrom, M.K., L.C. Brown and H.J. Hwang, "Oxygen Transfer Parameter Estimation," J. Env. Engr., ASCE, 107(2), pp 379-397, (1981).
Thompson, E.J. and Gulliver, J.S., Oxygen Transfer Similitude for Vented Hydroturbine, J. Hydraul. Eng. 123(6) 528-538, (1997).
Tropea, C., Yarin, A.L. and Foss, J.F. (Eds), Handbook of Experimental Fluid Mechanics, Springer, (2007).
Wang, M., Moin, P., Dynamic wall modeling for large-eddy simulation of complex turbulent flows, Physics of Fluids, 14(7), 2043-2051, (2002).

XII. Appendix

Velocity Field Plots

AoA 0º Vel 5.0 m/s Air Flow 0.5SLPM

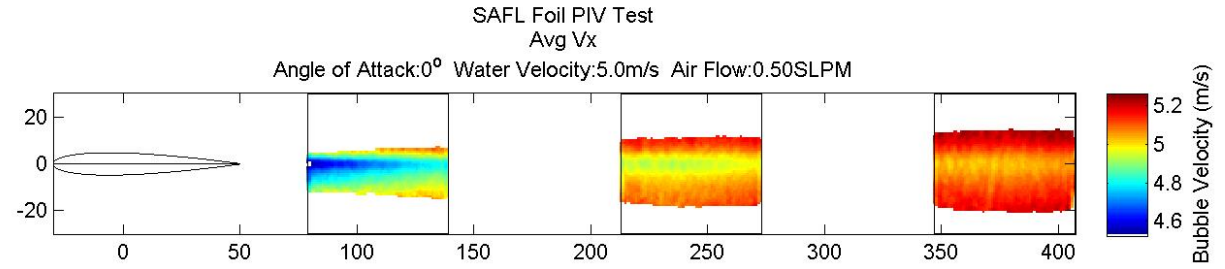

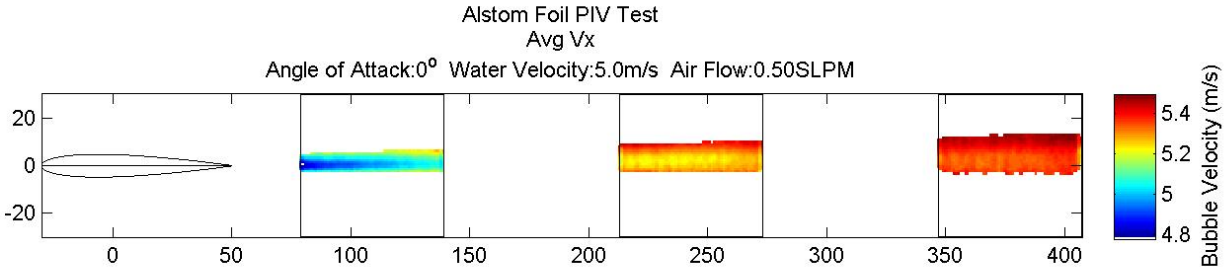

AoA 0º Vel 5.0 m/s Air Flow 1.5SLPM

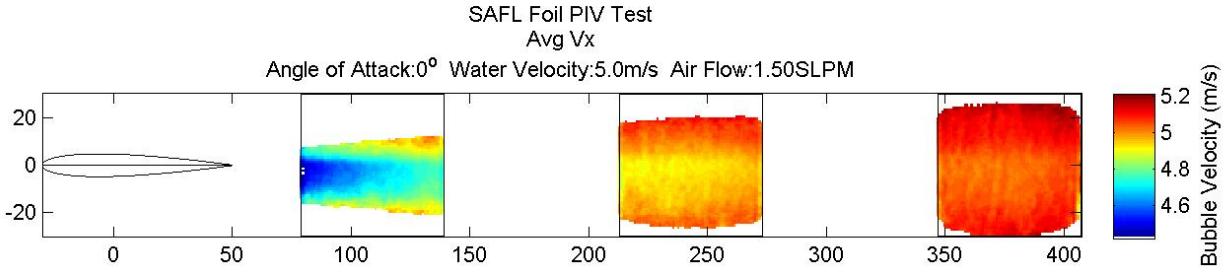

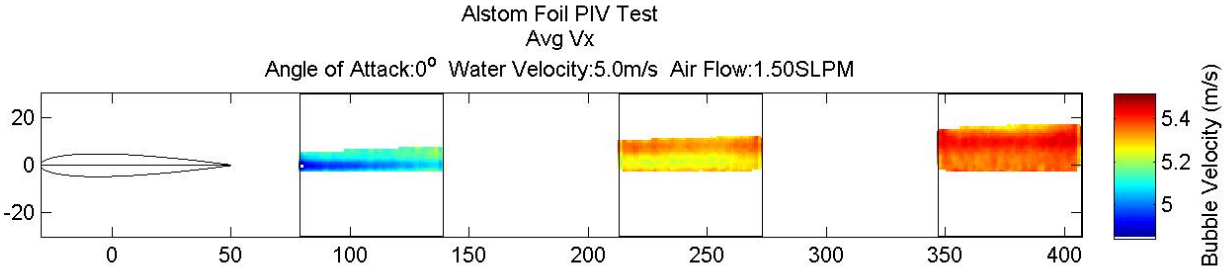

AoA 0º Vel 7.5 m/s Air Flow 1.0 SLPM

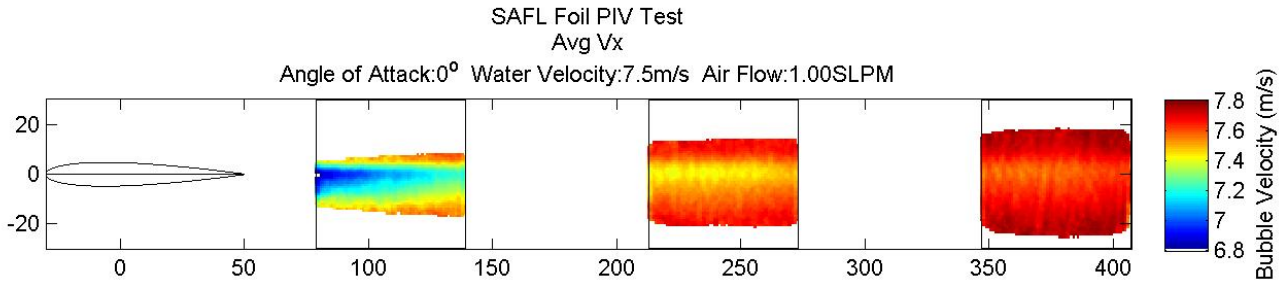

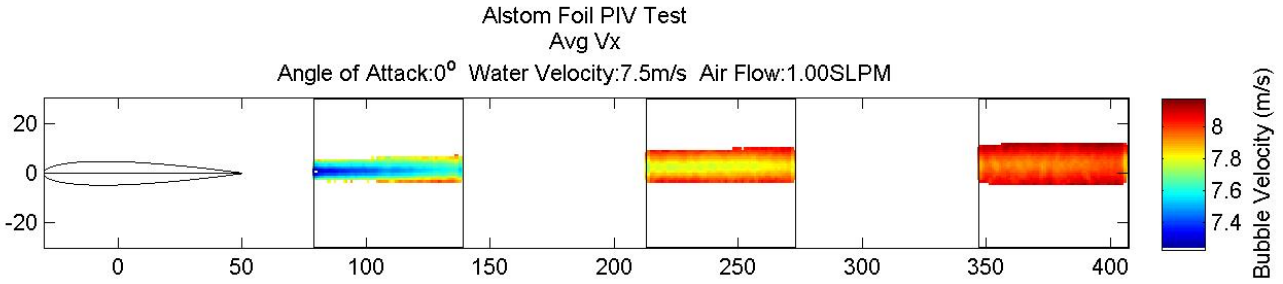

AoA 0° Vel 10.0 m/s Air Flow 0.5SLPM

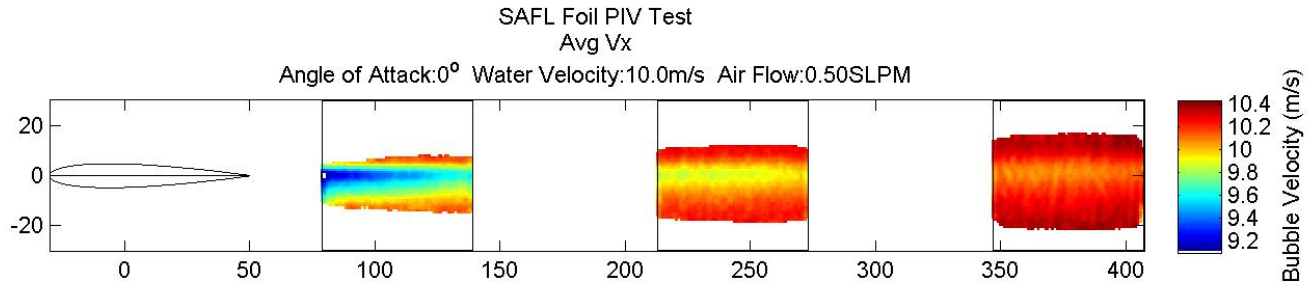

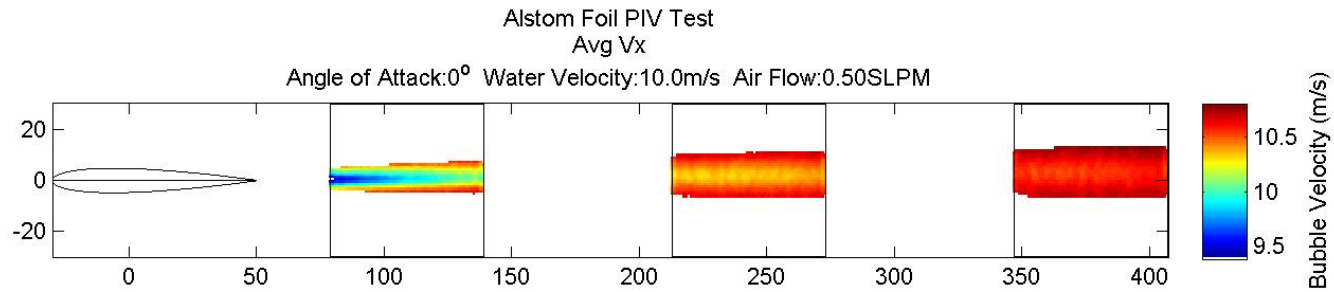

AoA 0° Vel 10.0 m/s Air Flow 1.5SLPM

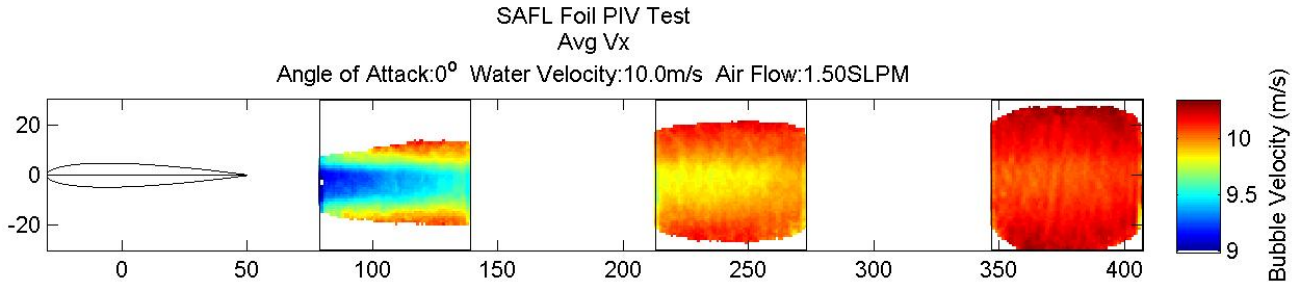

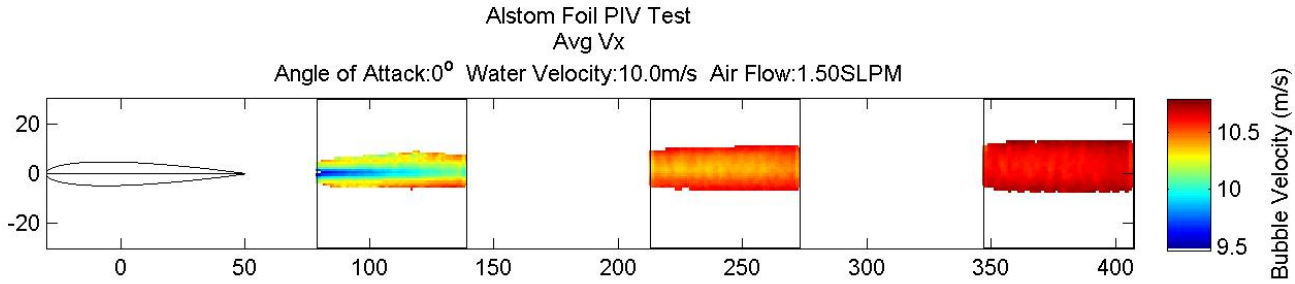

AoA 4° Vel 5.0 m/s Air Flow 0.5SLPM

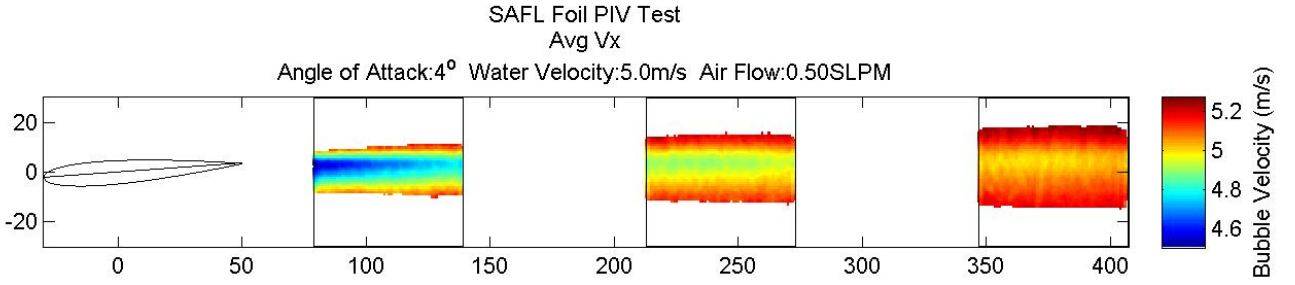

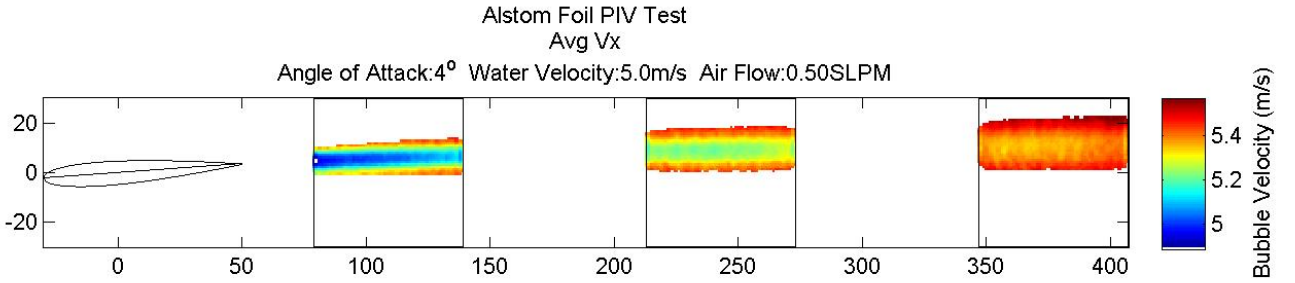

AoA 4° Vel 5.0 m/s Air Flow 1.5SLPM

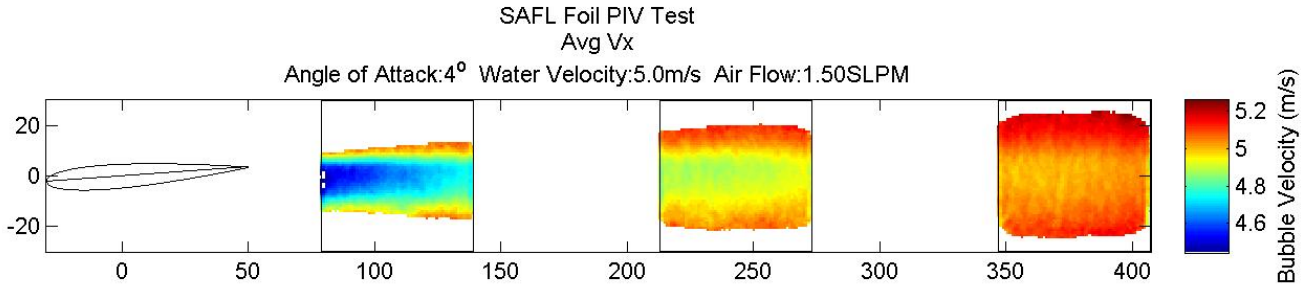

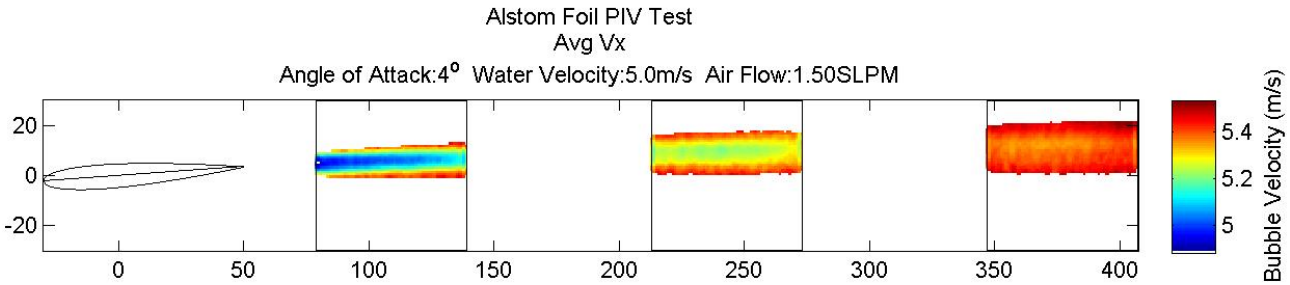

AoA 4° Vel 7.5 m/s Air Flow 1.0SLPM

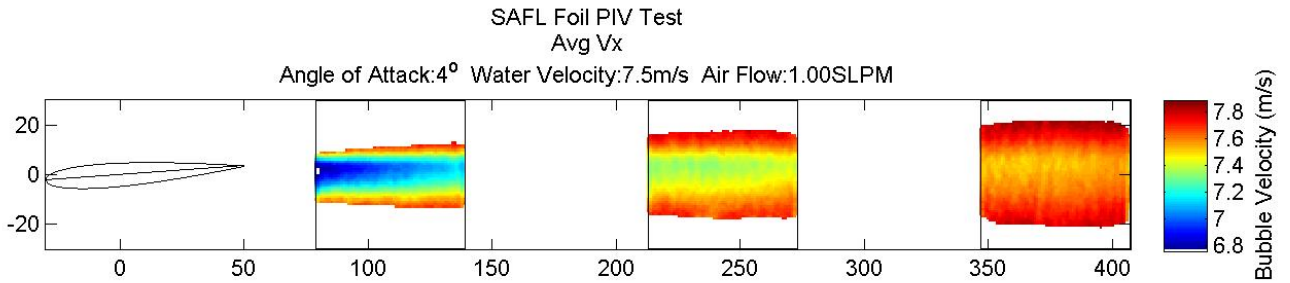

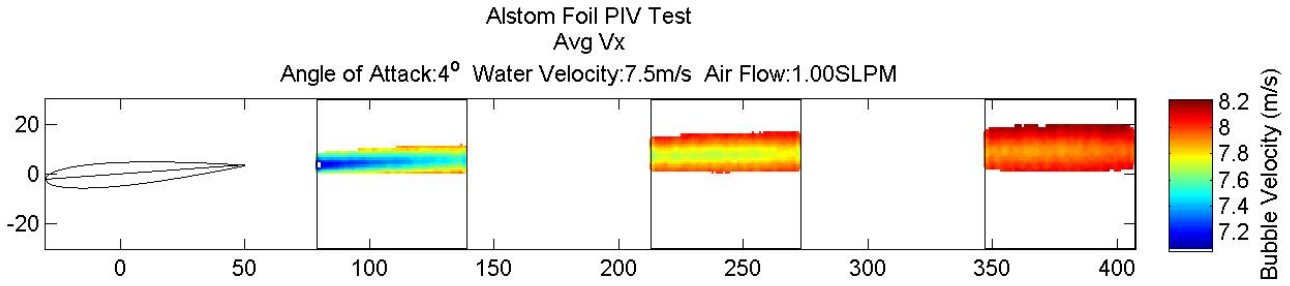

AoA 4° Vel 10.0 m/s Air Flow 0.5SLPM

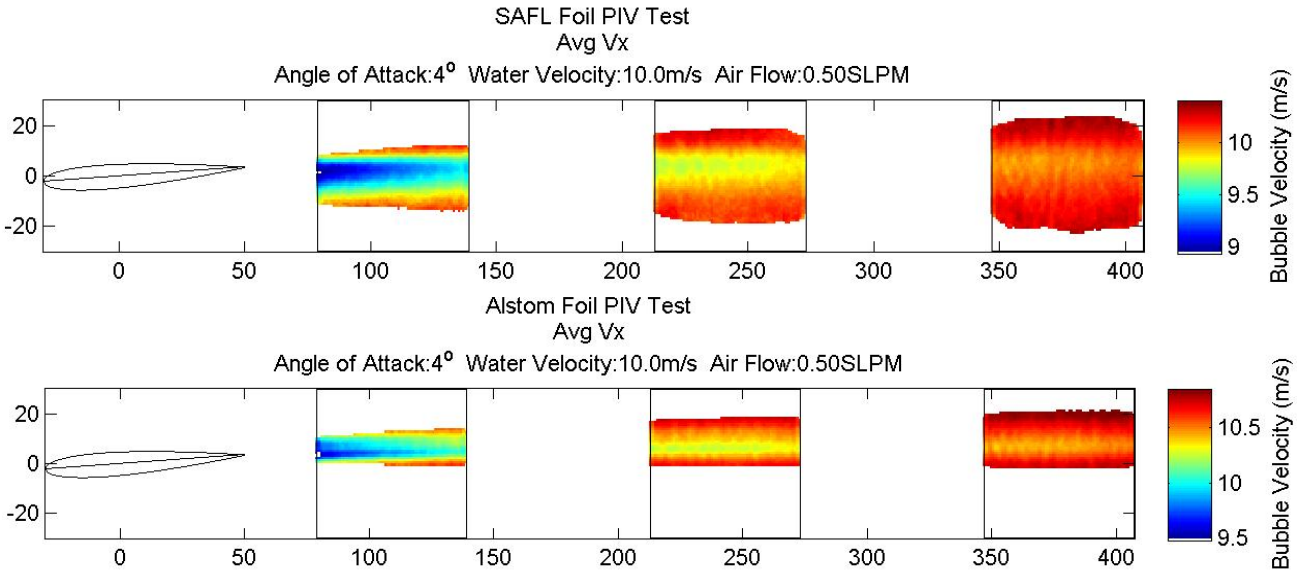

AoA 4° Vel 10.0 m/s Air Flow 1.5SLPM

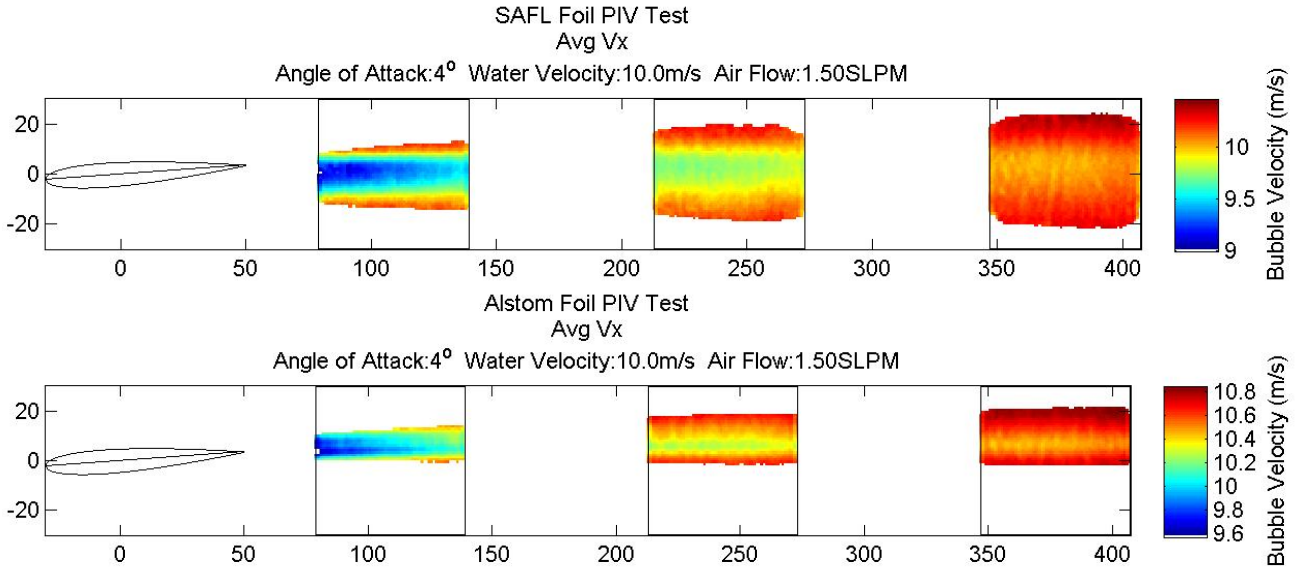

AoA 8° Vel 5.0 m/s Air Flow 0.5SLPM

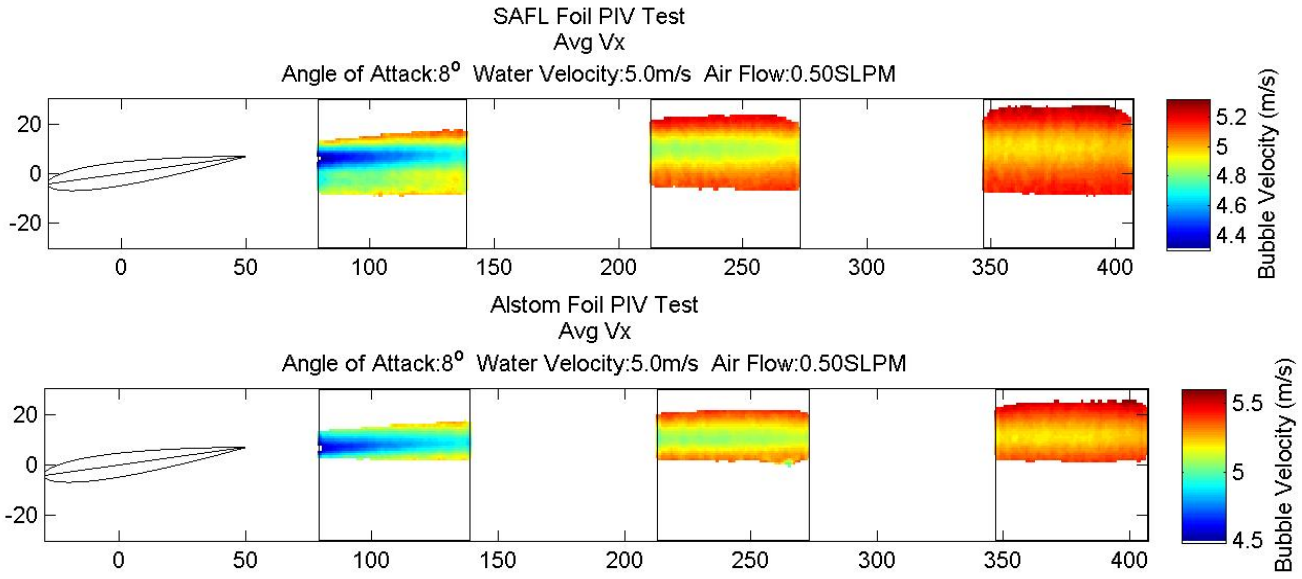

AoA 8° Vel 5.0 m/s Air Flow 1.5SLPM

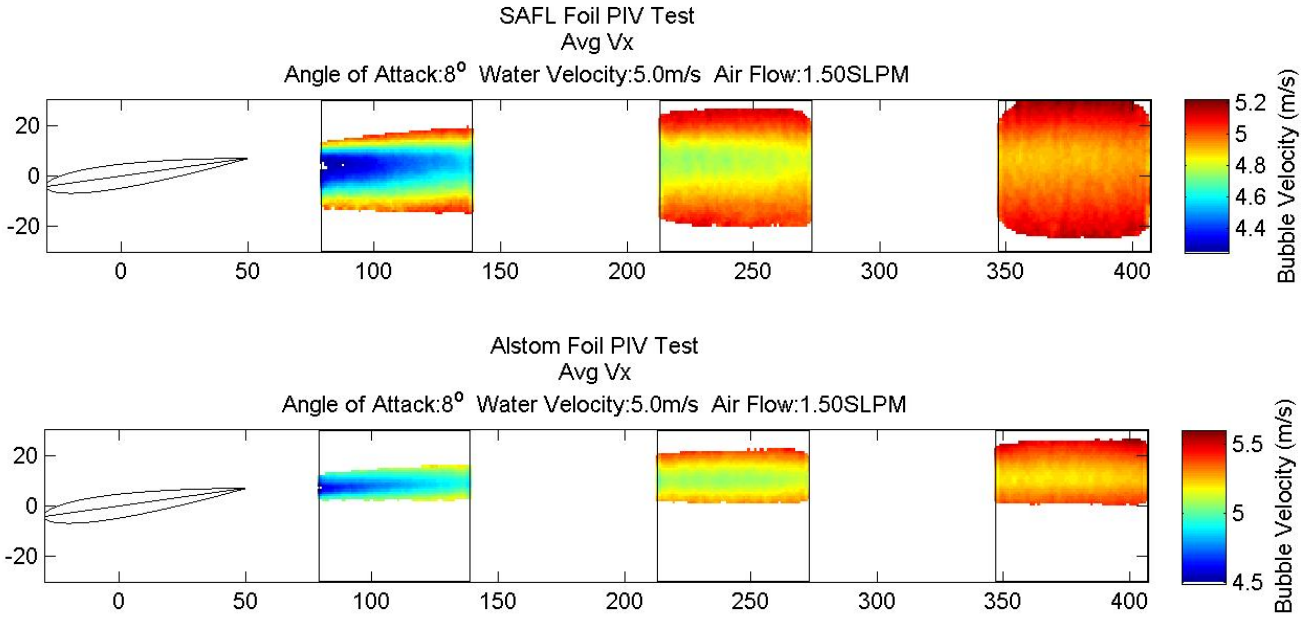

AoA 8° Vel 7.5 m/s Air Flow 1.0SLPM

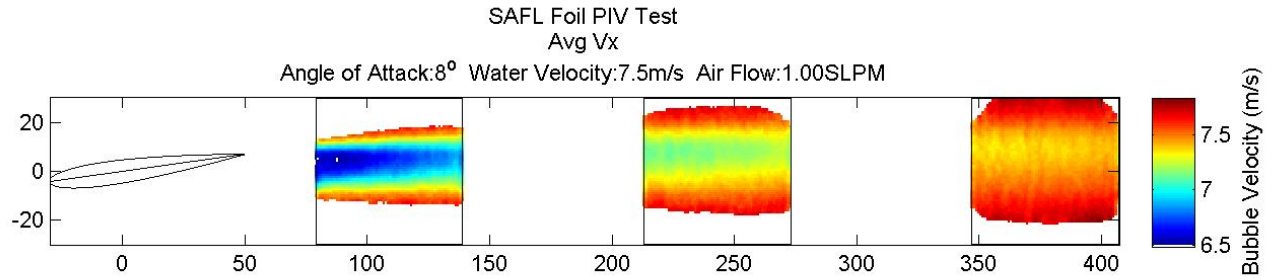

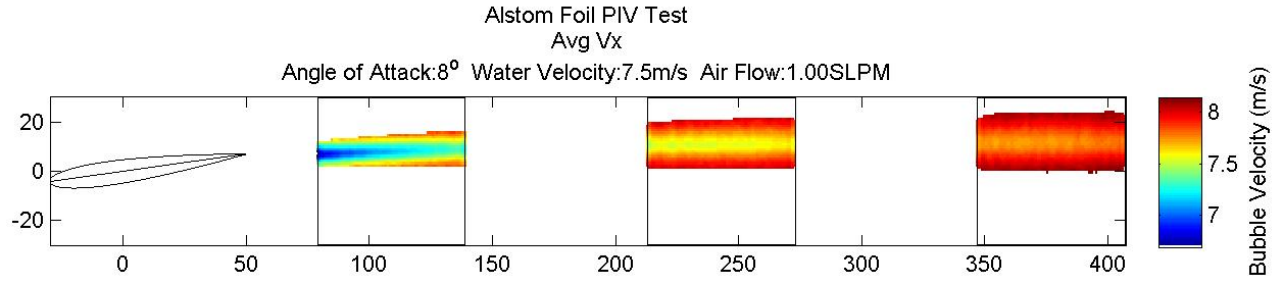

AoA 8º Vel 10.0 m/s Air Flow 0.5SLPM

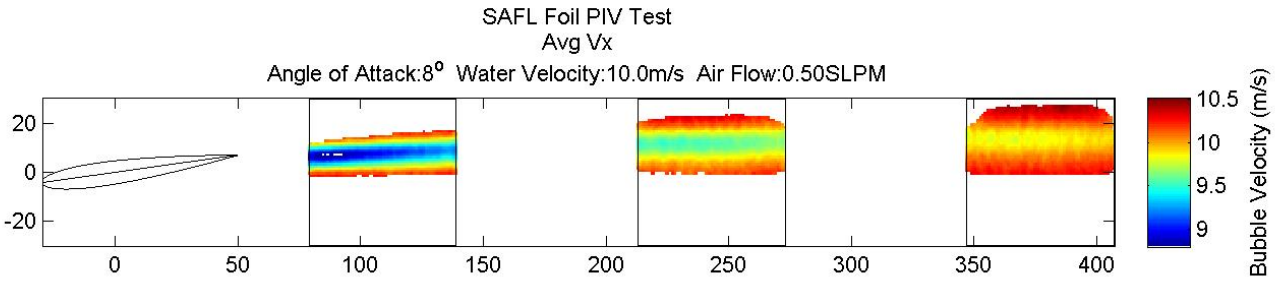

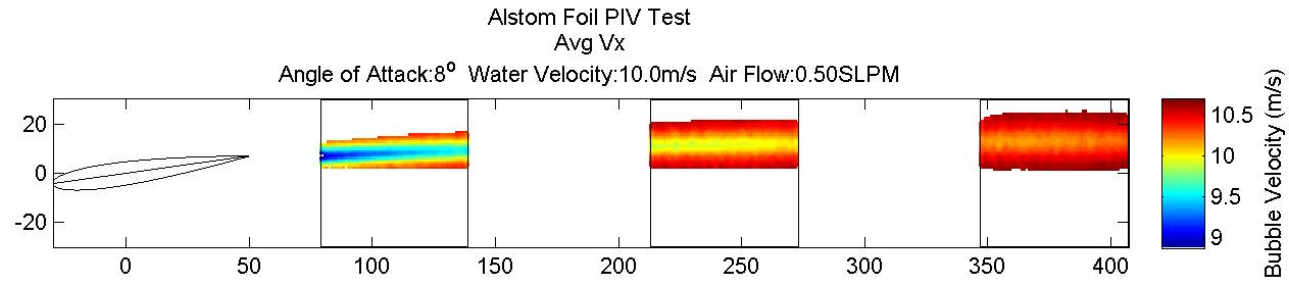

AoA 8º Vel 10.0 m/s Air Flow 1.5SLPM

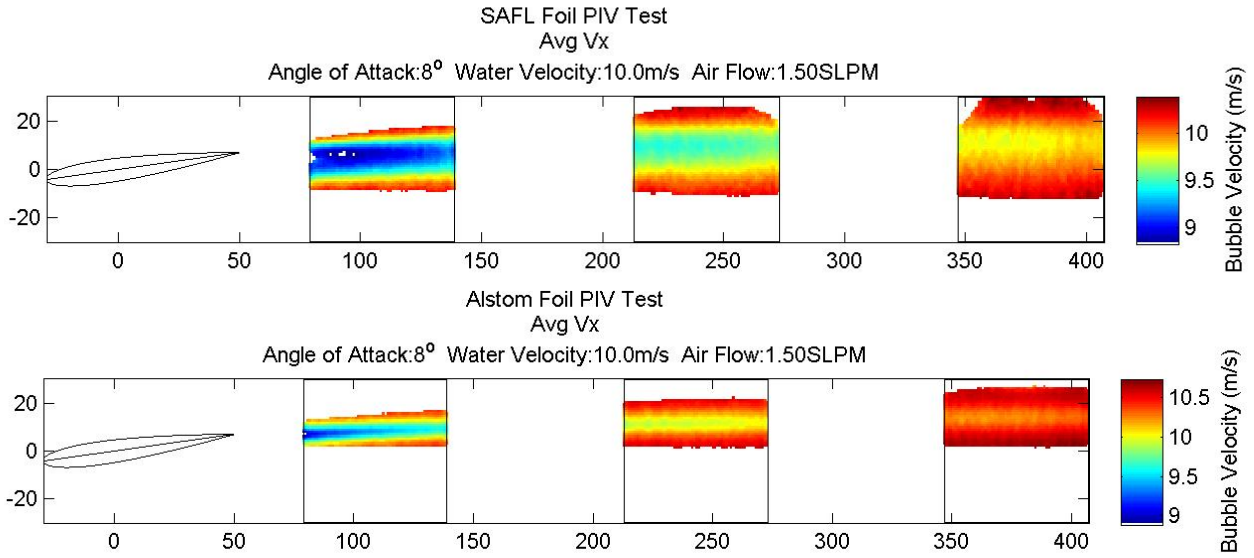
SAFL Foil PIV Test
Avg Vx
Angle of Attack:8° Water Velocity:10.0m/s Air Flow:1.50SLPM
20
0
-20
0
50
100
150
200
250
300
350
400
10
9.5
9
Bubble Velocity (m/s)
Alstom Foil PIV Test
Avg Vx
Angle of Attack:8° Water Velocity:10.0m/s Air Flow:1.50SLPM
20
0
-20
0
50
100
150
200
250
300
350
400
10.5
10
9.5
9
Bubble Velocity (m/s)